2003

On the synthesis of indium-doped tin oxide nanowires

Phó Nguyễn
San Jose State University

ON THE SYNTHESIS OF INDIUM-DOPED TIN OXIDE NANOWIRES

A Thesis

Presented to

The Faculty of the Department of Chemical and Materials Engineering

San José State University

In Partial Fulfillment

of the Requirements for the Degree

Masters of Science

by

Pho Nguyen

August 2003

INFORMATION TO USERS

The quality of this reproduction is dependent upon the quality of the copy submitted. Broken or indistinct print, colored or poor quality illustrations and photographs, print bleed-through, substandard margins, and improper alignment can adversely affect reproduction.

In the unlikely event that the author did not send a complete manuscript and there are missing pages, these will be noted. Also, if unauthorized copyright material had to be removed, a note will indicate the deletion.

ProQuest Information and Learning Company
300 North Zeeb Road
P.O. Box 1346
Ann Arbor, MI 48106-1346

APPROVED FOR THE DEPARTMENT OF CHEMICAL AND MATERIALS ENGINEERING

Dr. Emily Allen

Dr. Melanie McNeil

Dr. Hou T Ng, NASA Ames Research Center

Dr. Meyya Meyyappan, NASA Ames Research Center

APPROVED FOR THE UNIVERSITY

For my parents and brothers,

ABSTRACT

ON THE SYNTHESIS OF INDIUM-DOPED TIN OXIDE NANOWIRES

by Pho Nguyen

Single-crystalline rutile indium-doped tin oxide nanowires, a = 4.685Å and c = 3.200Å, have been synthesized via the vapor-liquid-solid mechanism with carbothermal reduction. SEM, XPS, EDX, and HR-TEM analyses show an average diameter of 94 nanometers, a standard deviation of 19 nanometers, 20:1 tin-to-indium atomic ratio, and heteroepitaxial growth in [100] preferred axis on sapphire substrates. A transistor with the nanowire as the channel shows semiconducting and saturation behaviors.

Thermodynamic analysis suggests a higher concentration of tin-containing species, compared to indium-containing species, generated at the ITO-graphite source, as well as a more favorable reaction mechanism for consumption of tin oxide at the liquid alloy catalytic heads. The analysis underlines the importance of thermodynamics in dictating the final composition of the nanowires.

This breakthrough study introduces a novel method of *in-situ* doping of metal oxide nanowires. Precision doping enables control of the band-gap energy and resistivity. Potential applications of doped nanowires include high-sensitivity bio/chemical sensor applications, solar cells, nano-electronics, and nano-photonics.

Acknowledgements

First and foremost, I sincerely thank Dr. Meyya Meyyappan, Director of the Center for Nanotechnology at NASA Ames Research Center. Dr. Meyyappan provided me the opportunity to work in the emerging and exciting field of nanotechnology. His leadership and support throughout the duration of this project ensure its successful completion.

Secondly, I express my deepest gratitude to Dr. Hou Tee Ng. Dr. Ng taught me how to be an independent researcher; yet, he was always there when I needed him. His vast knowledge and eagerness to teach helped me tremendously; without his supports, an inordinate amount of time would be required to complete this project.

I would like to thank Prof. Melanie McNeil for accepting me as a M.S. student at the Chemical Engineering department and for her thorough support and heartfelt encouragement of my academic plan.

Last but not least, to all of my colleagues at the Ames Research Center – thank you for a very enjoyable experience.

San José, August 2003.

TABLE OF CONTENTS

LIST OF FIGURES

LIST OF TABLES

NOMENCLATURE

VARIABLES

Symbols	Definition	Units
ε	binary bond energy	
ε_o	permittivity of vacuum	
a	lattice parameter	
c	lattice parameter	
CN	coordination number	
Cp	isobaric heat capacity	J/mol K
d	distance between the cations and anions	Å
d*	exponential scaling factor for repulsive term	0.345 Å
e	charge of the electron	1 eV=96480J/mol
E_B	binding energy	kJ/mol
F	Force	N or eV/nm
G	Gibbs free energy	kJ/mol
H	Enthalpy	kJ/mol
K	equilibrium constant	
M	mean or molecular weight	
N	the number of ions in the formula unit	
N_{AV}	Avogadro's number	6.022E+23
P	Pressure	atm
P_i	partial pressure of species "I"	atm
Q	reaction quotient	
R	atomic or ionic radius	
R	gas constant	8.314 J/mol K
Rcryst	Radius of crystalline nanoparticle	
Re	Reynold's number	
S	Entropy	kJ/mol K
s_N	standard deviation	
T	Temperature	Kelvin
U_{POT}	lattice potential energy	kJ/mol
V	volume	m^3
Z	effective nuclear charge or number of bond per atom	
Δ	denote change in a quantity	
ΔH_L	lattice energy	kJ/mol
α	structure-specific Madelung constant	
β	gas compressibility	
γ	surface tension	
λ	constant for the electron cloud repulsive force	

ρ	constant for the electron cloud repulsive force	
ρ	density	kg/m^3

SUBSCRIPTS

Symbols	Definition
-	anion
+	cation
B	boiling
Cr	crystalline
G	Gas
L	liquid
M	melting
Min	value at minimum
Mix	value as a result of mixing
RXN	reaction quantity
S	solid

SUPERSCRIPTS

Symbols	Definition
o	denote standard state
f	denote formation value
A	denote activation state

ABBREVIATIONS

Abbreviation	Definition
AFM	atomic force microscopy
CMOS	complementary-metal-oxide-silicon
CNT	carbon nanotube
CPU	central processing unit
DRAM	dynamic random access memory
EDX	energy-dispersive X-ray spectroscopy
FE-SEM	field-emission scanning electron microscope
HR-TEM	high-resolution transmission electron microscope
IC	integrated circuits
IN	Inch
ITO	indium tin oxide (90 wt% indium oxide and 10 wt% tin oxide)
MFC	mass flow controller
nm	nanometer (10^{-9} meter)
NW	nanowire
OAM	oxide-assisted mechanism
SAED	selected area electron diffraction
SCCM	standard cubic centimeter per minute
TCO	transparent conducting oxide
VLS	vapor-liquid-solid
VS	vapor-solid
XPS	X-ray photoemission spectroscopy
XRD	X-ray diffraction

CHAPTER ONE - INTRODUCTION

NANOTECH - THE LEAP-FROG TECHNOLOGY

1.1 Overview and Definition of Nanotechnology

1.1.1 Overview

Nanotechnology. The whole notion of nanotechnology is exotically vague and evasively alien to a vast number of people. When one thinks of nanotechnology, one envisions the world of K. E. Drexler [1], where mankind achieves omnipotence. In this fantasy world, nanocomputers provide recipes to nanomachines, which manufacture virtually anything from cheap raw materials and solar energy by atomic-level manipulation. Human life expectancy reaches unprecedented longevity due to the miniaturized machines, which roam human arteries and veins to repair damaged biomolecules, tissues and organs, and enhances the immune system of the host.

Realistically, Drexler's vision may never materialize but nanotechnology is not simply a trendy and novel technology that will evaporate as rapidly as cold fusion and ceramic superconductivity; applications based on nanotechnology are gradually permeating themselves into mainstream products, inconspicuously. To clarify certain confusion, the definition of nanotechnology will be stated, along with some current applications. Subsequently, the focus will be shifted onto metal oxide nanowires (NW), their novel properties, and growth methods.

1.1.2 Definition and Some Technological Developments

Nanotechnology is the design and synthesis of novel and functional structures having dimensions that measure 100 nanometers or less.

In his famous talk delivered on December 29th, 1959 at the annual meeting of the American Physical Society at the California Institute of Technology, Richard Feynman gave birth to nanotechnology in "There's Plenty of Room at the Bottom" [2]. During that talk, Feynman presented his vision and established the Feynman prize to encourage researchers to achieve that vision. Since then, numerous technological and scientific advancements have enabled researchers to synthesize, characterize, and utilize sub-micron structures.

The discovery of carbon nanotubes by S. Iijima [3] in 1991 rapidly gravitated scientific interest toward nanostructures, i.e. structures measure 100 nm or less in a dimension, due to their remarkable mechanical and electrical properties [4, 5]. Subsequently, nanostructures of a vast range of compositions have been discovered to possess novel electrical, optical, and mechanical properties due to the quantum confinement effects and the crystallinity of these structures. Nanostructures encompass multiple subsets such as biomolecules, nanoparticles, nanotubes, nanobelts, and nanowires.

In 2000, researchers at International Business Machine Corporation (IBM) announced successful fabrication of transistors having carbon nanotubes (CNT) as the conducting channels [4], which outperform leading contemporary silicon counterparts. In 2003, IBM successfully created an electrically pumped infrared light emitter based on the single-

walled CNT field effect transistor (FET) having emission wavelength of 1.5 micrometers [4], the world's smallest solid-state light emitter, as shown in Figure 1.1. And currently, IBM is working on integration of the CNT-based transistors into ultra-dense circuits [4]. Hewlett-Packard (HP) success in fabrication of a molecular grid facilitates its design as a communication network between electronic devices, such as the transistors and resistor, or utilization as a foundation for future molecular microprocessor development [6]. Cetek Technology Inc., recently, acquired the technology from Motorola to produce and manufacture CNT triodes for flat panel display screens [6]. The technology will allow production of 60-in screens as easily as 2.5-in screens, with lifetime in excess of 10,000 hours [6]. Compared to current active-matrix liquid crystal display (LCD) technology, CNT flat screens offer enhanced resolution and one-tenth the power consumption, at only one-third of the manufacturing costs [6]. Other applications of CNT such as automotive painting technology from General Motors for better adhesion and CNT tips for atomic force microscopy for better resolution and durability have already entered the commercialization phase.

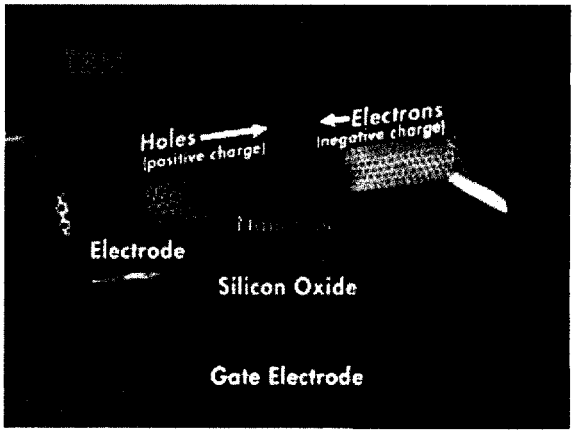

Figure 1.1. Electronically-pumped carbon nanotube FET light emitter [4].

Some developments in the area of biotechnology include a programmable two-state, two symbol finite automation DNA computer [7], a holographic optical data storage system based on a retinal protein molecule found in the micro-organism *halobacterium salinarium* called bacteriorhodopsin [8], biosensors for improved sensitivity [8], and catalysts for enhanced selectivity and reaction rate [8].

In terms of electronics and photonics based on inorganic one-dimensional (1D) nanostructures, much progress has been achieved. In optoelectronics, ZnO nanowires [9] have been found to exhibit photoluminescence behaviors with emission wavelength of approximately 380 nm at room temperature, as shown in Figure 1.2. Luminescent effects are briefly explained in Appendix D. Intensive researches are being conducted to create an electronically pumped laser, similar to the CNT laser. Some other photoluminescent nanowires are GaAs and silicon. A mass-produced, high-efficiency, room-temperature, tunable, miniature, ultraviolet laser source will have many commercial applications, such as optical data storage, videogames, laser printer, scanners, full-color electroluminescent displays, toxic monitor devices, water purification, decontamination of bacteria, and military covert communication [10]. An example of an electronically pumped p-n diode junction comprised of two crossing indium phosphite nanowires is demonstrated in Figure 1.3. Intensive research is in progress to integrate these laboratory devices into commercializable functional devices.

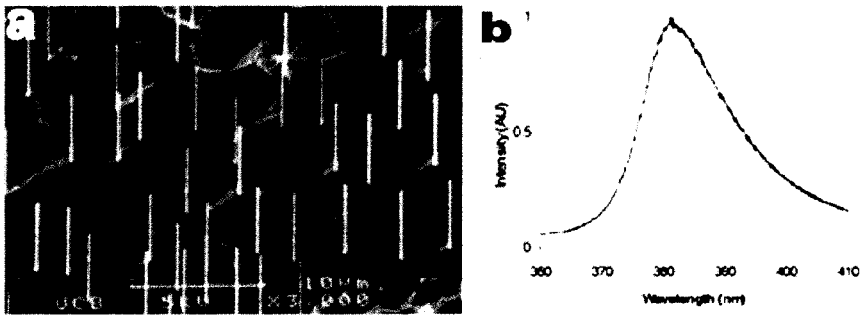

Figure 1.2. Optically-pumped ZnO cavity laser [9]. (a) SEM image of vertical zinc oxide nanowires and (b) photoluminescence spectrum of the laser showing peak emission in the ultraviolet range.

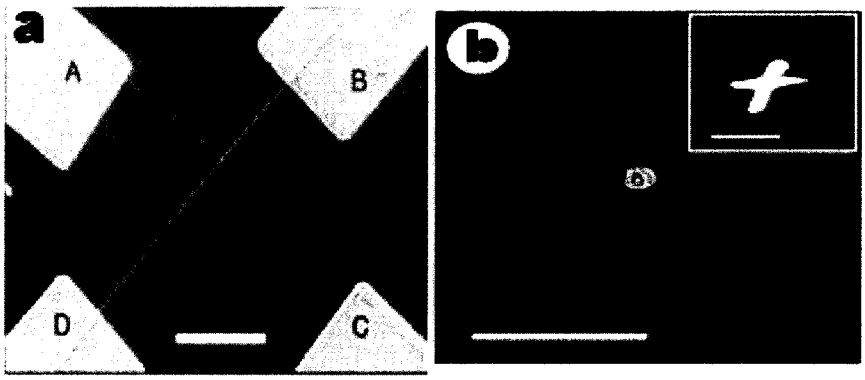

Figure 1.3. Indium Phosphite NW p-n diode junction [11]. (a) SEM image of the junction and (b) luminescence at 780 – 830 nm. Scale bars are 1 μm.

Various nanoelectronics achievements include gallium nitride nanowire FET [12], silicon nanowire inverter and bipolar transistor [13], as shown on Figure 1.4. Presently, nanoscale integrated circuitries (IC), comprised of logic gates with such nanowires as the channels, are being developed. The commercial potentials of these devices are enormous, as well.

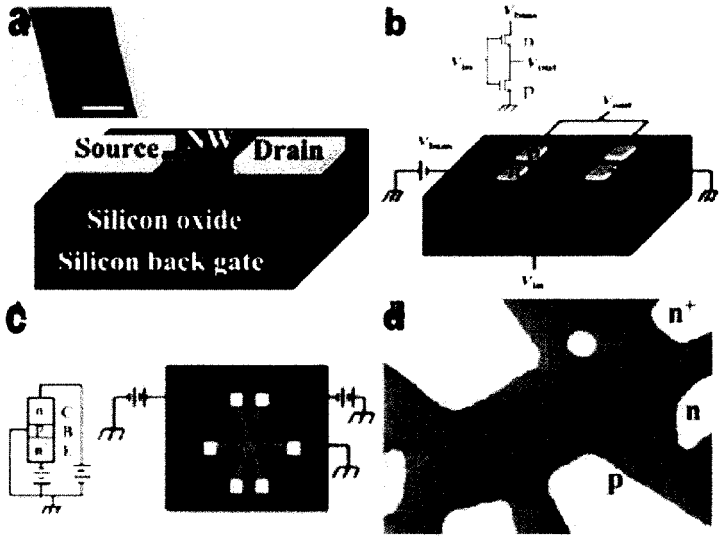

Figure 1.4. Illustrative nanoelectronics devices. (a) Gallium Nitride NW field-effect transistor [12], (b) Silicon NW inverter, and (c)-(d) Si NW bipolar transistor, [13].

For the semiconductor industry, existing "nanotechnology" enables manufacturers to produce smaller, faster, higher energy-efficiency and economical IC chips, such as the central processor units (CPU) and the random-access-memory (RAM) modules. Currently, Intel Corp. is working on a depleted-substrate complementary-metal-oxide-silicon (CMOS) transistor with the transistor gate length of 50 nanometers [14]. However, recently, many limitations of current semiconductor technology, such as the quantum behavior of electrons as the gate thickness shrinks to oblivion, heat dissipation, lithography, and the economy of production, began to surface. It has been predicted by numerous leading researchers, investors, and policy-makers that the "leap-frog" nanotechnology will revolutionize the world and supplant the current semiconductor "nano"-technology. Figure 1.5 illustrates a representative technology progress timeline where nanotechnology and molecular computing become the replacement technologies.

Figure 1.6 demonstrates the personal forecast of the author of this study. As shown in Figure 1.6, despite ingenious technological advancement, the silicon-based semiconductor will encounter its absolute limit beyond which further advancements will be infeasible due to discussed limitations. Nanotechnology, along with molecular electronics and quantum computing, will continue to fulfill Moore's law for the performance-per-IC-area index; however, it will also plateau as it reaches the absolute limit of physics, beyond which improvement of performance will be unattainable. It appears an inevitability that nanotechnology and molecular technology will fuel the engine of economy growth and technological progress in the next era.

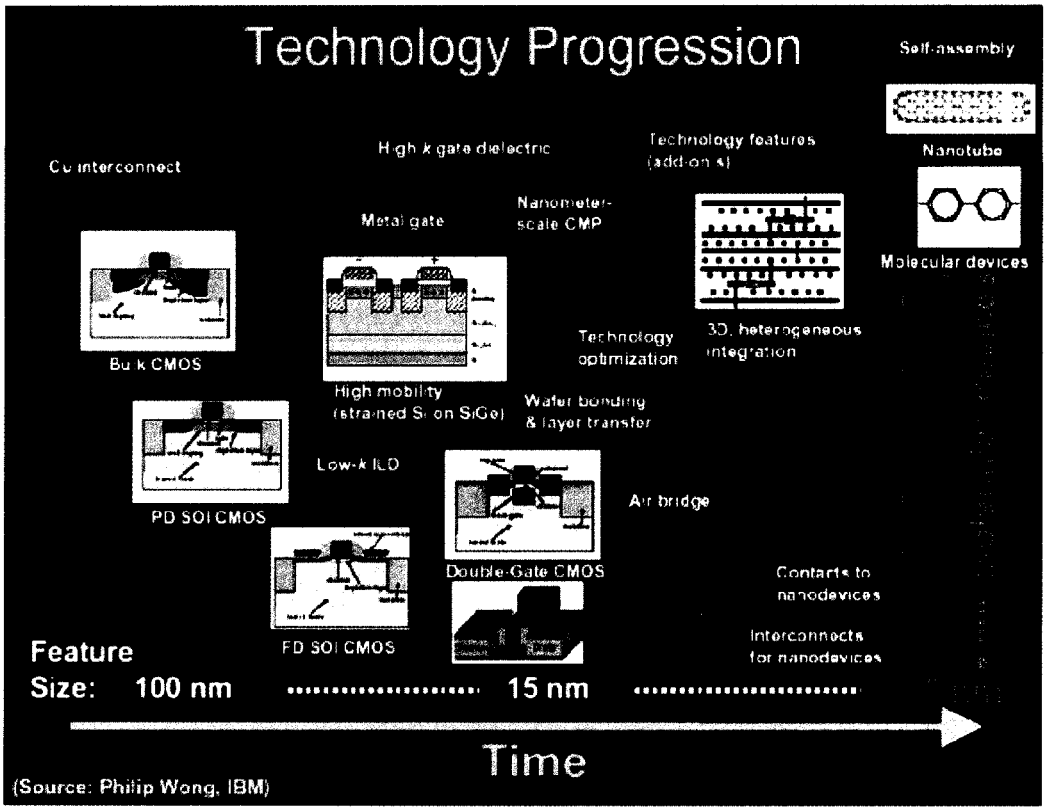

Figure 1.5. Technology Progression Timeline [4].

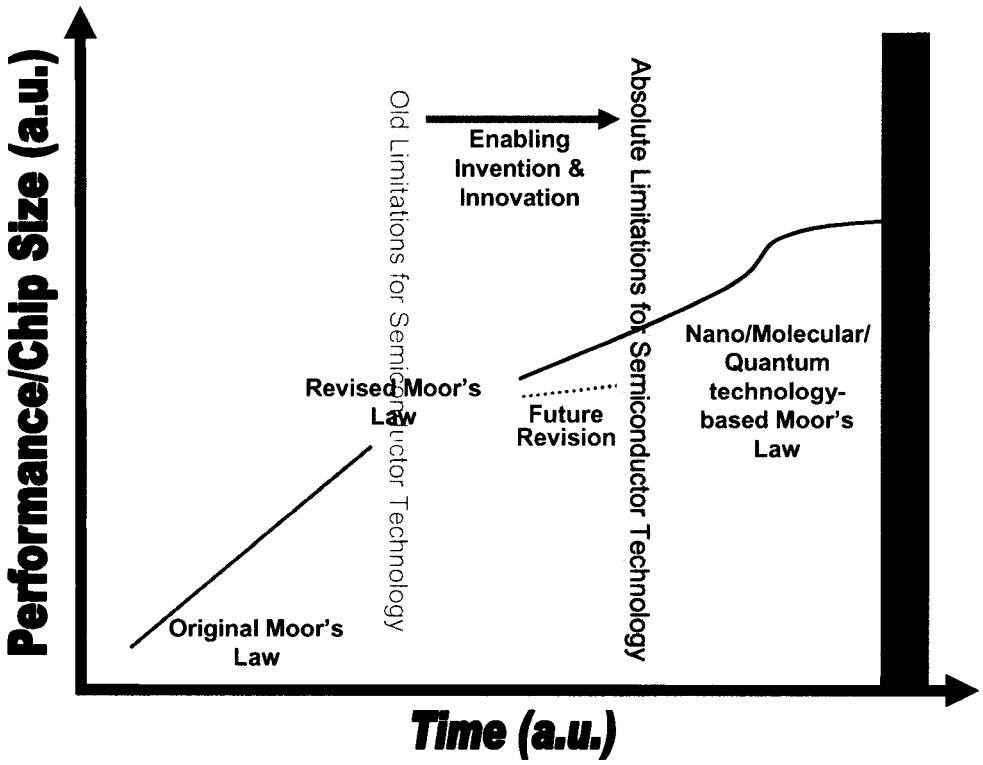

Figure 1.6. Progress of Technology as viewed by the author.

Given the enormous potentials of nanostructures, it comes as no surprise that nanostructures have captured the attention of the scientific community and many advances have been achieved within the last decade. Thus, government-sponsored, as well as corporate-sponsored, research has received billions of dollars around the world. Figure 1.7 demonstrates the lofty vision that many people entrusted in nanotechnology.

Successful growth of nanostructures is the fundamental step, as it allows characterization of the optoelectronic properties of the structures. Financial realization will be a consequence of feasible integration into functional devices and economical mass manufacturing. Presently, nanotechnology is still in its infancy and there are only a few

products entering the commercialization phase, such as light bulbs, flat panel displays, atomic force microscopy (AFM) tips, and automotive paint adhesion factors. Worldwide intensive researches persist on synthesis of nanostructures of new materials and fabrication of functional devices based on such nanostructures. Envisioned high-tech and novel applications are being developed and, expectedly, much of the visions may turn out to be pure hype. But the risk is too high not to invest in it as everyone is rushing into the new frontier and hoping to strike gold.

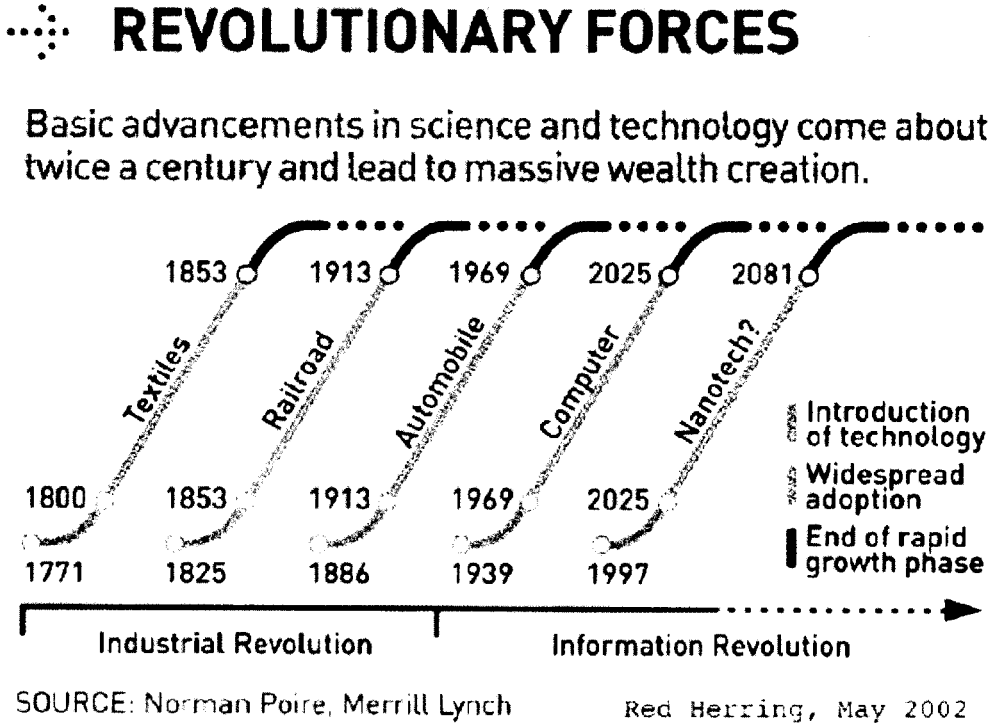

Figure 1.7. Nanotechnology-The Next Revolution

1.2 Tin-Doped Indium Oxide

For inorganic one-dimensional structures, much focus has been on traditional semiconductor materials, such as germanium [15, 16], silicon [17], GeO_2 [18], and GaN [19, 20]. Recently, nanostructures of various wide-band-gap transparent conducting oxide (TCO), such as ZnO [9, 10], In_2O_3 [21], CdO [22], and SnO_2 [23], have been synthesized. Nonetheless, no report on the synthesis of doped wide-band-gap TCO materials has been located in the literature.

Potential commercial opportunities of wide-band-gap TCO nanowires include molecular electronic devices due to the ease of functionalizing a nanowire with biological and chemical molecules, miniaturized ultraviolet laser sources due to the large band gap energy and quantum confinement effects, solar cells due to its optical transparency and electrical conductivity, toxic gas monitor devices due to the high surface-area-to-volume ratio and enhanced electrical sensitivity to various gases facilitated by the electron transfer between the gaseous molecules and the nanowire surface, and nano-optoelectronics due to their optical transparency and semiconducting properties. Doping allows precise control of the band gap energy and the resistivity of the wires.

In thin-film form, tin-doped indium oxide (ITO) is the preferred transparent conducting oxide (TCO) material of choice for optoelectronic device applications among the wide-band gap TCO class, which includes ZnO, In_2O_3, SnO_2, CuCl, BeTe, $CuAlS_2$ and GdInOx in optoelectronic device applications, due to its superior optoelectronic properties. Bulk ITO possesses optical transmittance as high as 95%, electrical resistivity as low as $2\text{-}4x10^{-4}$ Ω cm, and band gap energy between 3.3 eV to 4.3 eV, depending on

the growth conditions [24]. Although no data on its exciton binding energy are reported, it is postulated to be approximately 40 meV, as the value of zinc oxide is 60 meV [9]. Generally, an exciton binding energy greater than 20-25 meV is recommended for potential lasing applications to ensure stability at room temperature [10]. Deductively, ITO nanowires have promising potential of being a tunable room-temperature laser, whereas ZnO [9] has a peak wavelength of 380 nm. It is expected that crystalline ITO nanowires will have improved optical transparency; accordingly, highly doped crystalline ITO nanowires may find applications in optical waveguides, optical switches, and interconnects. On sensing applications, tunable bandgap energy may yield nanowires with selective sensitivity for different gases. The maximum carrier concentration is calculated to be approximately 2.3×10^{19} cm^{-3} in ITO thin film [18]. Accordingly, the feasibility of synthesis of tin-doped indium oxide nanowires is being investigated in this study.

CHAPTER TWO - BACKGROUND

NANOWIRES: PROPERTIES AND SYNTHESIS METHODS

2.1 General Behaviors of Nanostructures

2.1.1 General Quantum Confinement Effects

By definition, nanostructures have dimensions of 100 nanometers or less. At such diminutive length scale, the structures exhibit quantum confinement effects not observed of bulk materials. The electronic quantum confinement effects are governed by Schroedinger's equation, whose solution is a function of the principal quantum number, the orbital quantum number, and the magnetic quantum number. For one-dimensional structure, the solution is given in Equation 1; evidently, the energy of an electron confined in a one-dimensional structure is a function of the physical size of that structure. As predicted by Equation 2, wide-band-gap and semiconducting nanostructures exhibit observable luminescence that is shifted to higher energies due to the inverse relationship between the size of the nanostructures and band gap between the minimum of the conduction band and the maximum of the valence band, as shown in Figure 2.2.a.

$$\frac{-\hbar^2}{2\ m}\nabla^2\Psi - U(x,y,z)\ \Psi(x,y,z) = E\ \Psi(x,y,z)$$

$$\Psi(r,\theta,\phi) = R(r)\ P(\theta)\ F(\phi)$$

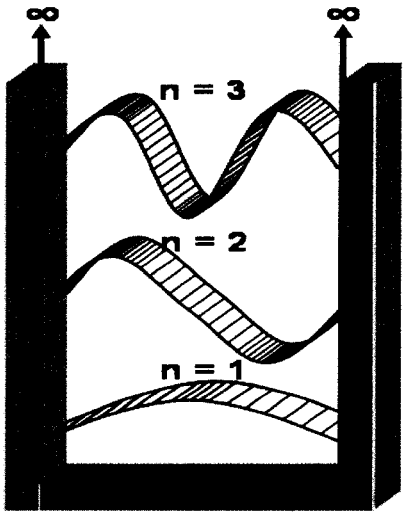

Figure 2.1. 1-D quantum well.

$$E = \frac{(n_1^2 + n_2^2 + n_3^2)\ h^2}{8\ m\ L^2} \qquad \text{Equation 1}$$

$$E_{g,\ nanocrystal} = E_{g,\ bulk} + \Delta E_g = E_{g,\ bulk} + \frac{\hbar^2 \pi^2}{2\ M\ R^2_{nanocrystal}} \qquad \text{Equation 2}$$

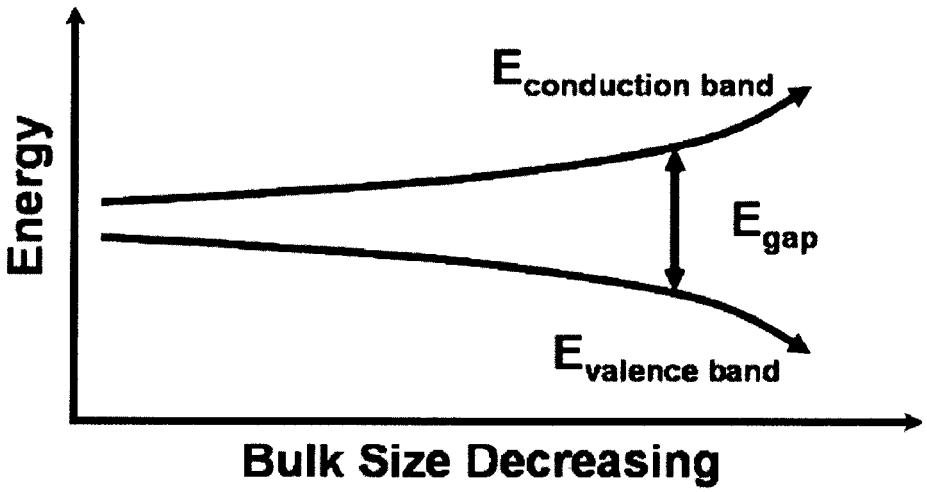

Figure 2.2.a. Dependence of band gap on size of semiconducting structure [28].

As the physical dimensions diminish, the band gap enlarges, resulting in a higher excitation energy required to promote an electron from the valence band to the conduction band and a larger energy released upon recombination of the electron-hole pair. Figure 2.2.b depicts the "blue shift" of the optical absorption edge and the photoluminescence spectrum as the physical size of the structure decreases. As the physical size of the nanostructures vanishes, the probability of luminescence from recombination of the electron-hole pairs also increases due to the confinement effects.

The quantum confinement effects have been observed experimentally for numerous materials and tabularized in Figures 2.3.a-c. Figure 2.3.a demonstrates accord between theoretical prediction and experimental validation of the bandgap energy of zinc oxide quantum wells having dimension less than 100 nm [29]. The dependence of bandgap energy on size of silicon powder is plotted on Figure 2.3.b – the optical absorption edge and photoluminescence shift toward shorter wavelength regime as the physical size decreases [30]. Li *e. al.* [31] reports that the thermal conductivity of silicon nanoparticles decreases with of size, as shown in Figure 2.3.c, as well.

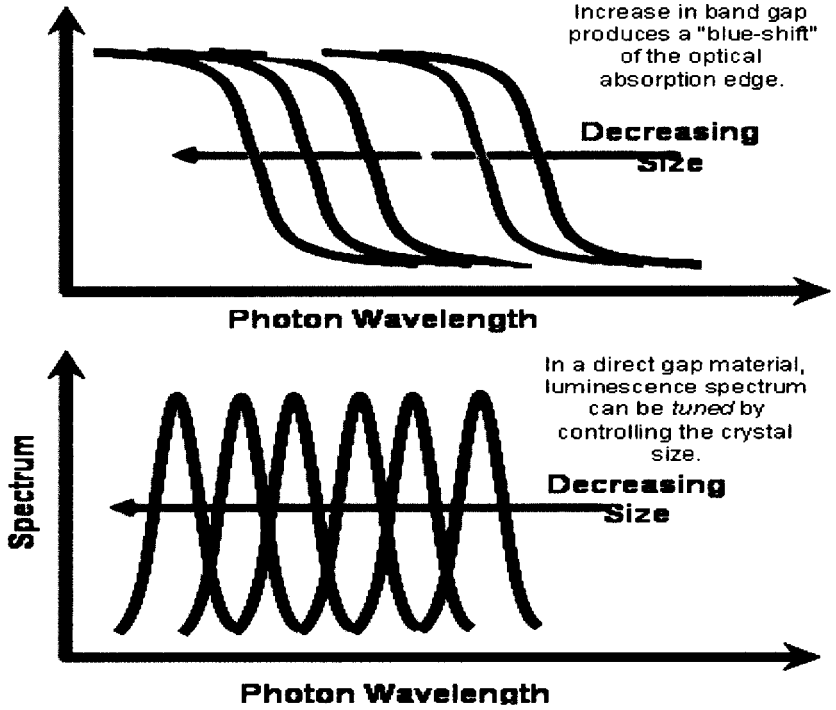

Figure 2.2.b. Optical absorption and emission as function of physical size [28].

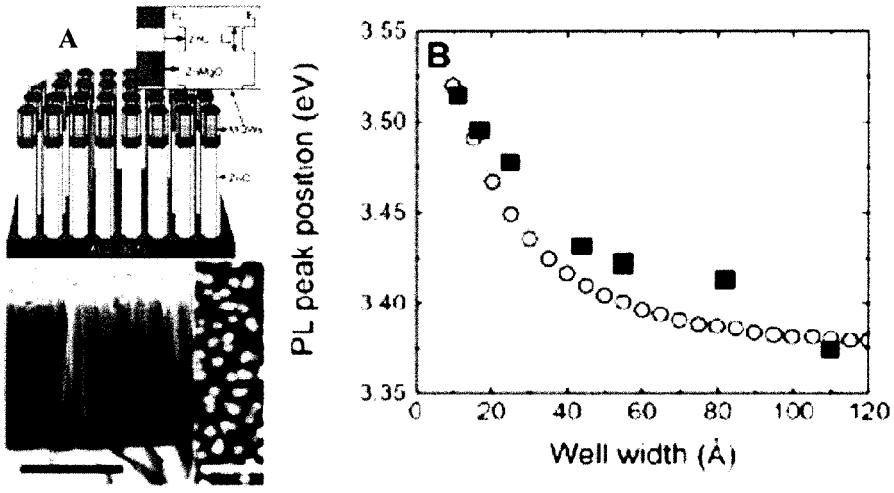

Figure 2.3.a. Quantum confinement effect of ZnO nanostructure [29].
(a) ZnO quantum well bounded by ZnMgO, as grown by metal oxide CVD.
(b) Photoluminescence effect showing good agreement with theoretical prediction.

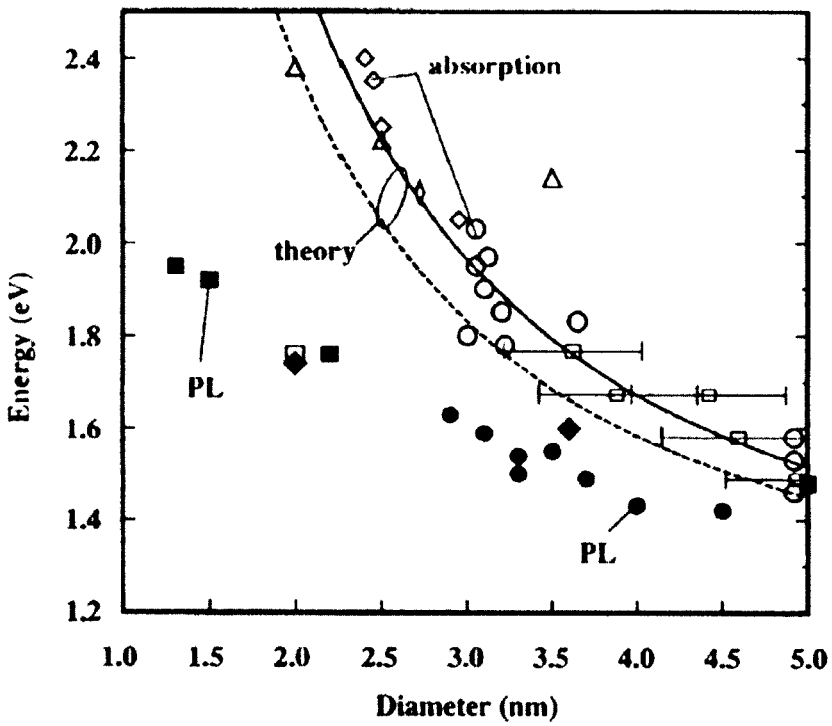

Figure 2.3.b. Increase of bandgap energy of silicon as a function of size [30].

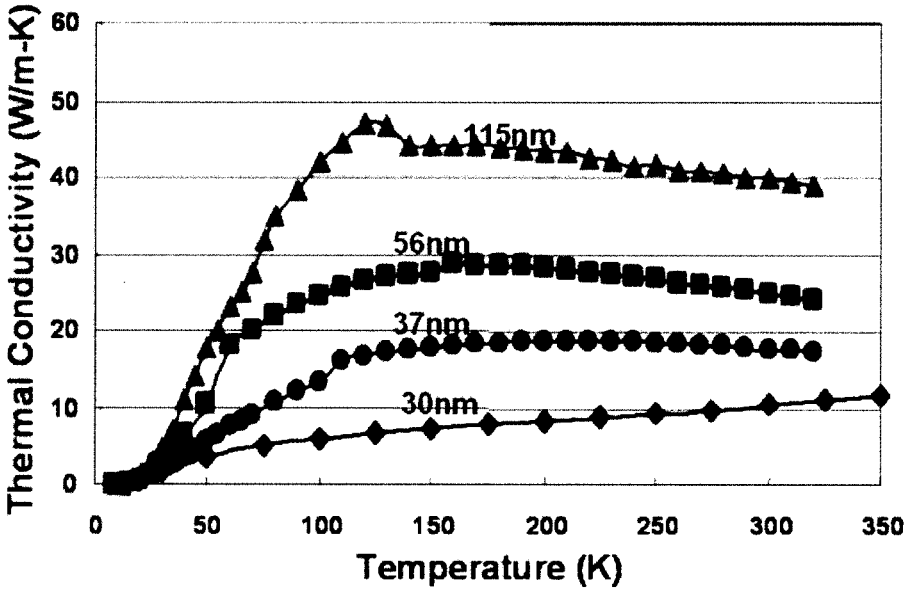

Figure 2.3.c. Si thermal conductivity dependence on physical dimensions [31].

2.1.2 Moss-Burstein Effect

The bandgap width of wide-bandgap semiconductors exhibits dependency on the concentration of the charge carrier, due to the Moss-Burstein shift. This phenomenon is observed when a semiconductor is heavily doped. For the case of *n*-type doping, the tips of the valence band and the bottom of the conduction band swell slightly due to the excessive concentration of elections at those locations. All of the low-energy states in the conduction band and the high-energy states in the valence band are occupied due to excessive doping.

Thus, the electrons at the top of the valence band cannot transition into the low-energy states in the conduction band upon excitation. Correspondingly, the effective photon energies for optical absorption will be approximately increased by the Fermi energy amount to promote the electron from the top of the valence band to the top of the conduction band. Consequently, the fundamental absorption edge will shift toward the shorter wavelength region of the electromagnetic spectrum with increasing carrier concentration. And a higher amount of energy will be released in form of an energetic photon or a phonon as the electron transitions from the bottom of the conduction band to the bottom of the valence band. This behavior is displayed in Figure 2.4. Here, the band structure is assumed to be parabolic as shown below.

Report of the Moss-Burstein effect in 2-D, 1-D, and 0-D nanostructures has not been located in the literature. Successful synthesis of ITO nanowires will provide a template for development of a controlled doping process, which will enable the study of the

electronic properties of highly doped nanostructures. Future design of optoelectronic devices, which capitalize on this effect, logically ensues.

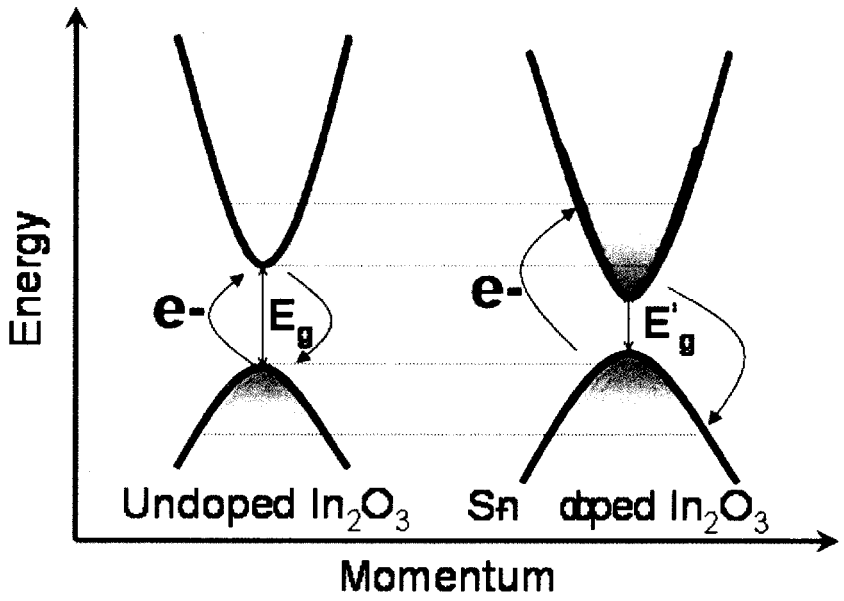

Figure 2.4: Reduction in apparent bandgap due to *n*-type doping [28]. The curved arrows denote the electron transition path.

2.2 Synthesis Methods

For nanowire synthesis, successful synthesis methodology enables precise control of the optoelectronic properties of a nanowire, its morphology and crystallinity, its exact location and the distribution density, and accommodates successive processing steps for device integration. The optoelectronic properties and morphology of a nanowire are functions of its crystallinity, such as crystal structure, crystal defects and the growth orientation, the dopant or impurity concentration, its diameter, its length, the capping at both ends, and the outer sheath. Quantum-confinement calculations explain why and

how the optoelectronic properties of a nanostructure depend greatly on its physical dimensions. The need for ease of device integration is apparent. Here, device integration encompasses both academic and commercial purposes.

Currently here are three predominant methods for nanowire growth: Laser Ablation [32 -35], Chemical Vapor Deposition [10, 11, 15-17], and Physical Vapor Deposition [18, 36]. Other methods include ion-beam synthesis [37], supercritical fluid solution-phase synthesis [38], or electrochemical deposition. Chemical compositions of these nanowires include germanium [15-16], ZnO [9], Si [17], GaN [19-20], SiOx [39], GaAs [29, 40], $ErSi_2$ [41 - 42], and $YBBCu_3O_7$ [35], CdO, and In_2O_3 [21], among others. Table 2.1 tabulates the various synthesis methods, along with their respective advantages and disadvantages.

As summarized in Table 2.1, the catalyst-assisted chemical vapor transport process is the preferred synthesis method due to its simplicity and ease of control. Unfortunately, for a given set of growth conditions, various growth phenomena may compete and nanowires of inconsistent morphology and characteristics may result. Thus, it is imperative to understand the various potential mechanisms to elucidate what is happening as the data are analyzed. Generally, the catalyst-assisted growth process follows the Vapor-Liquid-Solid (VLS) model. However, if an oxide is present in the nanowire growth material or if the growth material is an oxide itself, some nanowire growth may proceed under the Oxide-Assisted model (OAM). Compared to the VLS model, the OAM results in nanowires with higher defect density and it offers inferior control over localization and growth orientation of the nanowires. Evidently, process parameters

under which the oxide-assisted growth prospers should be avoided. In addition, under some growth conditions, the physical vapor deposition (PVD) process may compete with the catalyst-assisted chemical vapor deposition process. Although both methods potentially produce crystalline structures, VLS growth allows superior wire localization and diameter control. Consequently, when growth by the VLS mechanism is preferred, conditions under which physical vapor deposition thrives should be avoided. A more detailed discussion of the OAM and PVD is presented in Appendix A.

The three mechanisms are tabulated in Table 2.2 for comparison since their coexistence within a reactor set-up is plausible. There are other vapor-deposition models, such as the Charged-Cluster Model, but they are irrelevant under conditions where catalyst-assisted CVD growth is attempted. The processing conundrum is to determine a feasible processing window which is facultative to VLS growth mode and inhibitive to the other two growth modes. Thus, thorough understanding of all growth mechanisms will provide valuable insights to development of a judicious growth strategy and analysis of the data.

Based on the available information, synthesis by the catalyst-assisted vapor transport method using the chemical vapor deposition scheme is the better choice for exploratory nanowire synthesis of high melting temperature metal oxide compositions. Accordingly, the following sub-sections discuss various sequences of this method, namely, carbothermal reduction to generate the vapor source, VLS growth, and heteroepitaxy which determines the growth orientation. Chapter Three discusses in details the critical processing parameters for VLS growth.

Table 2.1. Comparison of various nanowire synthesis methods

Methods	General Description	Advantages	Disadvantages
Laser Ablation	Vapor source, generated by high-power laser ablation of solid target, is transported by an inert carrier gas to a lower temperature deposition zone where growth proceeds by VLS mechanism, [33-35].	High crystallinity, Good diameter control, Easy control of localization, size distribution, and growth orientation, and *In-situ* doping and layered 1-D structures of various compositions possible.	Intensive tool requirement, Prohibitive cost of a high-powered laser, And voracious demand of energy.
Chemical Vapor Deposition (CVD)	Transport of vapor source, generated either by evaporation or carbothermal reduction of liquid or solid source, to a catalyst-coated substrate precedes 1-D growth by VLS mechanism [10, 11, 15-17].	High crystallinity, Good diameter control, Easy control of localization, size distribution, and growth orientation is simple, and Inexpensive toolsets.	Materials with low volatility and reactivity toward the carbothermal reduction may be excluded, and Simultaneous deposition of multiple materials may be difficult.
Physical Vapor Deposition (PVD)	Evaporation of source and condensation onto the surface of the substrate [18, 36].	Least complex toolset requirement.	Same disadvantages as CVD, and Minimum control over localization and diameter distribution.
Ion-Beam Synthesis	Photolithography, anisotropic etching with KOH, and subsequent thermal oxidation are performed on (001) silicon wafer to form the V-grooves of SiO_2. The groove is implanted with germanium ions & annealed nitrogen ambient, [37].	High-quality Ge NW, and Small diameter range of 5-10 nm.	Extremely low yield, Multitude of processing tools (lithography, etching, thermal oxidation, and ion beam implantation), and Difficulty in harvesting or integration into complex optoelectronic devices.

Table 2.2. Comparison of various vapor-transport synthesis mechanisms

Mechanisms	General Description of Mechanism	Advantages	Disadvantages
Vapor-Solid (VS)	Evaporation of the source and condensation of the vapor-phase source material at energetically favorable sites on the surface of a substrate. VS can happen when VLS is planned [18].	No metal alloy nano-tips.	Minimum control over crystallinity, localization, and diameter distribution.
Oxide-Assisted (OA)	OA happens when VS or VLS is planned if oxide is present in the source. Observed for Si [42 - 46], Ge [19], GaAs [47], and GaN [48] systems. Mechanism for Si system, $Si_xO \rightarrow Si_{x-1} + SiO \quad (x > 1)$ $2SiO \rightarrow Si + SiO_2$. The Si_xO shell on the NW tip acts as a catalyst. During growth, the SiO_2 shell retards the lateral growth and structural defects, such as stacking faults and micro-twins, enhance elongation of the wire [43-46].	No metal alloy nano-tips.	High defect density stacking faults, micro-twins, silicon oxide nanoclusters inside the nanowires, Irregular directionality, and An amorphous silicon oxide outer layer.
Vapor-Liquid-Solid (VLS)	Three distinct stages: *metal alloying, nucleation,* and *axial elongation.* Discussed in details in Section 2.2.3 and Chapter 3.	Same as CVD in Table 2.1.	Same as CVD in Table 2.1. Presence of metal alloy tips, whose removal may be difficult when not desired, and Metal contamination possible for device integration.

2.2.1 Carbothermal Reduction

Synthesis of nanowires, of materials having high-melting temperature, via the catalyst-assisted vapor transport process is difficult to achieve if thermal evaporation is the only means of source generation. Therefore, carbothermal reduction provides an alternative to generate vapor source at moderate temperature. Carbon reduction of metal oxides, such as CuO, CuO_2, SnO_2, SnO, Fe_2O_3, PbO and Ag_2O at elevated temperature is eminent as a bulk purification method for the corresponding metals. Accordingly, Huang *et al.* [9] suggest the following chemistry mechanism for the synthesis of ZnO nanowires to circumvent the high melting and boiling temperatures of the metal oxide:

1. Carbothermal reduction of zinc oxide by graphite to form zinc and carbon monoxide occurs at 925 °C. Since the melting point of zinc, 419 °C, is lower than the reaction temperature, zinc is rapidly evaporated into the vapor phase and is convected downstream by the inert argon gas to the catalyst particle.

$$ZnO_{(s)} + C_{(s)} \rightarrow Zn_{(v)} + CO_{(g)}$$

2. Vapor zinc is absorbed into the gold, forming a liquid alloy droplet due to the melting point depression in the *alloying* step of the VLS mechanism.

$$Zn_{(v)} + Au_{(s)} \rightarrow Au - Zn_{(l)}$$

3. Zinc at the surface of the liquid alloy droplet is oxidized by the carbon monoxide in the gas phase to form zinc oxide.

$$Au - Zn_{(l)} + CO_{(g)} \rightarrow Au - ZnO_{(l)} + C_xO_{y\ (g)}$$

4. Disproportionation commences to form liquid gold-zinc oxide alloy droplet and the crystalline zinc oxide *nucleate*. Crystalline nanowire results due to migration of zinc

oxide molecules to the lower energy site at the zinc oxide-gold interface and one-dimensional *elongation* of the nucleate. Here, an internal circulation loop within the liquid alloy droplet delivers zinc oxide to the nucleating interface and replenishes depleted zinc at the surface.

$$Au - ZnO_{(l)} \rightarrow Au_{(l)} + ZnO_{(s)}$$

The equations are not exclusively provided by Huang *et al.* [9]. They are conjectured by the author of this study based on the suggestion presented in the article. This chemistry mechanism has not been conclusively proven. Successful synthesis of other metal oxide nanowires based on the carbothermal reduction mechanism has been demonstrated [56].

2.2.2 The Vapor-Liquid-Solid Model

2.2.2.1 The Mechanism

The Vapor-Liquid-Solid growth process was proposed for nanowires grown by the catalyst-assisted method. First introduced by Wagner in the 1960s [49, 50] based on his observation of large single-crystalline whisker growth, this mechanism is later observed by many researchers studying the synthesis of one-dimensional structures. The VLS mechanism is divided into three distinct stages: (1) metal alloying, (2) crystal nucleation, and (3) axial growth. Figure 2.5 summarizes the VLS mechanism.

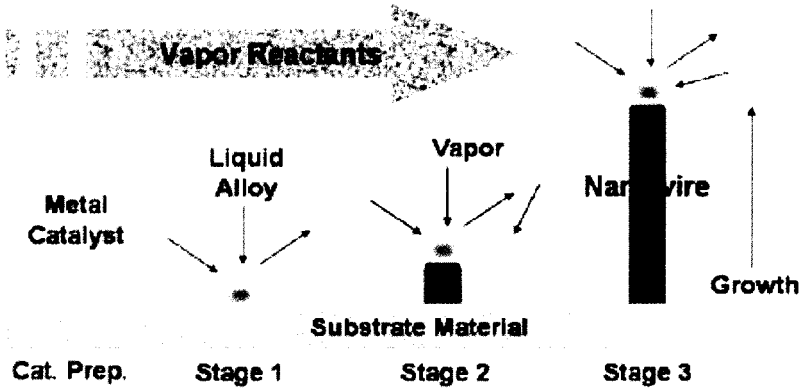

Figure 2.5. Schematic of the Vapor-Liquid-Solid Mechanism

Metal alloying happens early in the growth process. The reagent powder, such as a silicon, is vaporized and transported to the substrate by an inert gas, such as argon. At a suitable temperature, the reagent vapor dissolves itself into the metal catalyst, such as gold, on the surface of the substrate, forming a liquid alloy droplet. The melting temperature of the alloy is now lower than the melting point of the bulk catalyst material both due to the increase in surface area-to-volume ratio and the introduction of impurity. The alloy liquid droplet continues to absorb more reactant molecules from the gas stream until it reaches a bi-phase region of the phase diagram.

Supersaturation of the reactant material in the liquid alloy droplet denotes the *crystal nucleation* stage. As the concentration of the reactant material in the liquid alloy droplet reaches a critical value, the material begins to crystallize out of the alloy droplet. The nucleation process proceeds epitaxially at the surface of the substrate. Here, the preferred growth direction of the nanowire and crystal orientation of the substrate play an important role in determining the direction of the grown nanowires as they elongate above the substrate surface plane.

Once nucleation completes, the nucleus/liquid interface provides a low-energy site for further crystallization of the solute inside the alloy complex. As the nanowire elongates, the liquid alloy droplet is pushed from the bottom outward; thus, this process is named a "bottom-up" approach as opposed to the "top-down" semiconductor processing approach. During this process, deposition on the surface of the nanowire may promote diameter enlargement but this effect is essentially negligible. At the end of the growth process, as the reactor temperature cools down to room temperature, rapid temperature change may induce crystal defects at the head/body junction. Gradual solidification of the liquid alloy tip may minimize such defect formation.

2.2.2.2 In-situ Transmission Electron Microscopy Observations

Previously, the indirect evidence of the VLS mechanism is the presence of an alloy head at the end of a crystalline 1-D structure observed by scanning electron microscopy (SEM). Until the use of *in-situ* high-temperature transmission election microscopy (TEM), the progress of growth under VLS mechanism has never been irrevocably demonstrated.

In 2001, Wu and Yang [51] report the first direct observation by *in-situ* transmission electron microscopy during the growth of germanium nanowires on gold catalytic thin film. Figure 2.6 shows transmission electron microscopy images of the growth progress of a germanium nanowire with a gold catalyst particle. Figure 2.7 shows a schematic of the phase diagram of germanium in gold and where each stage occurs on the diagram.

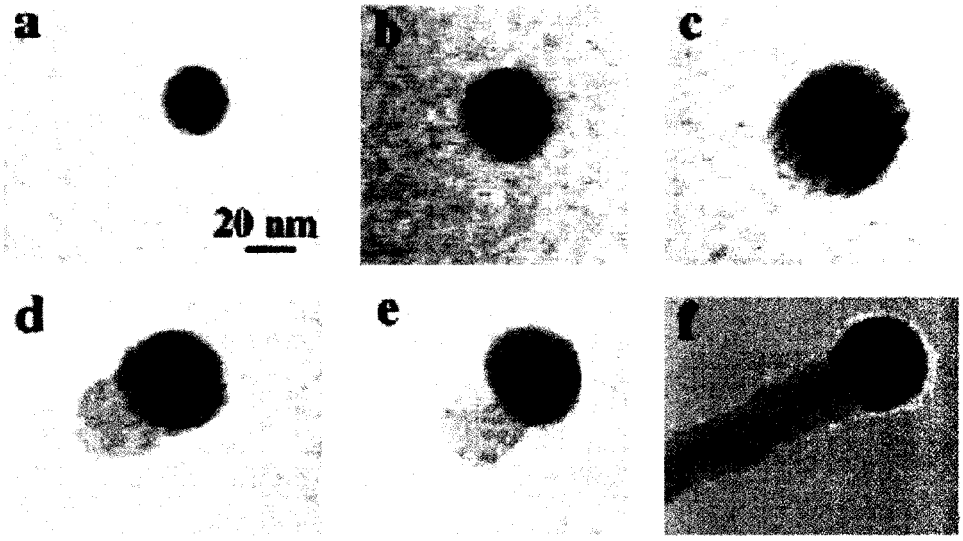

Figure 2.6. *In-situ* TEM images of VLS growth: (a) catalyst particle, (b) alloying initiation, (c) liquid alloy, (d) nucleation, (e) elongation, and (f) a germanium nanowire [51]. Scale bar is the same for all images.

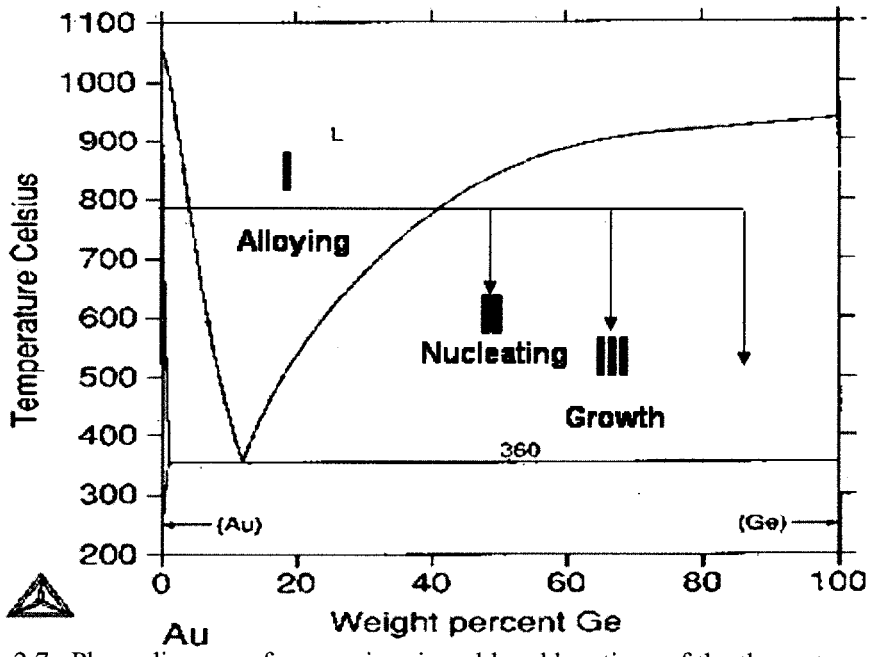

Figure 2.7. Phase diagram of germanium in gold and locations of the three stages [51].

In their study, Wu and Yang [51] grow germanium nanowires inside a high-temperature TEM. For preparation, micrometer-sized germanium particles are dispersed on TEM grids together with solution-made monodispersed gold nanoclusters of an average diameter of 20.2 ± 3.1 nm. The grids are placed inside the JEOL CX200. And real-time progress of the reaction is recorded. Wu and Yang [51] draw several important observations regarding the three growth stages.

During the *alloying stage* the volume of the alloy droplets increases and the elemental contrast decreases due to the dilution of heavier-metal gold with lighter-metal germanium. Based on the volume change, the authors calculated the germanium weight percentage to be 50-60 % at the commencement of the *nucleation* stage.

According to the equilibrium binary phase diagram, precipitation of germanium should begin at Ge weight percentage of 40 %, shown previously in Figure 2.7. Thus, Wu and Yang [51] conclude that *nucleation* occur under supersaturation condition. During *axial growth*, incoming germanium molecules preferentially diffuse to and condense at the solid/liquid interface because it is at lower energy level compared to the initiation of a new nucleus.

When the reactor is cooled down to room temperature, energy dispersive X-ray spectroscopy (EDX) shows the composition of the tip matches qualitatively well with the estimated alloy composition at which the first germanium nanocrystal nucleates. Wu and Yang also note in this study that there is a linear relationship between the wire diameters and the gold nanocluster diameters. The wire diameters are generally several nanometers larger than the nanocluster diameters.

Thus, if a phase diagram is readily available for the nanowire growth material and a metal solvent, the difficulty in selecting the catalyst material and a feasible temperature is alleviated. This catalyst-assisted growth mechanism is observed both for the chemical vapor deposition method and the laser ablation method for many growth materials and catalytic metals. The controlling parameters for the VLS mechanism will be analyzed thoroughly in Chapter Three.

2.2.3 Epitaxial Growth

During the *nucleation* phase of the Vapor-Liquid-Solid mechanism, the nanowire material, i.e. metal oxide, exists as a supersaturated solute inside the liquid catalyst/metal oxide alloy. There, the metal oxide molecules adsorb to the crystal lattice of the substrate and form a nucleation site. As the *elongation* phase proceeds, the metal oxide molecules migrate within the liquid alloy droplet to the nucleation site and form crystalline structure. The growth process is epitaxial.

In epitaxial growth, the lattice spacing between atoms in the crystalline substrate and the crystalline nucleate should be closely matched to ensure a regular transition in atomic arrangement from the substrate to the nucleate. If lattice mismatch is great, the interface will be irregular and weak, causing poor adhesion for thin film deposition or causing high crystal defect density in the as-grown material. For nanowire synthesis, inferior adhesion merely poses an insignificant issue since the surface contact area and volume of the nanowire are diminutive. Similarly, the difference in thermal expansion coefficients of the two materials does not cause post-synthesis problem due to the enhanced rate of thermal dissipation enabled by high surface area-to-volume ratio. The obvious issues are

the control of the orientation of the nanowires respective to the substrate surface, as shown in Figure 2.10, and electrical conductivity between the substrate and the nanowires if both are conducting materials.

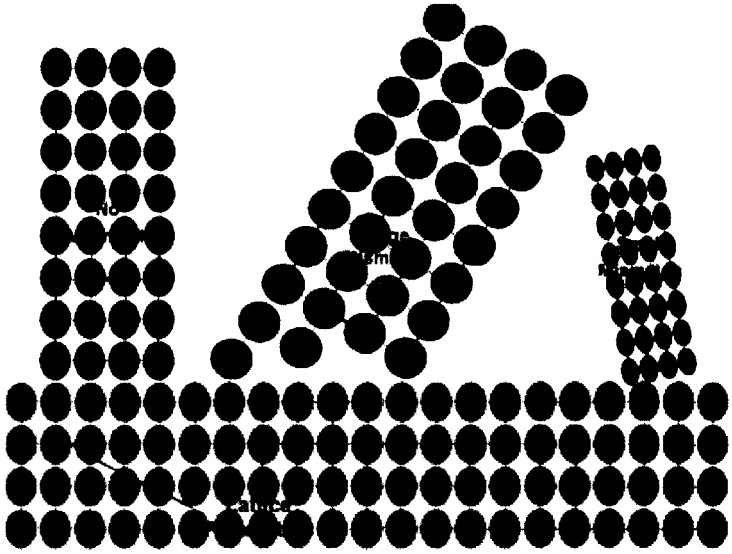

Figure 2.10. Lattice mismatch and growth orientation in a simple cubic structure system.

Understanding heteroepitaxy allows the researchers a greater control of the orientation of the nanowires. Assuming a wide range of substrates is readily available, the angle between the nanowires and the surface of the substrate can be adjusted to the whim of the knowledgeable researchers. Also, a mono- or di-atomic layer of a different material can be sandwiched between the substrate and the nanowires to adjust the growth direction; such layer is called a "buffer" layer.

2.3 Remarks

The wealth of the literature suggests that the catalyst-assisted vapor transport process via the vapor-liquid-solid mechanism is superior to physical vapor deposition and the oxide-assisted mechanism. The oxide-assisted mechanism produces nanowires with high defect density and it offers minimal control over growth orientation, localization, and final diameter of the wires. Physical vapor deposition can produce crystalline structures but localization is mostly random and diameter control is unaccommodating. On contrary, the vapor-liquid-solid mechanism offers nanowires with high crystallinity and maximum control over diameter, length, and localization. The only disadvantage of this method is the presence of the alloy tips in the as-grown wires. In some applications, the metal alloy tips may not be desirable and their removal is a challenging task.

Epitaxial growth, inherent with the vapor-liquid-solid mechanism, produces nanowires with high crystallinity. The lattice mismatch between the crystalline substrate and the crystalline nanowires is a determining factor in the growth orientation of the nanowires. Coupled with carbothermal reduction, the catalyst-assisted vapor transport process is an effective method of synthesis of metal-oxide nanowires. The subsequent Chapter Three discusses in details the critical parameters of VLS growth.

CHAPTER THREE - LITERATURE REVIEW

CRITICAL PARAMETERS FOR METAL-OXIDE NANOWIRE SYNTHESIS VIA VAPOR-LIQUID-SOLID MECHANISM

3.1 Metal Oxide Nanowires in the Literature

Table 3.1 lists various high-temperature synthesis methods of some transparent-conducting-oxide (TCO) nanostructures since the focus of this study is on tin-doped indium oxide nanowires from commercially available granular 9:1 weigtht ratio indium-tin oxide.

Table 3.1: High-temperature synthesis of various metal oxide nanowires

Reference	Materials	Method and Condition	Structures	Dimensions
Huang *et al.* (2001)	ZnO	VLS with gold catalyst at 900-925 °C constant Ar flow, 1:1 ZnO/C powder source, 5-30 min	NWs	D = 80-120 nm L = 10-20 μm.
Sun *et al.* (2003)	SnO_2	Evaporation at 800 °C, 100 sccm Ar, pure Sn powder, 120 min.	N-belts	t = 10-30 nm W = 60-250 nm L = μm - mm.
Dai *et al.* (2002)	SnO_2	Evaporation at 1050-1150 °C, 100 sccm Ar, Sn/SnO powder.	NWs N-ribbons N-tubes	Varied
Pan *et al.* (2001)	In_2O_3	Evaporation at 1400 °C, 50 sccm Ar, 300 Torr, In_2O_3 powder, 120 min.	N-belts	t = 10-30 nm W = 50-150 nm L = 10-500 μm.
Pan *et al.* (2001)	CdO	Evaporation at 1000 °C, 50 sccm Ar 300 Torr, In_2O_3 powder, 120 min.	N-belts & sheet	Varied
Zhou *et al.* (2003)	In_2O_3	VLS by laser ablation of InAs target with gold catalyst.	NWs	D = 10-50 nm (Controlled) L = 5 μm.

Hitherto, most 1-D structures of metal oxides were synthesized by simple evaporation-condensation at high temperature. As shown in Table 3.1, synthesis by VLS mechanism produces crystalline nanowires whereas synthesis by simple thermal evaporation

produces various structures, such as nanowires, nanobelts, and "nano"-sheets. Due to the various justifications cited earlier, growth via VLS is attempted for tin-doped indium oxide nanowires. For catalyst-assisted chemical vapor deposition via the vapor-liquid-solid mechanism, experimental data from numerous groups provide information on the effects of process parameters on the morphology of the nanowires. A literature review on the critical process parameters which influence synthesis via the vapor-liquid-solid mechanism is presented in Section 3.2.

3.2 Critical Parameters in Vapor-Liquid-Solid Growth

Based on the VLS model, it is apparent that temperature, pressure, gas flow rate, size of catalyst particles, the crystallographic orientation of the surface of the substrate, and reaction time all play important roles in determining the morphology of the as-grown nanowires. In the following sub-sections, the effects of these parameters, as well as others, are presented.

3.2.1 Temperature

Based on their previous publications, as well as the existing literature, Wu *et al.* [52] conclude that, in principle, synthesis of nanowires of various compositions is feasible if suitable solvents and appropriate growth temperatures are determined. A good solvent material allows formation of a liquid alloy with the desirable material for nanowire growth at a reasonably practical temperature. A temperature range where eutectic liquid alloy formation, between the metal solvent material and the nanowire material, exists is recommended. Growth temperature should be selected between the eutectic point and the

melting point of the alloy [52]. The effect of temperature on growth and morphology of nanowires has been reported in the literature. Huang *et al.* [9] report significant overgrowth in terms of length and diameter of the nanowires at higher temperature. However, no quantitative data or SEM images are provided.

In a study performed by Chen *et al.* [19], gallium nitride nanowires are grown using molten gallium at temperature of 800 - 1050 °C in an ammonia ambient at atmospheric pressure on (1 0 0) silicon or quartz substrates, as shown in Figure 3.1. The authors report the following observations. Broader diameter distribution is obtained under fast heating rates (> 100 °C/min) and narrower diameter distribution is produced under slow heating rate (25 °C/min) for metal powders of Fe, Co and Ni. Optimum growth temperature is observed to be approximately 910 °C. Nanowires with poor crystallinity and amorphous solid are formed at temperatures below 850 °C. At temperatures higher than 1050 °C, growth is minimal.

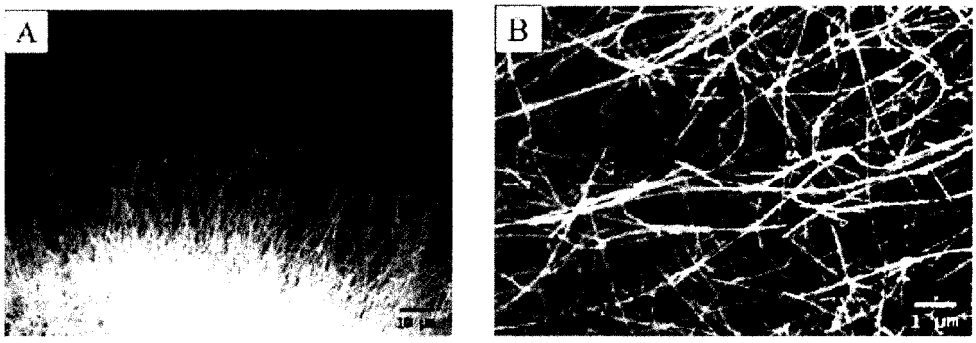

Figure 3.1. Cross-section SEM image of GaN nanowires on a substrate. (a) Edge and (b) top-view [19].

Evidently, both the growth temperature and the temperature ramp-up rate significantly modulate the growth phenomena. The VLS model indicates the existence of a process window for temperature. At a temperature below the lower limit, generation of the source material, "quasi-"melting of the metal catalyst, or alloy formation may be prohibited. At a temperature above the upper limit, excessive supply of thermal energy increases the kinetic energy of the vapor-phase and liquid-phase source material. Excessive thermal leads to reversible reactions, reversible nucleate formation, and evaporation of the source molecules from the liquid alloy droplet.

Furthermore, "premature nucleation" and amorphous film growth may result if the nucleation stage occurs before coalescence of the gold film to form gold bumps completes, at lower temperature and faster ramp-rate, when a catalyst thinfilm is used instead of colloids. Additionally, competition between growth by physical vapor deposition and growth by catalyst-assisted chemical vapor deposition may intensify at lower temperature, as explained in Chapter Two, leading to the presence of amorphous material on the surface of the substrate, along with the nanowires.

3.2.2 Thinfilm Thickness and Colloidal Size

Abundant publications suggest that the diameter of a nanowire is modulated by the size of the alloy droplet, which is dictated by surface energetics and thermodynamics. Here, the physical size of the catalyst material, the ambient temperature and pressure, and the nanowire materials all play important and interacting roles. For thinfilm coating of the catalytic material, film thickness directly correlates to the diameter of the alloy droplets. As the temperature ramps up, the thin film of metal catalyst breaks apart to

form metal bumps on the surface of the substrate, as described in Appendix D. The degree of coalescence is a function of the film thickness, surface tension of the liquid metal catalyst, the wetting properties, the temperature ramp-up rate, and the ambient conditions. For rigid control, monodispersed metal nanoclusters are recommended since the average diameter of the nanoclusters is readily controlled and the diameter distribution is also, ideally, narrower.

For synthesis of zinc oxide nanowires on gold-coated silicon substrate, Huang *et al.* [9] find that thinner gold film thickness generally lead to smaller diameters, as shown in Figure 3.2. However, no direct correlation is presented.

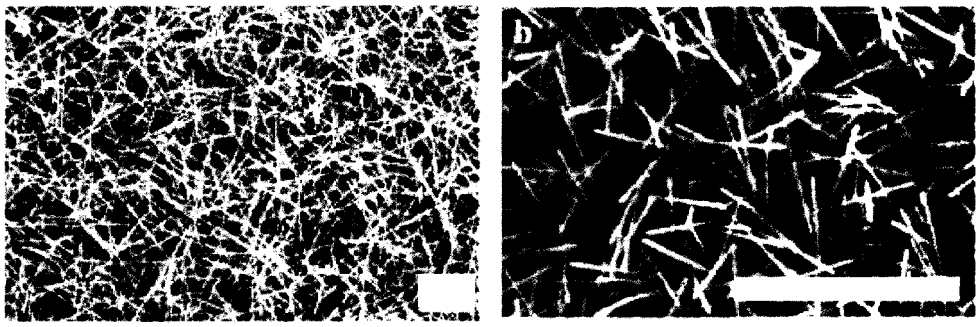

Figure 3.2. ZnO nanowires with different Au film thickness. (a) 50 nm thick coat and (b) 30 nm thick [9]. Scale bars are 4 microns.

In the study [9], the gold-coated silicon substrates are not annealed prior to the growth process. It is postulated that the diameter distribution of the gold particles formed on the surface of the substrate will be more consistent with an additional annealing step prior to the growth step. Assuming the surface condition of the silicon substrate is pristine, thermodynamics dictates the minimum radii of the gold droplets as well as their distribution if the gold-coated substrates are pre-annealed. However, if the coalescence

of gold film occurs simultaneously as the reactants diffuse into the liquid alloy droplets during temperature ramp-up, then the surface tension of the individual droplets will vary if the process is mass-transport-limited. Furthermore, if the temperature ramp-up rate is too fast, then sufficient time may not be allocated for complete coalescence of the gold droplets. Therefore, the minimum radius, the average radius, the radius distribution, as well as the aerial uniformity of the wire distribution, will be inconsistent.

Since gold thin film offers wider diameter distribution and less exact control of the average droplet size, other researcher groups opt for monodispersed metal colloids to study the correlation between size of metal particles and average diameter of nanowires. In Cui *et al.* [17], silicon nanowires are grown on the SiO_2 substrates coated with Au nanoclusters, having nominal diameters of 5, 10, 20 and 30 nm. Silicon nanowires are grown in a quartz reactor at ~440 °C for 5-10 min with 10 - 80 sccm flow of SiH_4 (10% in helium gas).

For each subset, the average diameter of the nanowires is slightly larger, approximately 1-2 nm, than the average diameter of the gold nanoparticles. There is a linear dependency of the average diameter of the nanowires on the average diameter of the gold nanocluster, as evident in Figure 3.3a. Figure 3.3b schematically depicts the dependence of wire diameter on catalyst particle diameter. As expected, dispersity of the wires mirrors the dispersity of the nanoclusters, as shown by AFM and FE-SEM analysis in Figure 3.4. In Figure 3.4b, HR-TEM measures an average wire diameter of 10 nm with a metal complex at the tip. The clear lattice fringe confirms a single-crystal structure of the nanowire. Selected-area electron diffraction reveals crystallographic

structure. Stacking faults are found generally in wires with large diameters, not in wires with small diameter.

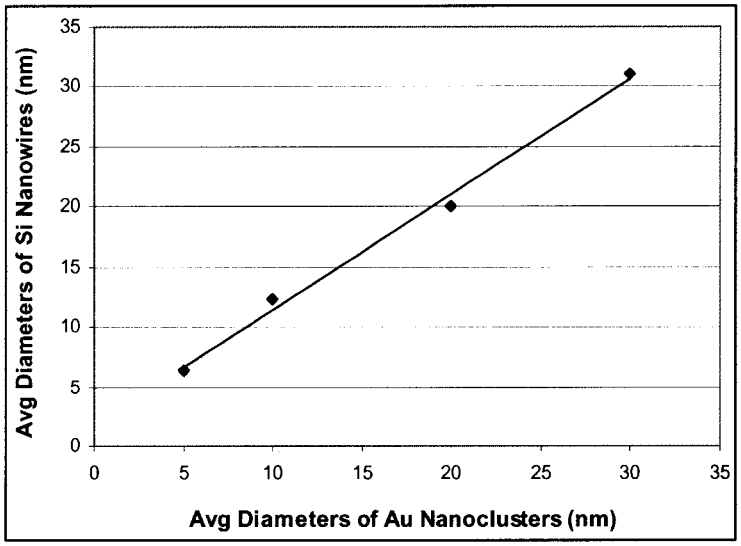

Figure 3.3. Dependence of diameter of Si NWs on diameters of the nanoclusters [17].

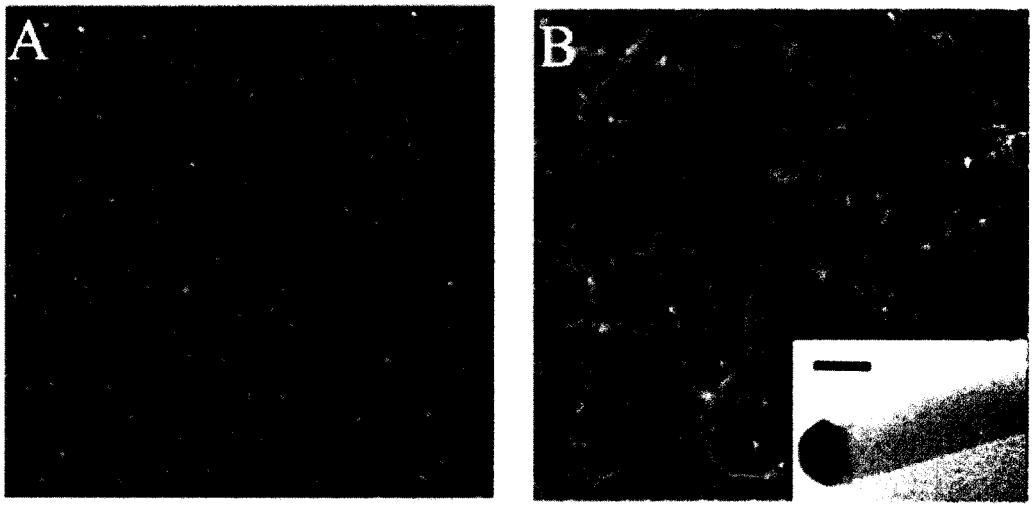

Figure 3.4. Correlation between distribution of Au colloids and distribution of Si NW. (a) AFM image of well-dispersed gold nanoclusters. (b) SEM of nanowires grown from 10 nm-diameter gold particles. Inset is the HRTEM image of the tip with the gold catalyst head. The scale bar is 20 nm [17].

In Gudiksen *et al.* [53], indium phosphide nanowires are grown on silicon wafers with gold nanoclusters by laser ablation. Dispersivity of the nanoclusters is verified with AFM prior to growth. The substrate is placed inside a quartz tube, downstream of a solid InP source, which is located external to the furnace to minimize thermal evaporation of the InP source. The furnace temperature is maintained at 650 - 700 °C, with the temperature of the surface of the substrate at 500 - 600 °C. The source is ablated with an ArF excimer laser (Lambda Physik, 193 nm) and the vapor is convected to the substrate by inert argon gas at 100 sccm.

From TEM analysis, the diameters of the crystalline core for different diameters of gold nanoclusters are collected. Figure 3.5 shows the nanowire growth directed by gold colloids average diameters of 10, 20, and 30 nm, respectively. The Gaussian distributions of the diameters coincide well with the distributions of the gold colloids. Figures 3.6a schematizes a positive correlation between them. Figure 3.6b depicts the dependence of the wire length on the reaction time. It is interesting that the spread of the diameter distribution of the wires is smaller than that of the nanoclusters. Outside of the crystalline core is an amorphous oxide layer of 2-4 nm in thickness, as shown in Figure 3.6d, this thickness is relatively constant for all wires, within a set of experiment. This coat is assumed to be formed by oxidation with air after removal from the furnace.

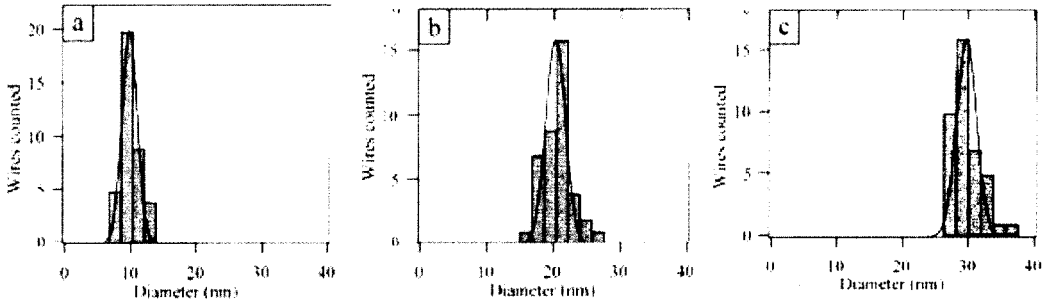

Figure 3.5. Correlation of diameter of InP NWs and diameter of Au colloids, with average diameters of (a) 9.7±1.0, (b) 19.9±3.0 and (c) 30.0±6.0 nm [53].

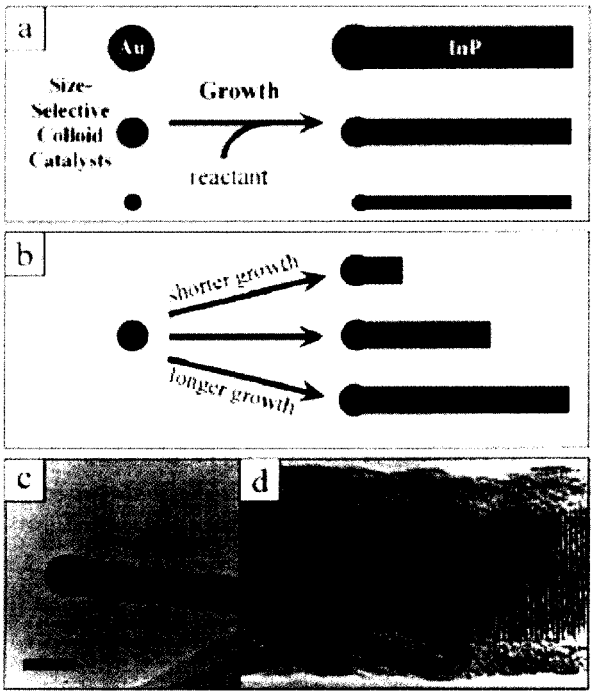

Figure 3.6. InP nanowires by catalyst-assisted laser ablation. (a) Dependence on catalyst sizes, (b) dependence on reaction time, (c) TEM image of a wire with metal catalyst head, and (d) HR-TEM shows crystalline structure and an outer oxide sheath [53].

Thus, the diameter of the as-grown nanowires directly correlate to the physical size of the alloy droplets, which depends on either the thickness of the deposited catalyst film or the average size of the catalyst colloids. Successful diameter control requires accurate

control of the average diameter of the alloy droplets and its distribution. Solution-based monodispersed nanoclusters can be used to control the nanowire aerial density also. Dilution of the concentrated solution is the key in controlling the distribution density of the nanoclusters on the surface of the substrate. However, direct localization of the nanowires requires precise placement of the catalyst spot, which is possible with e-beam lithography and lift-off process.

3.2.3 Reaction Time

According to the VLS model, longer reaction time will result in longer wire length. Growth in the radial direction should be minimal since only the axial growth is catalyzed. Huang *et al.* [9] report significant crystal overgrowth for longer growth time, in both directions. Thus, some non-catalyzed epitaxial deposition directly on the surface of the body of a nanowire occurs.

In Chen *et al.* [19], rod-like structures are synthesized when reaction time is 3 hours. From 3 - 12 hours, the rod-like structures elongate in the axial direction to form wire-like structures. These wire-like structures are longer in length, yet smaller in diameter. The diameters of the wires drastically increase if reaction time is longer than 12 hours. For reaction time greater than 48 hours, bulk GaN crystals of unusual shapes are observed. The dependence is shown in Figure 3.7.

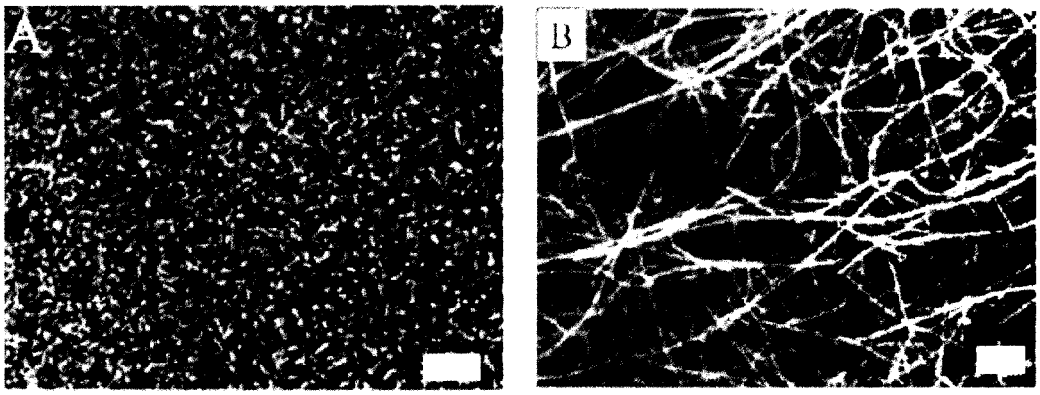

Figure 3.7. GaN NWs by vapor transport. (a) Rod-like structures having average diameter of several hundred nm after 3-hr growth, and (b) "typical" NWs having diameter range of 20-50 nm [19]. Scale bars are 10 and 1 micron(s), respectively.

Gudiksen *et al.* [53] also study the effect of growth time on nanowire length. Although the synthesis method is laser ablation instead of chemical vapor deposition, the results are pertinent nonetheless, because the growth mechanism is VLS. In laser ablation, the vapor source is generated by laser ablation of the solid source; whereas, in chemical vapor deposition, the source is vaporized thermally or via carbothermal reduction. In this study, InP nanowires are synthesized at various growth times using gold nanoclusters of 20 nm average diameter. Figure 3.8a-c show SEM images of nanowires grown at different durations and Figure 3.8d plots, quantitatively, the nanowire length versus the laser ablation (growth) time.

As growth time increases, the number of wires also increases. The nucleation stage of this VLS growth proceeds after 1 - 2 minutes because a finite period of time is required for complete saturation of the alloy droplets. After this stage, the wires elongate at a fairly constant rate, producing wires of well-defined lengths and narrow distribution.

Also, the aerial distribution is denser at longer growth time. This phenomenon could be explained with rapid elongation rate after the first slower nucleation stage.

The authors do not report enlargement of the diameter or presence of amorphous bulk material, compared to Huang *et al* [9] and Chen *et al.* [19]; perhaps, the growth time is not sufficiently long for those phenomena to happen or vapor-phase concentration of growth material is not relatively high.

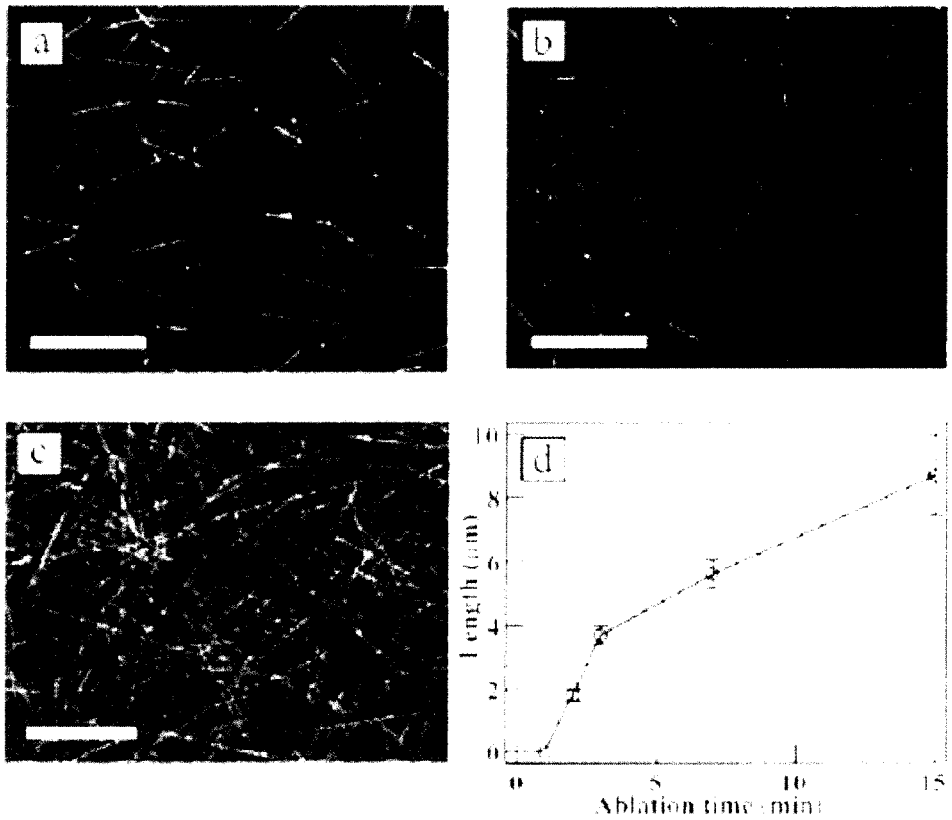

Figure 3.8. InP NW morphology on growth time. (a) 3 min, (b) 7 min and (c) 15 min. All scale bars represent 5 μm. (d) Plot of Length vs. Reaction Time [53].

3.2.4 Substrate Orientation

In general, nanowires have a preferred direction of growth. For growth of ZnO nanowires on (111) silicon substrate in Huang *et al.* [9], TEM images measure spacing of 2.56 ± 0.05 Å between adjacent (002) crystal planes and indicate <001> as the growth direction, as shown in Figure 3.10. This result is also confirmed by x-ray diffraction (XRD).

From Figure 3.2, the ZnO nanowires do not grow perpendicularly to the surface of the substrate. Although it is not obvious from Figure 3.2 and not reported in the paper, it is likely the angle is 45° because the <001> preferred growth direction is at an angle of 45 degrees to the (111) plane of the silicon substrate.

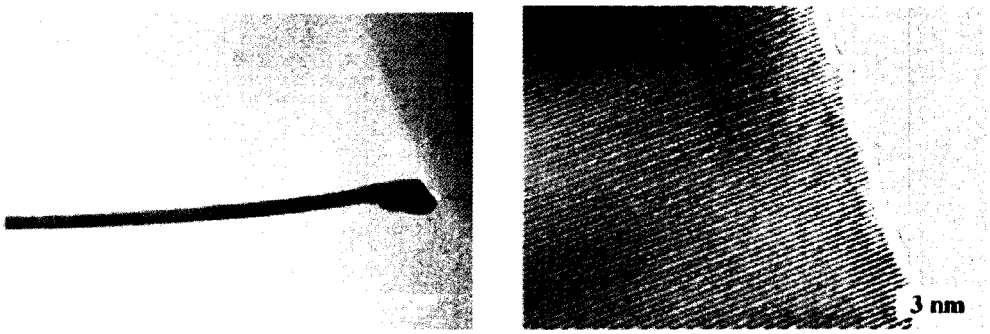

Figure 3.9. TEM image of a ZnO NW. (a) With an irregularly shaped Au/Zn alloy tip. (b) HR image showing high crystallinity [9].

In Cui *et al.* [17], it is observed that smaller Si NWs prefer the [110] growth orientation; whereas, larger wires almost exclusively prefer the [111] orientation. These preferences suggest competing catalyst/Si nanowire interface and Si nanowire surface energetics; thus, the authors recommend additional analysis.

Wu *et al.* [52] suggest a method to grow vertically aligned nanowires when such growth is desirable. To grow vertically aligned nanowires, the substrate which have the surface plane orientation perpendicular to the preferred growth direction of the desired nanowires must be selected, i.e. (111) Si substrate for Si nanowires and (110) sapphire substrate for ZnO nanowires (for ZnO case, the lattice mismatch between the ZnO *a* axis and the sapphire *c* axis is less than 0.08% at room temperature [52]). And the reaction conditions must be controlled in such a way that the growth is epitaxial so the wire will elongate out of the plane once nucleation is complete. Figure 3.10 shows vertical growth of ZnO nanowires on the *c*-plane of a sapphire substrate is attainable.

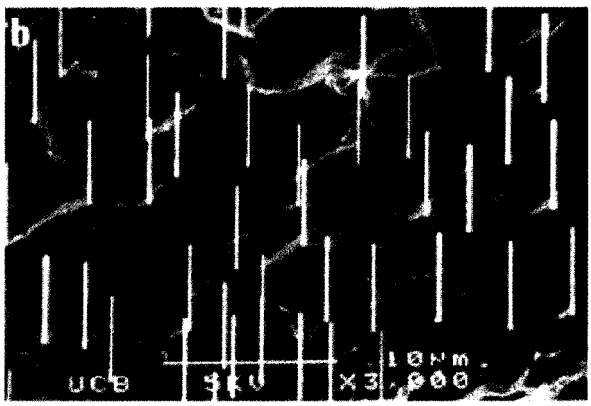

Figure 3.10. Vertical elongation ZnO NWs on *c*-sapphire [16].

3.2.5 Type of Metal Catalysts

According to the VLS growth model, growth is dependent on the liquid alloy formed by the growth material and the catalyst metal. Thus, for each type of catalyst metal, the growth temperature is different for the same nanowire material, depending on the phase diagram. Unless the alloys of the nanowire material and all various metals possess similar surface energy and form liquid alloy droplets of the same average diameter at the

tested temperature, the liquid alloy droplets from different metals should have different average diameters and, thus, different wire diameters. However, Chen *et al.* [53] report a very intriguing phenomenon.

In Chen *et al.* [54], metal powders and alloys of In, Co, Ni, Fe, Ni/Co, and Fe/Co can all be used to produce copious amount of GaN nanowires. The authors find that diameters and lengths of nanowires are not a function of these metal catalyst materials. The range of the wire diameter is 50 – 150 nm. Unfortunately, Chen *et al.* [19] neglect to report the mesh size of these metal powders, whether the powder particles are well-dispersed on the surface of the substrate or not, and the growth temperature for each metal catalyst. If all of the tested metal powders have the same average diameters, which is very likely, and if the metal colloids are widely separated, then the reported phenomenon is easier to digest. Thus, further information and confirmation of the results are imperative.

3.2.6 Reducing Agent

In Huang *et al.* [9], an experiment is conducted to test the effect of the reducing reagent. The authors find that hydrogen reduction of the ZnO powder yields smaller wires than carbothermal reduction of ZnO, as shown in Figure 3.11. Direct hydrogen-reduction of the source is achieved by flowing diluted hydrogen gas over the oxide source and carbothermal reduction is by thermal evaporation of a mixture of graphite powder and ZnO powder. Hydrogen-reduction growth produces long and curvaceous wires. Occasional coils within a long wire are evident in Figure 3.11c.

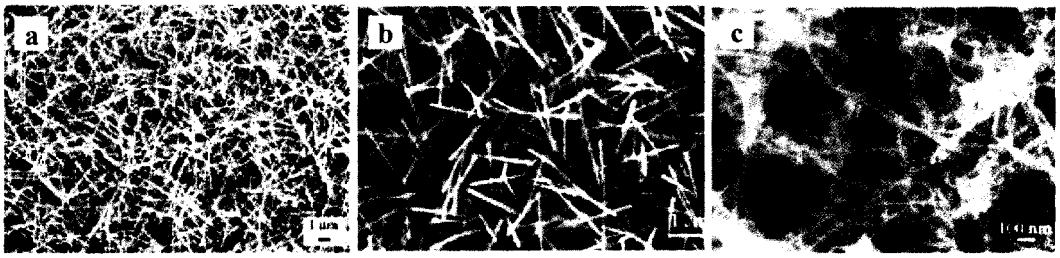

Figure 3.11. Hydrogen reduction versus carbothermal reduction on ZnO NW growth.
(a) On substrate with 50 nm of Au coat by carbothermal reduction,
(b) On substrate with 30 nm of Au coat by carbothermal reduction, and
(c) By hydrogen thermal reduction of the source instead [9].

The smaller diameter of the nanowire can be explained by the fact that hydrogen in the carrier gas can effectively reduce the ZnO source as well as the ZnO nanowires. The wires are curvy because they are long and small; thus, they can not mechanically support themselves to be straight. The increased concentration of reactant in the carrier gas, relative to the case of carbothermal reduction, can lead to faster elongation rate and, consequently, tremendously longer length.

3.2.7 Source-Substrate Separation

Ideally, all of the vapor-phase reactant material will be transported to the substrate by the carrier gas and form nanowires. Realistically, loss of the reactant materials will occur via physical deposition on the wall of the reactor on the way to the substrate and the mass transport limitation prevents most of the vapor reactant from arriving at the substrate. Thus, efficiency of the process could be low. Different researchers have performed studies on the effect of the separation between the source and substrate in a tube reaction chamber.

Huang *et al.* [9] observe that shorter nanowires and some nanoparticles are present in regions "closer to the reagent source." Nanowires of diameter range of 80 - 120 nm and length range of 10 - 20 μm are found on the substrate at unknown distance away from the source. Since the surface temperature as a function of the distance from the source is not reported, it is difficult to rationalize the phenomenon. If temperature is independent of the distance from source, then longer, bigger, and denser nanowires should be located closer to the source due to the relatively higher concentration of reactant in the carrier gas. However, if temperature varies along the length of the tube reactor, then more information is necessary.

In another study performed by Chen *et al.* [54], diameter distribution of nanowires is found to be a strong function of the separation distance between the source and the substrate. For separation distance of 1 cm, diameters of nanowires are in the range of 50 - 150 nm. When the separation distance is increased to 10 cm, diameter distribution reduces to 20 - 50 nm. This result is more consistent to the mass-transport phenomena, as explained earlier.

3.2.8 Flow Rate of Carrier Gas and Ambient Pressure

No detailed study on the effects of flow rate of carrier gas and the ambient pressures is reported in the literature. Based on mass-transport analysis, it is expected that larger, longer, and denser nanowires will be synthesized at higher ambient pressure due to the increased local concentration of the reactant. At excessively high pressure, amorphous bulk growth may be an undesired consequence.

However, the dependence on the flow rate of the carrier gas is not as apparent because it also depends on the evaporation rate of the reactant from the source, which is a function of growth temperature and source mix ratio for the case of carbothermal reduction. "Slow" evaporation rate, coupled with faster flow rate, leads to lower partial pressure of the reactant in the gas phase. "Medium" evaporation rate with faster flow rate also lead to dilution of the reactant in the gas phase but the dilution may be compensated with better mixing due to turbulence flow, if present, faster delivery, and reduced mass-transfer boundary layer thickness. Increased flow rate for a source having "fast" evaporation rate may not noticeably affect wire growth at all, unless gas flow dynamics affect wire morphology. Thus, interactions between carrier gas flow rate, ambient pressure, temperature, and source mix ratio are expected.

3.2.9 Positional Control (Localization)

Huang *et al.* [9] shows patterning of the gold film allows localization of nanowire growth. In Figure 3.12, nanowires at edge of hexagonal patterns form bridges crossing from one hexagon to the next. These wires have diameters of approximately 50 - 200 nm and lengths of over 50 μm. This shows that it is feasible to connect two conducting metal pads with the nanowires. Thus, a sensor device can be easily fabricated if the connection is profuse and stable.

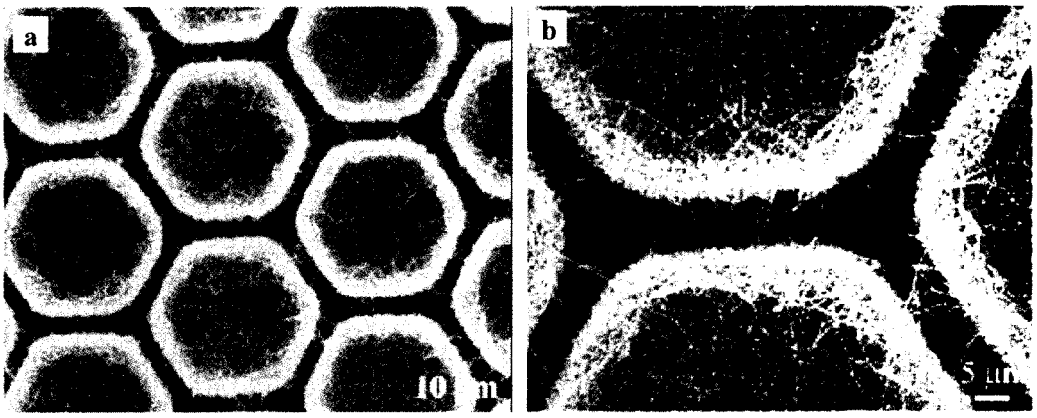

Figure 3.12. Localization of ZnO NWs by patterning of the Au thinfilm [9].

Wu *et al.* [51] suggest a local vapor pressure gradient near the nanowire causes the bridging of gold islands by zinc oxide nanowires in Figure 3.12 because nanowire growth is facilitated in the direction of higher vapor pressure. The local pressure gradient can be achieved by forming liquid alloy droplets bridging the metal solvent and the nanowire source material. Figure 3.13 also shows localization of nanowires by patterning the catalyst thin film [55].

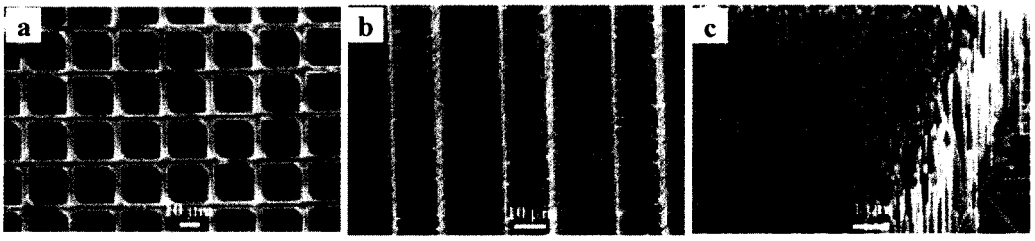

Figure 3.13. Site-selective growth of ZnO NWs. The pattern of the array is defined by conventional photolithography [55].

3.3 Summary

Experimental data from various research groups provide a general guideline for nanowire synthesis of new materials via the vapor-liquid-solid growth. There is a process window for temperature, beyond which growth is not feasible. The average diameter and dispersivity of the nanowire depends on the thickness of the catalyst thin film or the average diameter and concentration of the mono-dispersed catalyst colloids. Localization can be achieved by patterning of the catalyst materials.

Thus far, the VLS reaction is controlled by mass transport. Any process conditions that increase the local concentration of the vapor reactant over the surface of the substrate, i.e. shorter separation distance between source and substrate, proper source mix ratio, or higher temperature for thermal evaporation of the source, will increase growth rate and aerial uniformity. Longer reaction time results in longer length and, in some cases, larger diameter and bulk growth. Growth orientation of the wires can be controlled by determining the preferred growth direction of the nanowires and properly selecting a substrate whose surface crystal plane forms the desired growth angle with the preferred growth direction.

Generally, the as-grown nanowires should have high crystallinity from the epitaxial growth. Excessive amorphous or polycrystalline growth on the surface of the substrate is highly undesirable. Diameter and length distributions should be uniform over the surface. And importantly, the optoelectronic properties must be consistent within each run and repeatable over multiple runs.

CHAPTER FOUR – MATERIALS AND METHODS

TIN-DOPED INDIUM OXIDE NANOWIRES: SYNTHESIS AND CHARACTERIZATION

4.1 Research Hypothesis and Objective

4.1.1 Hypothesis

Synthesis of tin-doped indium oxide nanowires via carbothermal reduction and the catalyst-assisted epitaxial growth on sapphire substrate is feasible, at appropriate reaction temperature, substrate surface, and carrier gas flow rate.

4.1.2 Objectives

Synthesis of tin-doped indium oxide nanowires via carbothermal reduction of ITO powder and the vapor-liquid-solid mechanism will be attempted. Upon successful growth, the effects of thickness of catalyst thinfilm, reaction temperature, and carrier gas flow rate on nanowire morphology will be characterized. Crystallographic and parametric analyses will be performed on the nanowires.

4.2 Experimental Procedure and Analysis

4.2.1 Calibration

4.2.1.1 Volumetric Flow Rate of Carrier Gas

The gas flow rate was controlled by a MKS Instruments Mass-Flo® controller (MFC), which was calibrated using argon gas by manufacturer. The flow rate was set and read via a MKS 247 Type 4-Channel Readout.

Qualitative confirmation of the flow rate using an inverted water-filled graduated cylinder, a NIST-traceable VWR® stopwatch, and a rubber hose was performed and the result confirmed the MFC readout.

4.2.1.2 Reaction Temperature

The horizontal tube furnace, Lindberg/Blue M, Model# TF55035A, is equipped with a Eurotherm Model 2416 temperature controller. This tube furnace functions both as an annealing furnace for the gold-coated sapphire substrates and the high-temperature reaction chamber for the synthesis. The quartz tube fits snugly inside the chamber. The ends of the tube protrude out of the chamber since the length of the chamber is 16 in and the length of the quartz tube is 24 in.

Since temperature control and read-back is based on only one thermocouple at the center of the reaction chamber, it is highly suspected that temperature variation along the length of the chamber exists; however, due to lack of a high-temperature oxidation-resistant thermocouple, the temperature variation along the length of the boat (7.5 cm), which is situated at the center of the chamber, was not determined and assumed to be minimal.

4.2.2 Synthesis Procedure

(a) A thin film of gold (Alfa Aesar, 99.95% purity) was sputtered on a 0.5 cm x 0.5 cm (or 1.0 cm x 1.0 cm) sapphire substrate using the IBS/TM200S Ion Beam Sputterer with a thickness set point, controlled by a quartz crystal resonator, ranging from 1 nm to 10 nm. Henceforth, the Au-coated sapphire sample is referred to as the "substrate."

(b) Granular tin-doped indium oxide (Alfa Aesar, 10 wt% SnO_2 & 90 wt% In_2O_3, 99.99% purity) was mechanically pulverized and blended with synthetic graphite powder (Alfa Aesar, conducting grade, 99.9999% purity) in 1:1 weight ratio using the NIST-traceable APX-1000 scale from Denver Instruments with a measurement accuracy of 0.1 mg. Henceforth, the mixture is referred to as the "source."

(c) The source was placed four-centimeter upstream of the sapphire substrates from step (a) inside the tube furnace. Growth was performed at various reaction temperatures, various argon (Air Product, electronic grade, 99.999% purity) flow rates, and a fixed reaction time of 60 minute. The reaction apparatus is shown in Figure 4.1. The egress of the quartz tube was capped with metal fittings to ensure minimal temperature and air-flow perturbation. Rubber O-rings were installed at both ends to ensure an air-tight fit between the metal fittings and the quartz tube.

(d) Samples were SEM-inspected for growth. EDX, XPS, and TEM analysis were performed on substrates having dense growth.

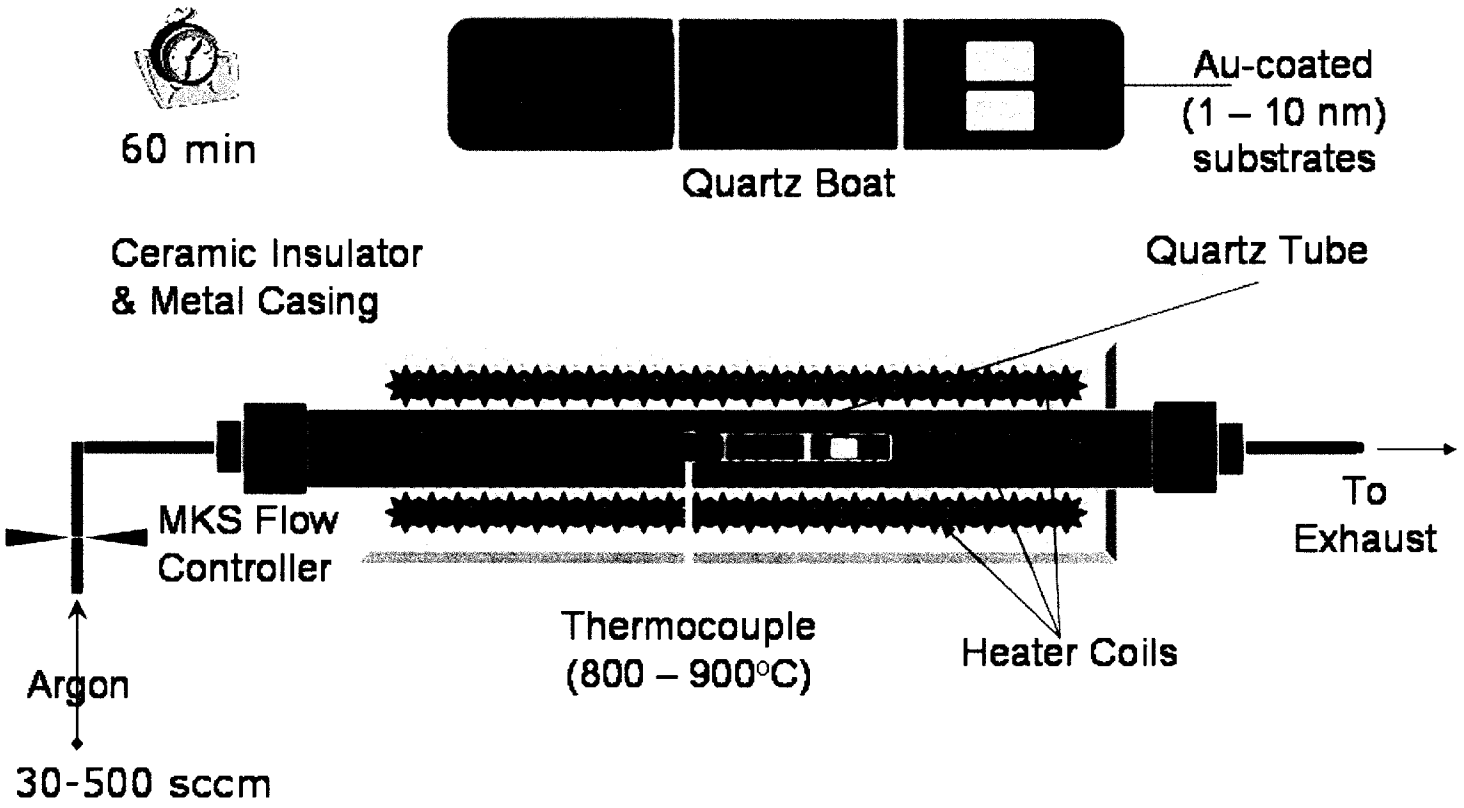

Figure 4.1. Reactor apparatus for ITO NW synthesis.

4.3 Experimentation

4.3.1 Phase 1: Feasibility of Synthesis

Since synthesis of ITO nanowires has not been reported in the literature, an exploratory experiment was conducted to explore the synthesis feasibility. As shown in Table 4.1, all variables, except temperature were held constant. The reaction temperature was varied until growth is observed. Characterization experiments proceeded after successful synthesis was observed.

Table 4.1. Nanowire Synthesis – Preliminary Experiments

TEMPERATURE (°C)	ARGON FLOW RATE (sccm)	GOLD FILM THICKNESS (nm)	SAPPHIRE PLANE	REACTION TIME (minutes)	ITO:Graphite Mix Ratio
700-1000	300	2	A/M-PLANE	60	1:1

As control group to verify the validity of the assumption that the synthesis is driven by carbothermal reduction and the VLS mechanism, the highlighted experiments were conducted.

4.3.2 Phase 2: Characterization study

To study the effects of temperature, carrier gas flow rate, and substrate crystal structure on as-grown morphology, the following sets of experiments were designed. The reaction time, source mix ratio, and gold film thickness were maintained constant at 60 minutes, 1:1, and 2 nm, respectively. In the first set, the temperature was incremented from 790 °C to 940 °C in 30 °C intervals at 300 sccm argon flow rate and *a*-sapphire substrate. In the second set, *m*-plane and *a*-plane sapphire substrates were used at a fixed

temperature and argon flow rate. Here sapphire was chosen due to the low miscibility of gold in sapphire and the commercial availability of various crystallographic planes, facilitating synthesis and the study of heteroepitaxy, respectively. In the final set, the carrier gas flow rate was incremented from 100 sccm to 500 sccm in 200 sccm intervals at constant temperature and *a*-sapphire.

4.4 Data Collection and Analysis

The data collection included morphology analysis, which focuses on uniformity, growth orientation, length, diameter, and crystal structure, and the electronic property analysis, which measures the dopant concentration and the resistivity of the wires. The *diameter distribution* and *length distribution* were determined from FE-SEM micrographs. Upon completion of each run, the uncoated samples were imaged by a Hitachi S-4000 at 20 kV and 20 Amps. Images were taken at various locations, as shown in Figure 4.2.a by the author.

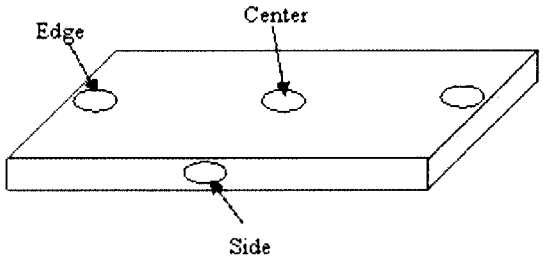

Figure 4.2.a. SEM sampling locations on a substrate

The distribution of diameter and length was determined by measuring the "width" and "length" of the image of the wire on the SEM images taken at a magnification of 20k for a given area. Since SEM magnification is not as impressive as TEM and the size of the nanowires ranges from 50 to 100 nanometers, an assumption is explicit where the

"width" of the image of the wire is representative of the "diameter" the nanowires, although the crystal structures of indium oxide and tin oxide are cubic bixbyite and rutile tetragonal, respectively. This will not be absolutely correct, unless TEM measurement is done. The mean and standard deviation were calculated for the diameter using the formulas in Table 4.2. A histogram for the diameter distribution was generated. Since the reaction time was fixed at 60 minutes, the elongation rate directly correlates with the average length of the wires.

Table 4.2. Data analysis formulas

Formula Description	Mathematics
Mean	$m \equiv \frac{1}{n}\sum_{k=1}^{n} x_k;$
Standard Deviation	$s_N = \sqrt{\frac{1}{N}\sum_{i=1}^{N}(x_i - \bar{x})^2}.$

To determine the average diameter of the catalytic head and the body of the nanowires using SEM images, the following procedure was performed. Microsoft™ PowerPoint® was employed to view the digital images at 400% magnification. A judicious selection of wires was performed to eliminate the nanowires which are out of the plane of focus, as shown in Figure 4.2.b. Based on the length scale intrinsic with the image, an extrinsic scale was created, as shown in Figure 4.2.c. Using this extrinsic scale, the diameter was measured with the scale aligned perpendicular to the growth axis, as shown in Figure 4.2.c.

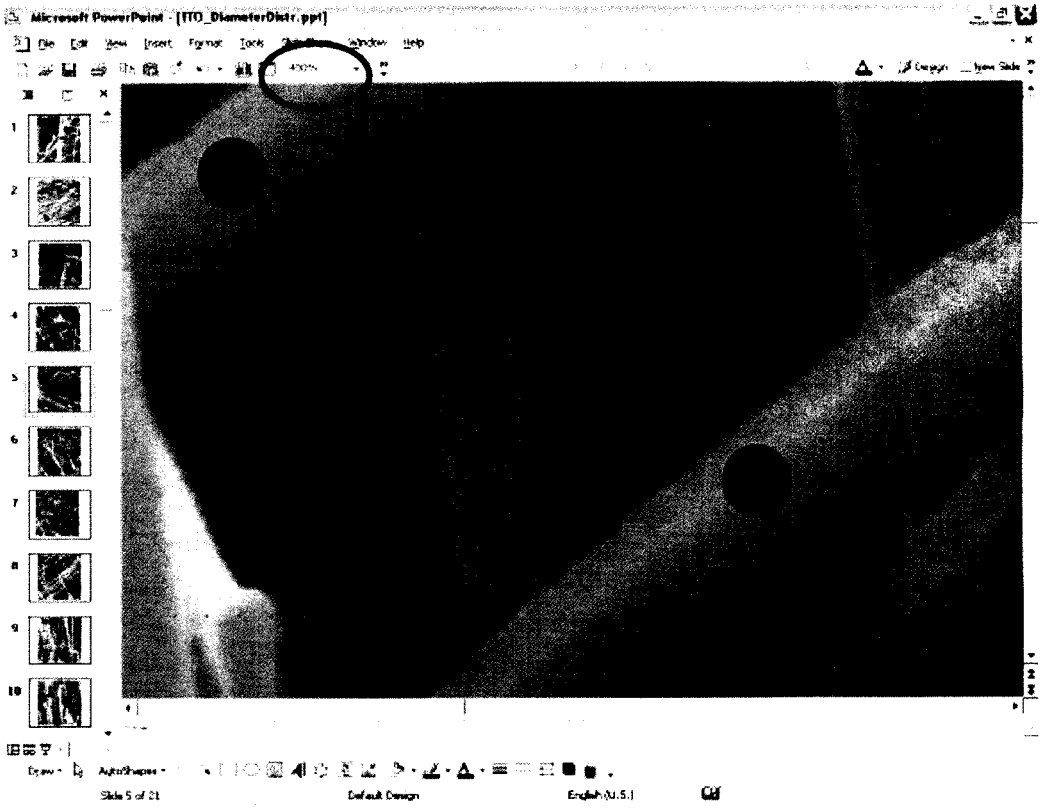

Figure 4.2b. Selection of NW for diameter measurement: happy face indicates fitness for diameter measurement and unhappy face indicates the reverse.

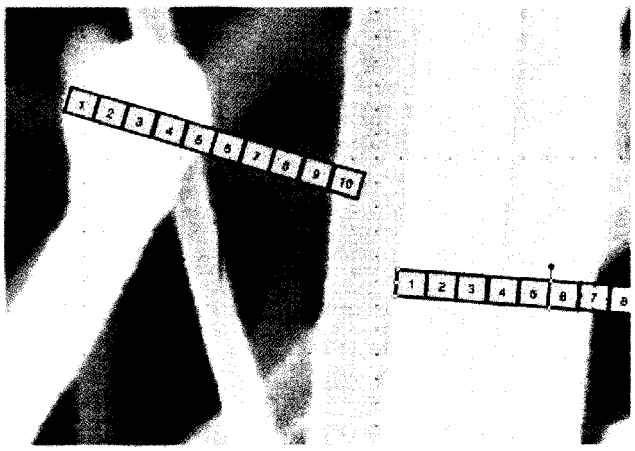

Figure 4.2c. Extrinsic scale for diameter measurement, created based on the intrinsic scale of the image.

Composition analysis was performed using Energy-Dispersive X-ray (EDX) with a Phillips CM-20 transmission electron microscope (TEM). The high resolution capability, spot size range of 9 – 25 nm, of the TEM rendered a much more accurate composition analysis than the SEM, as the SEM EDX analysis would reveal only bulk composition rather than nanowire composition. This analysis was conducted by Jing Kong of Stanford University.

To confirm the TEM EDX analysis result, an X-ray photoemission spectroscopy (XPS) study was performed using an SSI S-Probe Monochromatized XPS Spectrometer with Al (Kα) radiation as the probe under a vacuum pressure of ~1.0 E-10 Torr by the author. XPS composition analysis was furnished by the S-Probe ESCA software. Curve fitting of the indium, tin, and oxygen peaks were performed by Hou Tee Ng of NASA Ames Research Center. Correction to the charging effects was performed using the adventitious C peak at 285.0 eV. A Shirley background correction was applied to each spectrum before the curve fitting. The extent of Gaussian-Lorentzian mixing was allowed to vary freely and the consistency in the curve fitting was maintained by executing the fits with different starting parameters.

The electrical properties of the nanowires were measured by the author as followed. To extract the nanowires from the substrate, the sample was suspended in an acetone solution and sonicated by five pulses of thirty-second durations with thirty-second separation. The nanowire suspension solution was dispersed onto a pre-fabricated contact pad, kindly provided by Jing Kong, via a micropipette. Here, the highly-doped silicon substrate serves as the back gate; the 50 nm silicon dioxide coat serves as the gate

oxide; and the 5 nm gold pads serve as the source and drain. This labor-intensive procedure involved an iterative cycle of dispersion of the suspension and confirming the presence of the nanowire across the contact pads. With the nanowire establishing a bridge across the pads, as shown in Figure 4.3.a, the semiconductor behavior was measured using the Agilent 4156B semiconductor parametric analyzer. Figure 4.3.b shows a schematic of the device.

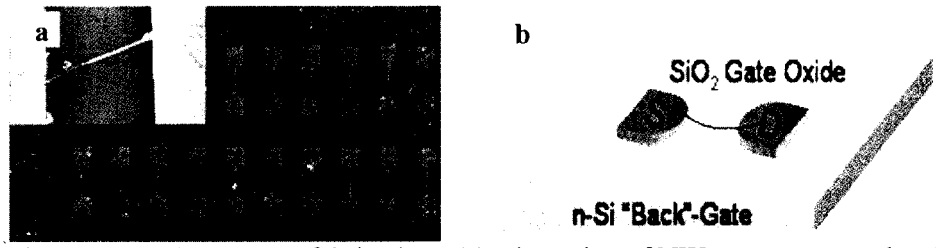

Figure 4.3. ITO NW FET fabrication. (a) Dispersion of NWs on contact pad and (b) Schematic of FET device with highly doped silicon substrate as the backgate.

Further insights into the crystallographic structure of the nanowires were obtained using high-resolution TEM and selective area electron diffraction (SAED). Images were taken by Jing Kong, with the accelerating voltage at 200 kV. Based on the transmission electron micrograph, the crystallinity of the nanowire can be inferred from the lattice fringes on the micrograph. Any amorphousness is visible on the micrograph. Calculations from the diffraction pattern were performed by Hou Tee Ng of NASA Ames Research Center to determine the preferred growth direction of the nanowire.

CHAPTER FIVE – RESULTS AND DISCUSSIONS

INDIUM-DOPED TIN OXIDE NANOWIRES

5.1 Synthesis Challenges and Solutions

5.1.1 Uniformity improvement

Various challenges were encountered while attempting to synthesize the nanowires. The first challenge arose when the repeatability of nanowire morphology was poor with a narrow feasible temperature process window of approximately 10 °C and dismal uniformity. Repeatability was improved and the feasible temperature window widened by introducing oxygen contamination into the system. The original set-up required installing metal fittings at the exit end of the quartz reaction chamber to minimize temperature and pressure fluctuations. The opening was only 0.20 inch in inner diameter, which minimized diffusion of atmospheric oxygen into the system as the flow rate of the carrier gas was maintained at 300 sccm. The oxygen contamination was introduced by removing the metal fittings at the exit end, increasing the egress diameter from 0.20 inch to 0.95 inch. The extra molecular oxygen contamination appears to have enhanced the oxidation reaction and stabilized the growth. Along with larger process window, the optimum temperature was shifted down by approximately 30°C. This is attributed to the increased availability of oxidative power, both in terms of oxygen presence and higher reactivity of oxygen, compared to carbon dioxide, which was generated by the carbothermal reduction process.

The second challenge was to improve the uniformity of the nanowires across the same substrate. Initially, the 1 cm^2 substrate was placed at the bottom of the third chamber horizontally. The uniformity using this set-up was relatively poor as shown in Figure 5.1. In Figure 5.1.a, high density of wires having average length six microns are consistently at the leading side of the substrate; lower density is observed at the edge. In Figure 5.1.b, towards the center, growth density becomes sparser, average length shorter (< 1 μm), and diameter and length distributions wider. In Figure 5.1.c, at the trailing edge, the density and average length (~ 1.5 μm) are diminutively increased; however, diameter and length distributions remain wide.

The apparent mass transport limitation was alleviated by positioning the substrate at a slanted angle by leaning it against the separation wall of the second and the third chambers, as shown in Figure 5.2. Appendix C provides a brief fluid dynamics discussion. The new set-up also appeared to improve repeatability and diameter uniformity, as well, by comparison of Figure 5.2.c with Figure 5.6.a.

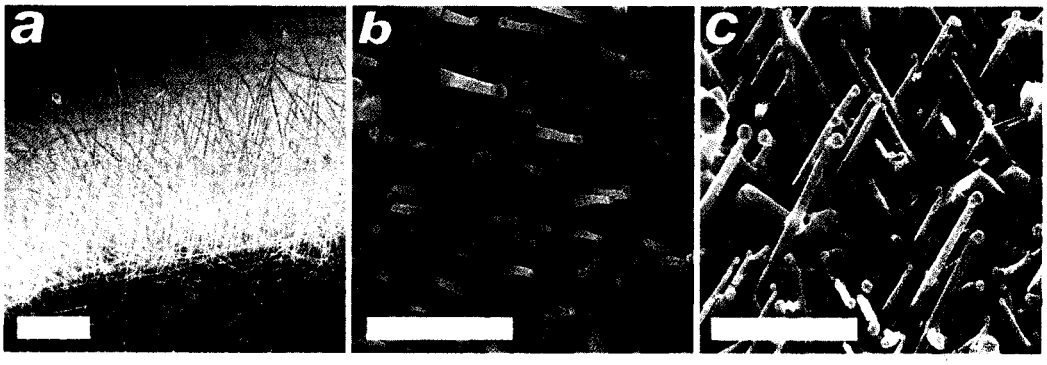

Figure 5.1. Growth nonuniformity within the same substrate. (a) Leading edge, (b) center, and (c) trailing edge of substrate. Scale bars are 2 μm.

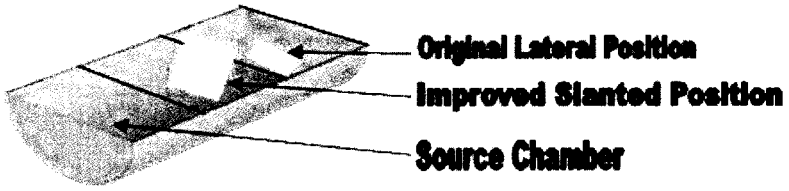

Figure 5.2. Schematic of boat showing the before and after positions.

5.1.2 Diameter control

To explore the dependence of the average diameter on thickness of the gold thinfilm, a set of experiments was performed using identical process parameters except gold film thickness, where it was controlled to be 1, 2, 3, and 5 nm. Figure 5.3 shows the nanowire distribution at the center of the 1 cm^2 *a*-plane sapphire substrate. It confirms the observation reported in the literature that average diameter correlates positively with gold film thickness. A comparison of Figure 5.3, with the horizontal substrate position, and Figure 5.5, with the new slanted substrate position, further demonstrates improved density, reduced diameter and length ranges, and enhanced growth rate with the new set-up.

Upon close inspection of Figure 5.3, it appears that thinner thickness lead to higher density; whereas, thicker film leads to low density and more apparent polycrystalline oxide film on the surface of the substrate. Possible explanations include incomplete fragmentation of the gold thinfilm, amalgamation of the gold droplets, and competition between catalyst-directed 2-D growth and catalyst-directed 1-D growth. Further studies are recommended. Some possible experiments are: *in-situ* monitor, pre-annealing the substrates, varying the temperature ramp-up rate, and time study.

Experiment without gold thinfilm as the catalyst at same conditions resulted in no nanowire growth or polycrystalline deposition at all. Due to charging effect caused by the exposed surface of the insulator Al_2O_3, SEM images were not taken. Thus, these results suggest that a metal catalyst is critical for the incorporation of the materials from the gas-phase into the liquid and, ultimately, the solid phase. The catalyst also provides a template and an environment for epitaxial growth to proceed.

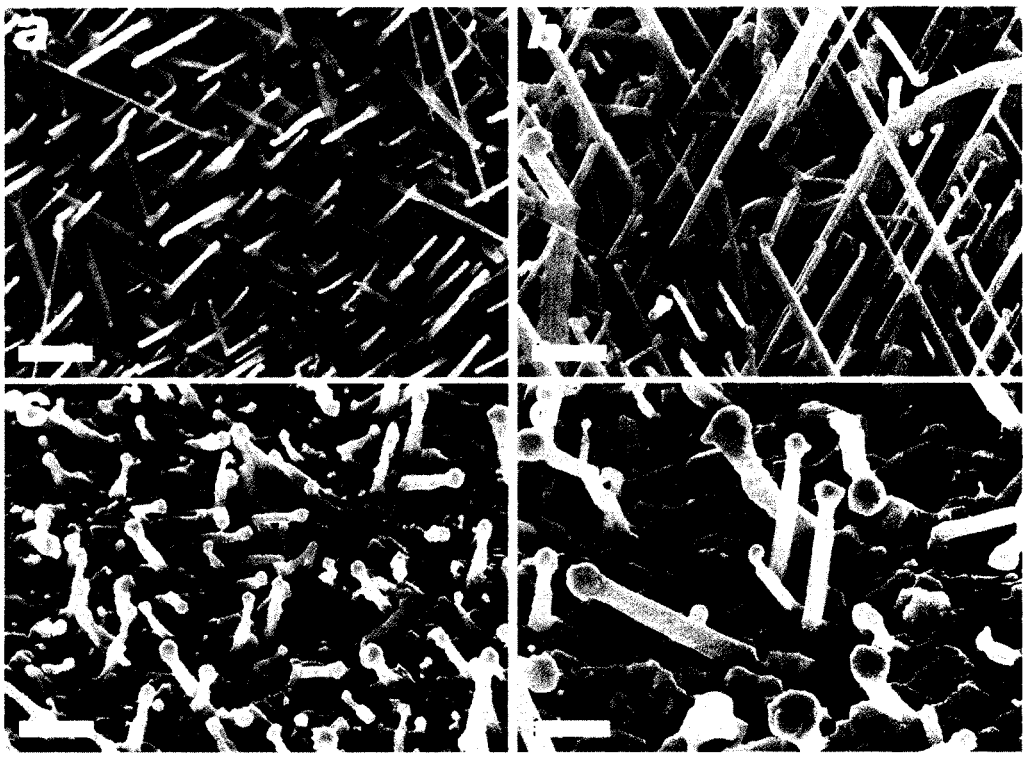

Figure 5.3. Dependence of morphology on gold thinfilm thickness. (a) – (d) are 1, 2, 3, and 5 nm, respectively. Images taken at center of substrates. Scale bars are 1 μm.

5.1.3 Feasibility of reusing source

The third set of experiments was performed to determine whether the source can be reused. Here, the 0.5 gram of 1:1 source mixture was reused three times for one hour reaction time each with the old set-up. Figure 5.4 suggests that the source become either depleted or "deactivated" after the first run, as nanowires were produced with a new source, sparse and short nanowires were produced with the once-used source, and a polycrystalline film was produced with the twice-used source. Deactivation may occur due to recrystalization of the various oxides in the source at elevated temperature, deactivation of the graphite powder or incomplete evaporation of the metal, producing a physical barrier for carbothermal reduction. Other possibilities exist as well. Due to the observed negative relationship, new source is recommended each run to enhance repeatability.

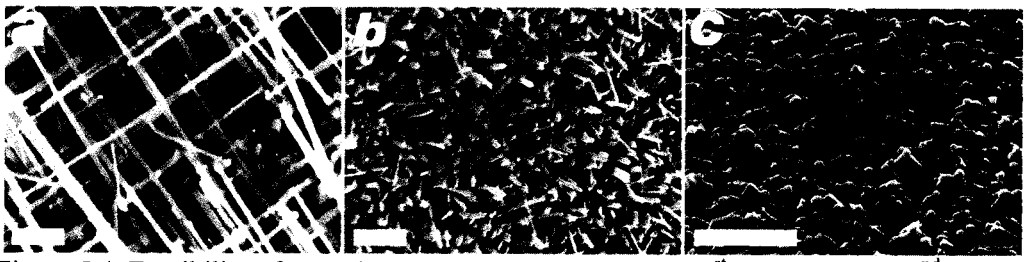

Figure 5.4. Feasibility of reused source. (a) New source, (b) 1st repeat, and (c) 2nd repeat. Scale bars are 1 μm.

5.1.4 Carbothermal reduction

The following set of experiments was performed to deduce the vapor-generation mechanism at the source. The result suggests that metal oxide vapors are generated by both carbothermal reduction and physical evaporation. To simulate physical evaporation at the reaction conditions under which carbothermal reduction also proceeds, mixtures of

powdered ITO and 0.05μ γ-alumina powder were subjected to identical reaction parameters. Alumina (Al_2O_3), a chemically stable oxide having a high melting temperature of 2000°C, is not expected to undergo a redox reaction with ITO at reaction conditions.

"Thinfilm" deposition and some nucleates were observed with 1:1 weight ratio mixture of SnO and In_2O_3 powders and 1:1 weight ratio mixture of ITO and 0.05m γ-Al_2O_3 powders, as shown in Figure 5.5 - this result suggests some physical evaporation of the ITO at reaction temperature or self-catalytic redox reaction of the tin (II) oxide, as explained in Chapter Six. As shown in Figure 5.5.c, nanowire morphology similar to Figure 5.6.a was observed when SnO/C source was used. However, no growth was observed for SnO_2/C or In_2O_3/C source under the "optimized settings" listed in Table 5.1.

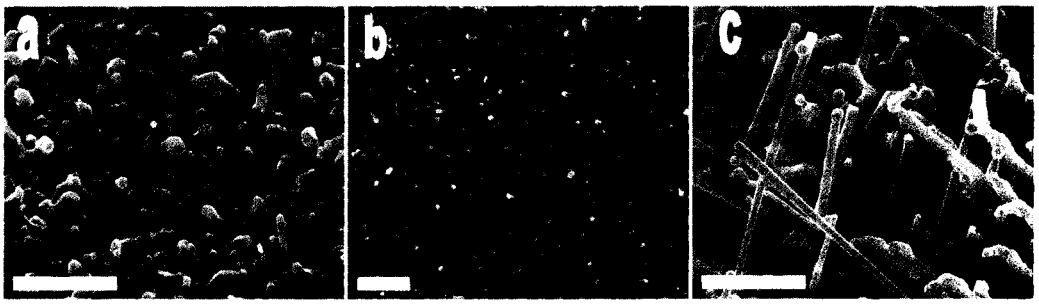

Figure 5.5. Carbothermal reduction of oxide source. (a) 1:1 SnO and In_2O_3, (b) 1:1 ITO and 0.05m γ-Al_2O_3, and (c) 1:1 SnO and C. Scale bars are 1 μm.

Nonetheless, carbothermal reduction of the metal oxide powder indeed ensues at reaction temperature. Increase in average length and growth density of NWs was observed when the source was prepared by mixing pulverized ITO with graphite powder, as opposed to only ITO powder or ITO/Al_2O_3 powder mixture. Furthermore, when 1.500 grams of graphite powder was baked at 1000 °C for 16 hours in argon ambient, only

0.026 grams was "consumed" and 1.474 grams remained. The 0.026 grams were assumed to be lost by material handling. However, when a mixture of 1.500 grams of graphite and 1.500 grams of ITO was baked at 1000 ^{o}C for 10 hours, only 0.860 gram remains. Assuming the source mixture was depleted of ITO, 0.64 grams of graphite was consumed. This is in stark contrast with the previous experiment. Thus, it was confirmed that graphite powder is consumed as the reaction proceeds. This set of experiments suggests that, in addition to physical evaporation, carbothermal reduction at the source generates vapor-phase tin, indium, and carbon oxide and oxidation of the metal vapor happens either in the gas phase or within the gold droplet to generate the metal oxide species critical for nanowire synthesis.

5.1.5 Preliminary findings

The previous data indicate that the following conditions should be applied for good repeatability of nanowire synthesis:

1. Graphite powder is required
2. Slanted substrate position
3. No end-cap metal fittings at egress
4. 2-nm gold thickness
5. New source for each run
6. Tin oxide in ITO is either "activated" or present in both SnO and SnO_2 forms.
7. Positive correlation between Au thinfilm thickness and wire diameter

Accordingly, subsequent characterization experiments were performed using the above guidelines.

5.2 Characterization Experiments

5.2.1 SEM Morphology

Successful synthesis of indium-tin oxide nanowires was achieved for the growth conditions tabulated in Table 5.1 and the modifications to the original set-up as described in Section 5.1. Despite this wide range of operating condition, good uniformity and density were achieved at a narrower range of temperature and carrier gas flow rate. Particularly, it was found that high-quality single crystalline nanowires were predominantly and reliably obtained within a relatively narrow temperature range of 840 – 880°C, a carrier gas flow rate of 250 – 350 sccm, a feedstock source/substrate distance of separation of 1 – 3 cm, and a gold thinfilm thickness range of 2 nanometers or less.

Table 5.1. In-SnO_2 nanowire synthesis conditions.

Parameters	**Feasible Range**	**Optimized Setting**
Temperature (oC)	800 – 900	840 – 880
Argon Flow Rate(sccm)	30 – 1000	250 – 350
Pressure (atm)	1.0	1.0
Gold Film Thickness (nm)	1 – 10	= 2

Composition analysis indicates the nanowires to be indium-doped tin (IV) oxide (In-SnO_2) instead of tin-doped indium (III) oxide. Figure 5.6 shows scanning electron microscopy (SEM) images of arrays of In-SnO_2 nanowires on *a*-plane sapphire substrate. Nanowires on *m*-plane sapphire substrate are shown in Figure 5.7.

All wires seem to possess smooth surface morphology with uniform diameter along the length of the growth axis, indicating single crystallinity. The alloy catalytic nanoparticles are located at the terminating growth front. Apparently, the diameter of the catalytic head is always larger than the diameter of the corresponding nanowire, as shown in Figure 5.8. Occasionally, very long wires run across the surface.

Although it is not unequivocally explicit on the SEM images, the nanowires possess a square cross-section, rather than a circular one, which is expected as the unit cell structures of indium oxide and tin oxide are cubic bixbyite and tetragonal rutile, respectively. At the junction between the catalytic head and the nanowire body, some kinks are visible on Figure 5.6.a, though none is visible in Figure 5.7.a. This is due to the more gradual cooling step implemented subsequently to reduce thermal shock during the temperature ramp-down phase.

It is noted that profuse growth, with greater density and longer length, is observed near the edge of the substrate, compared to the center of the 1 cm^2 sample, as shown in Figures 5.6.d and 5.7.d. The regularity of the array is no longer apparent in Figure 5.7.d because the nanowires cannot mechanically support themselves at longer length. Nonetheless, the "within sample" non-uniformity is much less pronounced compared to horizontally situated substrates. The uniformity can be improved by improving the gas-flow dynamics.

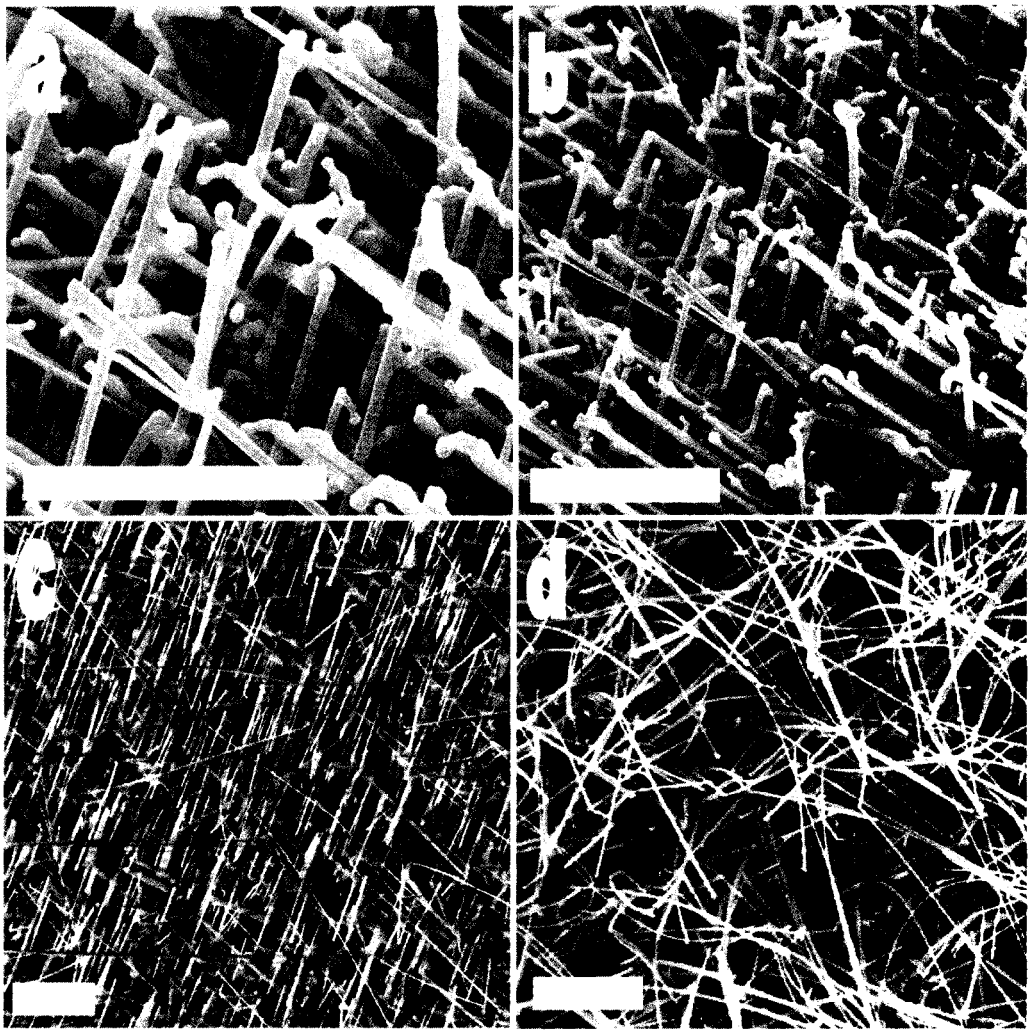

Figure 5.6. In-SnO_2 nanowires on *a*-plane sapphire. (a) – (c) "Center" locations having different magnifications. (d) "Edge" location. Scale bars are 2 microns.

The presence of the catalytic head, the crystallinity of the nanowires and the dependency of the directionality of the nanowires on substrate crystal structures demonstrate characteristics of the heteroepitaxial vapor-liquid-solid growth mechanism. In contrast to *a*-sapphire, the heteroepitaxial growth process results in an intricate cross-network of uniform In-SnO_2 nanowires on *m*-sapphire. Figure 5.7 shows a representative

SEM top-view image of a mesh-like nanowire formation. Higher resolution images further reveal formation of an almost three-dimensional regular matrix with individual nanowires growing mostly in directions orthogonal to each other.

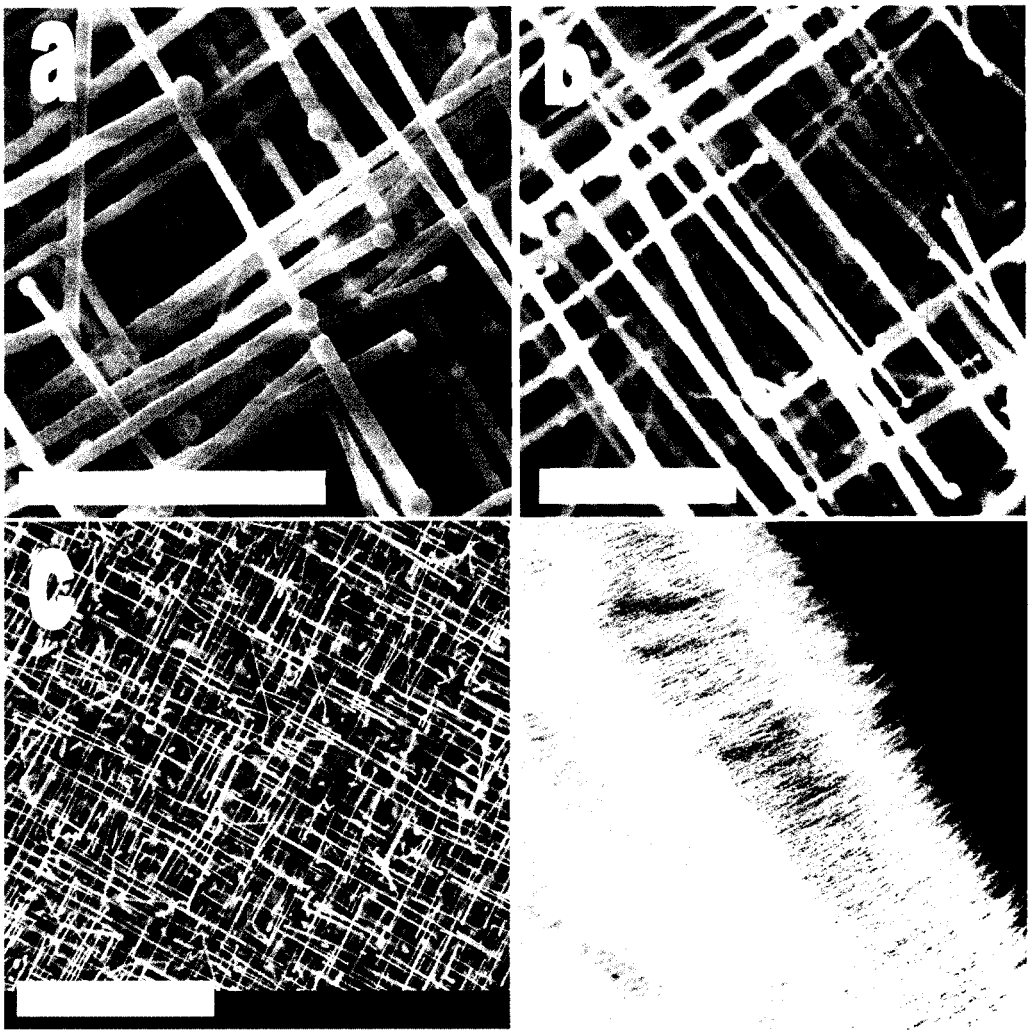

Figure 5.7. In-SnO_2 nanowires on *m*-plane sapphire. (a) – (c) "Center" locations, having different magnifications. (d) "Edge" location. Scale bars are 2 microns for (a) – (c) and 10 microns for (d).

As shown later, the main constituent of the nanowire is SnO_2. Heteroepitaxy dictates the growth direction of the nanowires on the two sapphire planes, resulting in different elongation angle. Lattice mismatch of the (1 0 0) plane of tetragonal rutile SnO_2 and the (1 1 0) *a*-plane of sapphire is approximately six percent, with the angle mismatch between the plane directions to be approximately 65°. This value agrees well with the observed angle. On the (1 0 0) *m*-plane of sapphire, the lattice mismatch is approximately two percent, with the angle mismatch between the plane directions of 45°, which also coincide with the observed value. Interested readers are referred to Ng *et al.* (2003) [56] for a more thorough discussion.

Figure 5.8 plots the diameter distribution histogram of both the nanowires and the catalytic heads at the center of the substrate. The average diameter of the nanowires is 94 nanometers with a standard deviation of 19 nanometers, whereas, the average diameter of the nanoparticles are 125 nanometers with a standard deviation of 32 nanometers. The diameter distributions appear to skew toward the lower range. Here, the diameter is measured using enlarged digital scanning electron micrographs, as discussed in Chapter Four; thus, the true average diameter may be slightly smaller due to the *square* cross-section instead of the *circular* cross-section. Furthermore, although strenuous efforts have been exerted to avoid shadowing and focusing effects, such effects may still produce inaccurate measurement.

Due to mass transport limitation, as well as growth kinetics, all wires are not expected to initiate growth simultaneously and uniformly across the surface of the substrate. Thus, wires at the edge of the substrate are observed to be longer than those at the center. This

is evident when comparing Figure 5.6.c to Figure 5.6.d and Figure 5.7.c to Figure 5.7.d. Here it is determined that, for the one-hour reaction duration, the average length ranges from two to ten micrometers from the edge to the center of the substrate.

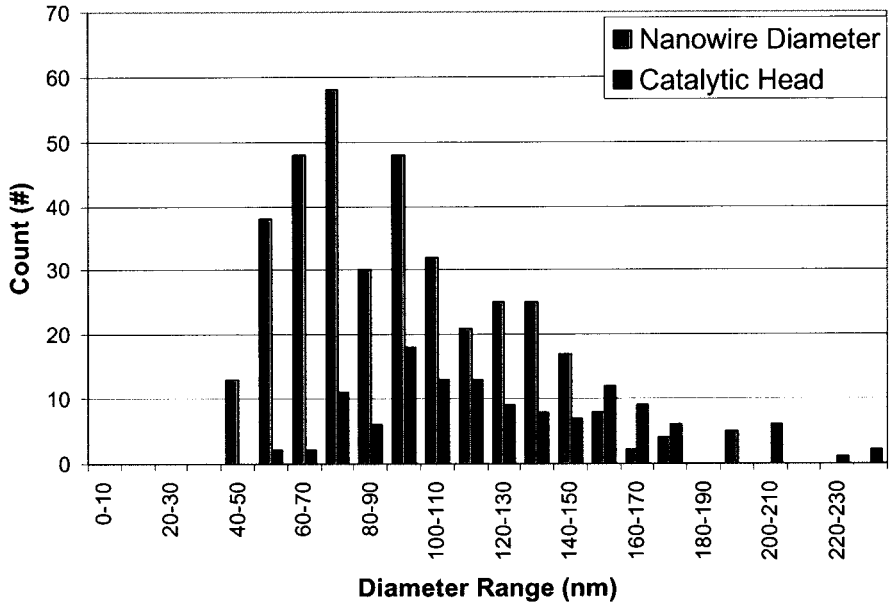

Figure 5.8. Histogram of diameter distribution.

After multiple runs have been performed, the surface of the boat obtains a white coloration and the inner surface of the quartz reaction chamber a gray coloration. Under scanning electron microscopy, the white coat of the boat is observed to consist of nanowires, as shown in Figure 5.9.a and 5.9.b. Directly above the source chamber, small crystals of either cubic or tetragonal lattice structure are found, as shown in Figure 5.9.c. This is in consistence with Huang *et al.* (2001) [9]. Near the egress of the tubular reaction chamber where the temperature gradient is -200 °C per centimeter, quasi-pin structures are formed. Figure 5.9.d and 5.9.e demonstrate well-defined facets and

spherical heads. These heads are of different morphology than those grown on the sapphire substrate using gold as catalytic material. Some of the pin heads appears to growth out of the body of the wire. It is believed that these pin-heads are composed mainly of metallic tin and tin oxide, via the self-catalytic vapor-liquid-solid mechanism. In this process, condense tin serves as the catalytic material, instead of gold, similar to the study conducted by Chen *et al.* (2003) [66].

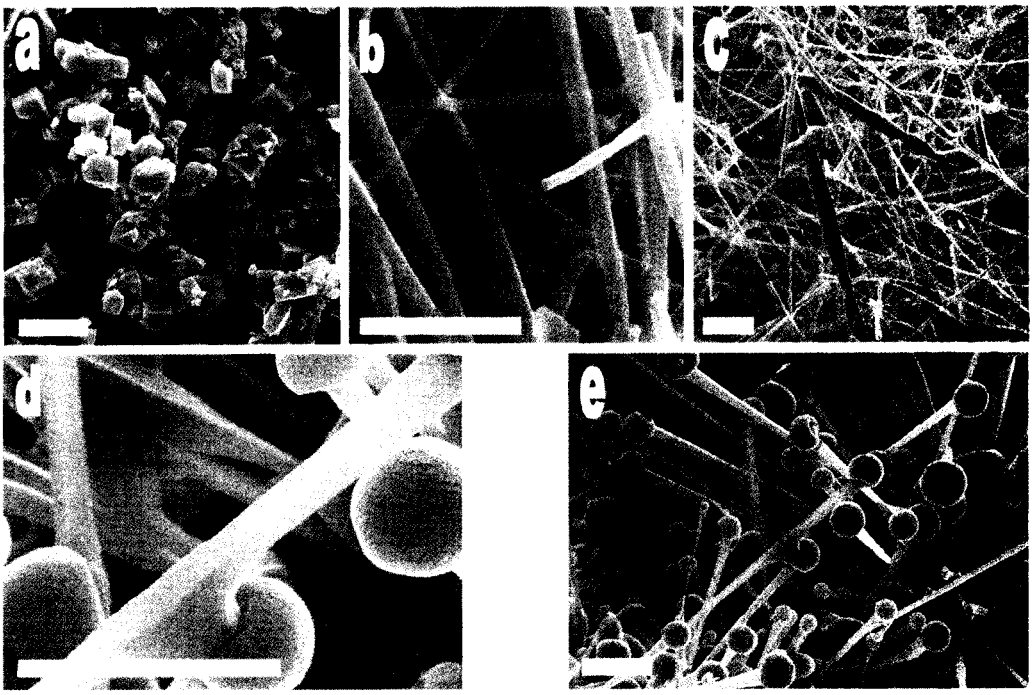

Figure 5.9. Collections at various places inside reaction chamber. (a) 1.5 cm on top of the source. (b)-(c), 2-3 in downstream of the source, top surface. (d) and (e) Near the egress of the reaction chamber. Scale bars are 2 microns

5.2.2 Growth Density

It has been a *de-facto* belief that an increase in carrier gas flow rate leads to a decrease in nanowire density. The reasons are two-fold. First, an increase in carrier gas flow rate effectively dilute the concentration of the vapor-phase reaction; thus, the amount of reactants being absorbed at the liquid alloy catalytic head, as well as the density and growth rate, is reduced. Second, the residence time of the reactants is inversely proportional to the carrier gas flow rate; consequently, faster flow equates to reduced growth.

To determine how growth phenomena depend on the flow rate, three experimental runs were performed at 500 sccm, 300 sccm, and 100 sccm of argon flow rate, all other variables were held constant. Figure 5.10 shows that in this process window 300 ± 200 sccm, higher flow rate leads to denser and faster growth. Here, at 500 sccm, the much longer length masks the underlying "fabric" morphology on the *m*-sapphire, as observed at 300 sccm. At 100 sccm, growth is sparse; indeed, an attempt at 30 sccm yielded only occasional nucleation sites. A minor waviness due to charging effect, as the samples were not coated with a conductive layer, is visible in Figure 5.10.a. It appears that higher flow rate enhances the effective carriage capacity by reducing the deposition of the vapor-phase reactants onto the surface of the quartz tube and boat *en-route* to the substrate. Interestingly, the average diameter seems to decrease with increasing flow rate, as shown in Figures 5.10.d and 5.10.f.

Another possible explanation of the observed phenomenon is the existence of gas-phase oxidation reactions. For a two-body reaction, a third non-reactive body is

frequently necessary for dissipation of the excess kinetic energy, allowing the reaction to go forward upon collision of the three members. Thus, higher pressure or higher flow rate may introduce the needed third body for the gas phase reaction to proceed to completion. Further study is recommended on this phenomenon.

The third possible explanation would be the inverse relationship between the boundary layer thickness and the "free-stream" velocity. For the slanted position, although mass transport to the surface of the substrate is predominantly by convection, there may exist both a momentum and a mass boundary layer between the "main-stream" flow and the growing front of the nanowire. Consequently, increase in carrier flow rate could lead to increased growth rate.

Another explanation rests within the kinetics of phase transformation, as discussed in Appendix B2.4. As the metal oxides crystallizes out of the alloy catalytic head, an enormous enthalpy is released, -923 kJ/mol and -577 kJ/mol for In_2O_3 and SnO_2 at standard conditions. The excess heat may force the crystalline metal oxide to undergo a phase transformation back to the liquid phase. Thus, the increase in convection may facilitate heat dissipation from the catalytic head and promote the crystallization reaction as the local substrate temperature is predicted to decrease at higher flow rate. Again, further experimental and theoretical studies are highly recommended to elucidate the dominant phenomenon.

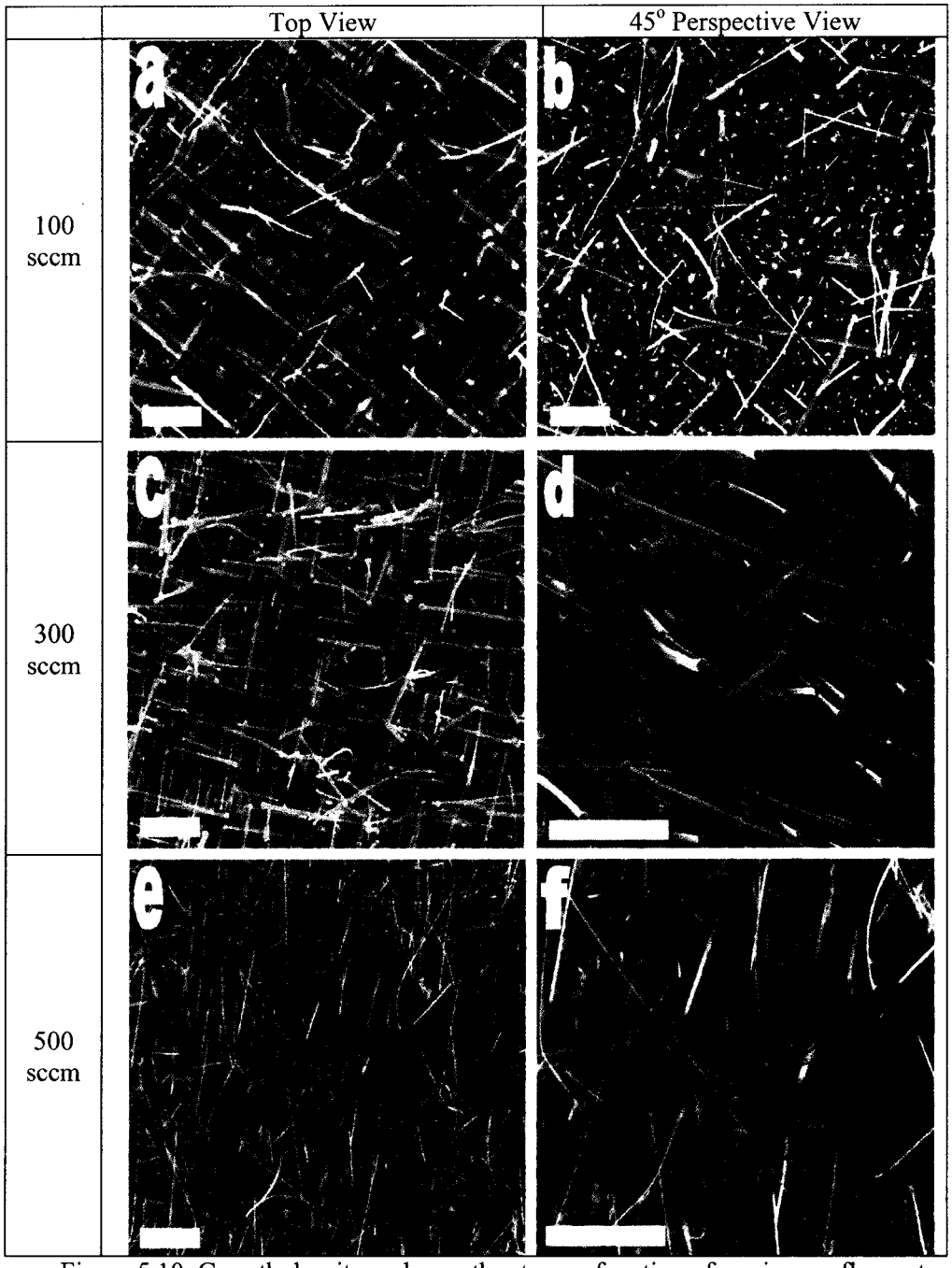

Figure 5.10. Growth density and growth rate as a function of carrier gas flow rate.

As discussed previously, there exists a process window for the temperature parameter. At the upper and lower bounds of the temperature range, growth density is sparse and length is shorter. This observation is expected as sufficient thermal energy must be required for the carbothermal reaction and evaporation of the metal species to proceed. Excessive thermal energy is found to exert inhibitory effects on nanowire synthesis, as some of the exothermic oxidation and crystallization reactions may become more reversible at elevated temperature, in accord with Le Chatelier's Principle, as discussed in Appendix B. Furthermore, the kinetic theory of gases dictates the average velocity of the gas molecule as a function of temperature; thus, at high temperature, the gaseous reactants may possess enhanced mobility and reduced reactivity.

Figure 5.11 delineates the morphology as a function of temperature on *m*-sapphire. Here, the temperature was incremented from 790 °C to 940 °C, by 30 °C per step. At 790 °C, only uniformly dispersed nucleates on a "polycrystalline" thinfilm of indium-tin oxide are observed. In contrast, at 940 °C, surface coverage of the "polycrystalline" thin film of indium-tin oxide is not as complete as at 790 °C. Evidently, lack of vapor content inhibits growth at 790 °C; whereas, excessive thermal/kinetic energy inhibits growth at 940 °C. At 910 °C, the nanowire possesses a larger base at the interface with the substrate; as the nanowire elongates, the diameter tapers. It is expected that these nanowires possess different compositions, as the reduction and oxidation reactions of the various oxides have different functional dependence on temperature.

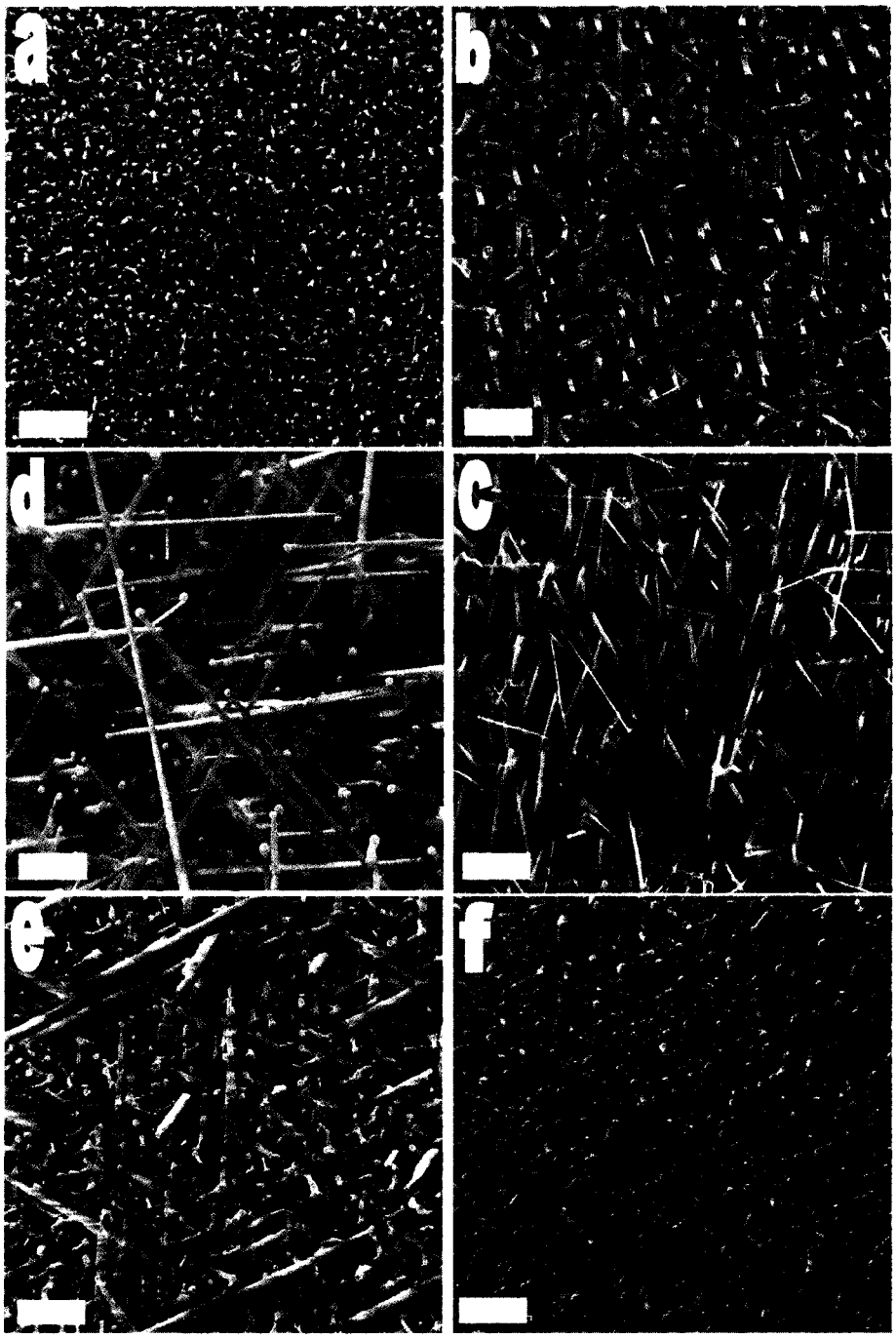

Figure 5.11. Growth morphology as a function of temperature. (a) 790 °C, (b) 810 °C, (c) 850 °C, (d) 880 °C, (e) 910 °C and (f) 950 °C. Images are viewed at 45° angle. Scale bars are 1 microns.

5.3 Transmission Electron Microscopy

5.3.1 Energy Dispersive X-ray (EDX)

EDX data reveal these well-faceted nanoparticles to consist mainly of Au:Sn:In. The EDX data were obtained using a transmission electron microscope, rather than a scanning electron microscope, to provide a more representative snapshot of the individual nanowires instead of the bulk materials. Figure 5.12 shows the EDX data of the catalytic head. Software analysis revealed that the catalytic head composition to be 71.2 atomic percent in gold, 6.2 atomic percent in indium, and 22.6 atomic percent in tin. In Figure 5.13, the atomic ratio of indium and tin is 5.4 to 94.6. Although the software analysis did not report the presence of gold in the body of the nanowire, there appears to be a miniscule gold K_β peak in Figure 5.13.

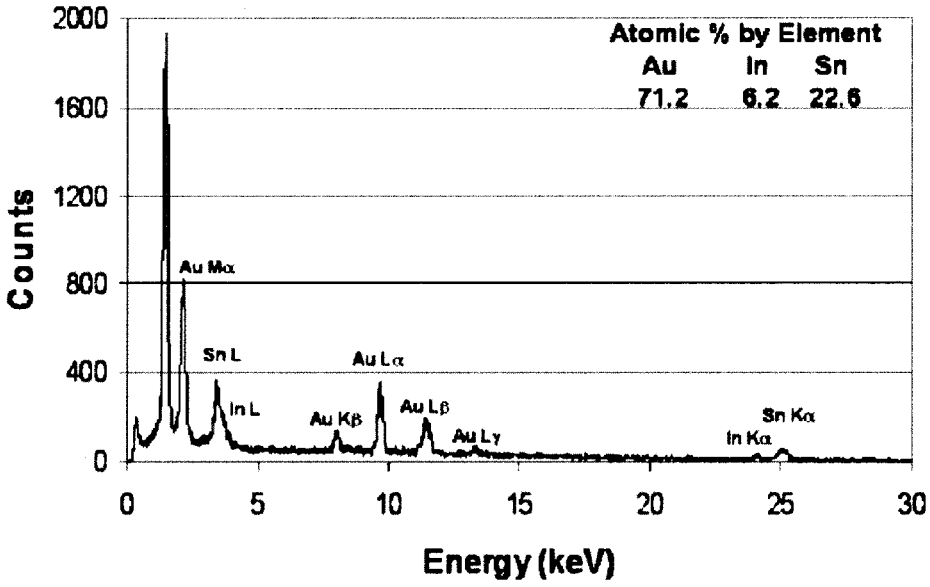

Figure 5.12.a. Composition of the catalytic head of an In-SnO_2 NW.

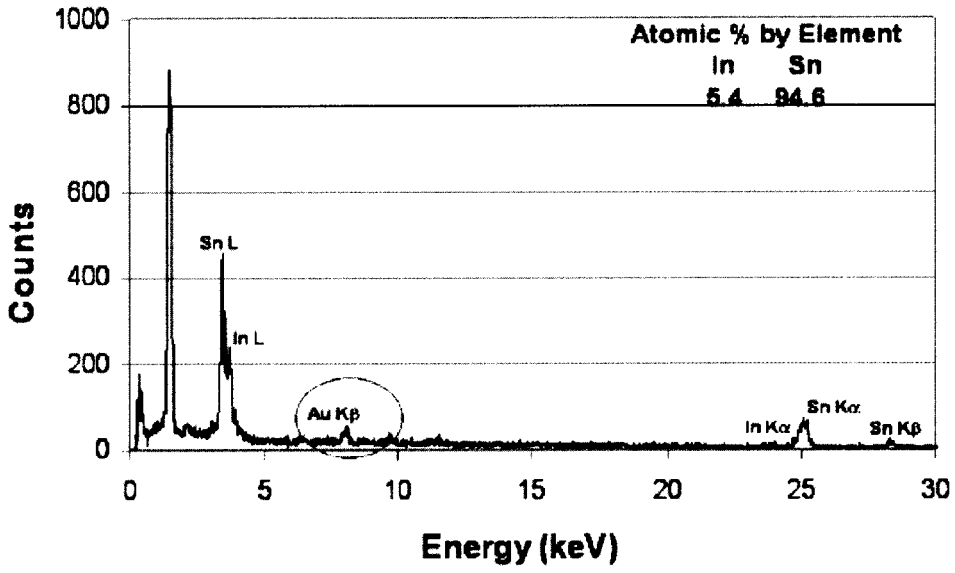

Figure 5.13. Composition of the body of an In-SnO_2 nanowire.

5.3.2 Transmission electron micrographs

Transmission Electron Microscopy (TEM) images provide further insight into the structure of In-SnO_2 nanowires. Figure 5.14.a shows a TEM bright field image of a cross-section of an In-SnO_2/*m*-sapphire interface. The nanowires are projected at angles typically ~ 45 degrees from the substrate plane and exhibit diameters between 50 – 80 nm, consistent with the earlier SEM images. Relatively long nanowires (> 10μm) could be occasionally observed. Alloyed nanoparticles are frequently found at the ends of the nanowires, as seen in Figures 5.14.a and 5.14.b, providing another evidence for the catalyst-assisted VLS growth mechanism. Although self-catalytic VLS nanowire growth via Sn catalytic particles formed through the so-called internal chemical reactions could possibly occur, the absence of catalytic nanoparticles consisting solely of tin from EDX

analysis has ruled out such a possibility. The diameter of the nanowires is highly uniform and appears rather homogenous and free of observable grain defects/boundaries, suggesting high single crystallinity of these nanowires.

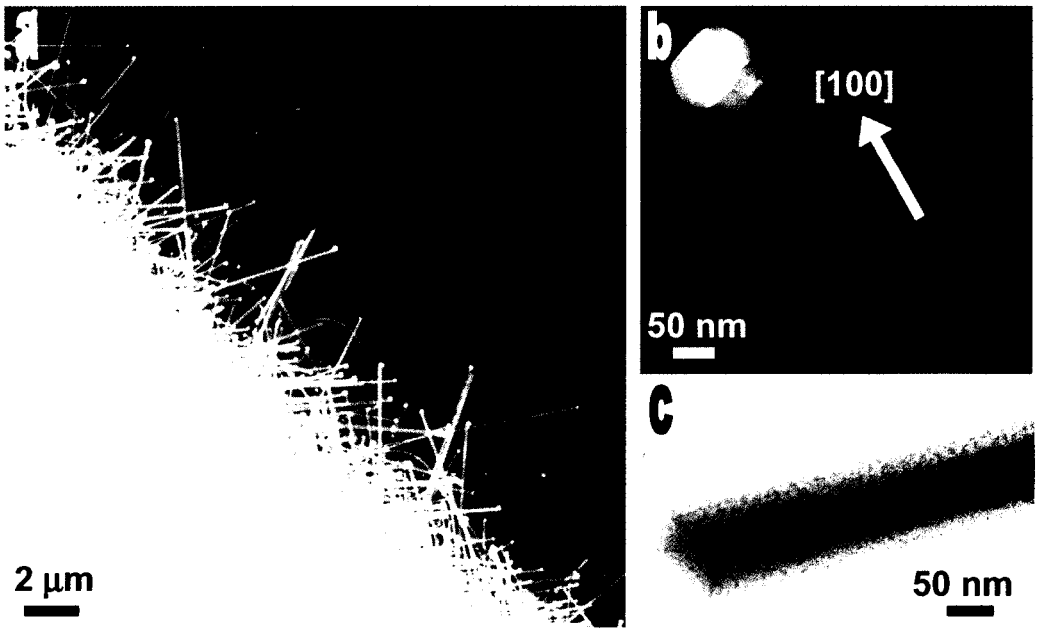

Figure 5.14. TEM micrographs of In-SnO_2 NWs on *m*-sapphire.

5.3.3 Selected area electron diffraction

A selected area electron diffraction (SAED) pattern, Figure 5.15.b, of a nanowire taken perpendicular to the nanowire axis further confirms the high single crystallinity. Regular diffraction spots could be indexed for the $[1\bar{1}\bar{1}]$ zone axis of single-crystalline tetragonal rutile SnO_2, with estimated lattice constants of a = 4.685Å and c = 3.200Å, which are close to that reported using powdered X-ray diffraction (a = 4.737Å and c = 3.186Å, JCPDS 88-0287), [56]. Table 5.2 tabulates the crystal structures of various potential compositions in the ITO system.

Table 5.2. Crystal structure of indium and tin oxides

Materials	Structure	a (Å)	c (Å)
In_2O_3 [57]	Cubic Bixbyite	10.118	
SnO_2 [58]	Tetragonal/Rutile	4.737	3.185
SnO [59]	Tetragonal	3.796	4.816
Sn_3O_4 [60]	Triclinic	4.86/5.88	8.20

A study performed by Dai *et al.* 2002 [61] suggests a phase transformation of SnO and Sn_3O_4 to SnO_2 occurring at 700 °C. Since the reaction temperature range is 800 – 900 °C, any SnO and Sn_3O_4 present in the catalytic head would most likely be oxidized by oxidizing environment or transformed to tin (IV) oxide. Comparison of the lattice parameters, along with the phase-transformation information, highly suggests that the crystal structure of the nanowire is tin (IV) oxide rather than other forms of tin oxide or indium oxide.

Apparently, the incorporation of indium atoms in the SnO_2 lattice structure does not seem to adversely affect the highly uniform crystal packing. Physical deposition of indium or In_2O_3 on the exterior of the nanowires is unlikely since well defined sharp side edges had been consistently observed under HR-TEM. Similar electron diffraction patterns had been routinely obtained over numerous In-SnO_2 nanowires and at different locations along the longitudinal axis of the nanowires. Figure 5.14.c shows a rectangular cross-section of a nanowire whereby the alloyed tip had been cleaved off. The well-defined crystal facets could be clearly seen, suggesting, again, the high crystallinity of the nanowires. A HR-TEM lattice-resolved image of a representative nanowire further reveals that the nanowires are structurally uniform and single crystalline, with an

interplanar spacing of 0.34 nm corresponding to the {110} plane of rutile crystalline SnO_2, as discussed in Ng *et al.* 2003 [56].

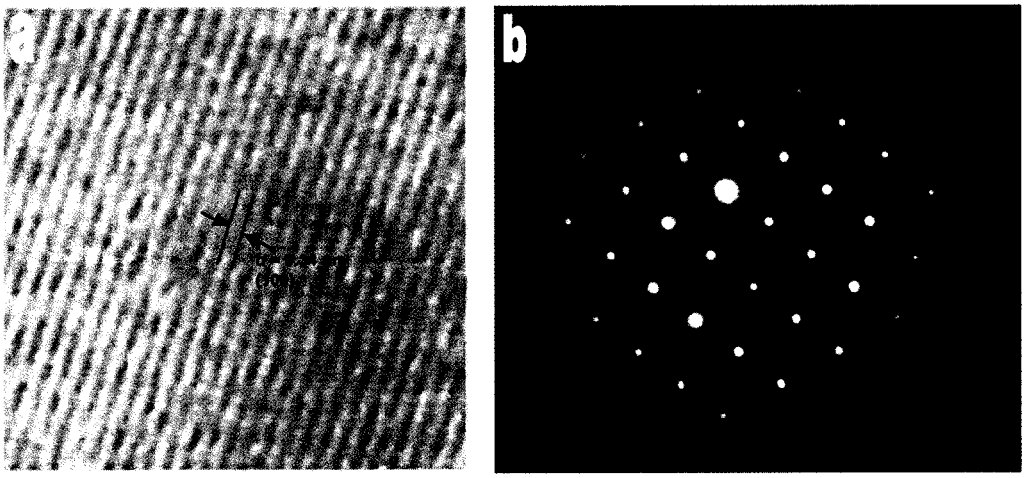

Figure 5.15. High-resolution TEM and SAED images of an In-SnO_2 NW, [56].

5.4 X-ray Photoelectron Spectroscopy

X-ray photoelectron spectroscopy (XPS) further confirms EDX analysis of the doping of indium in the SnO_2 nanowires. As shown in Figure 5.16, the atomic concentrations of the chemical elements were calculated from the peak areas; the indium concentration is approximately 5.3 atomic percent, in close agreement with the EDX result of approximately six atomic percent. Deconvolution of the peaks shows that the metal species are at fully oxidized state [56]. There are no significant impurities visible within the detection limit of the instrument and the adventitious C contamination is below five atomic percent.

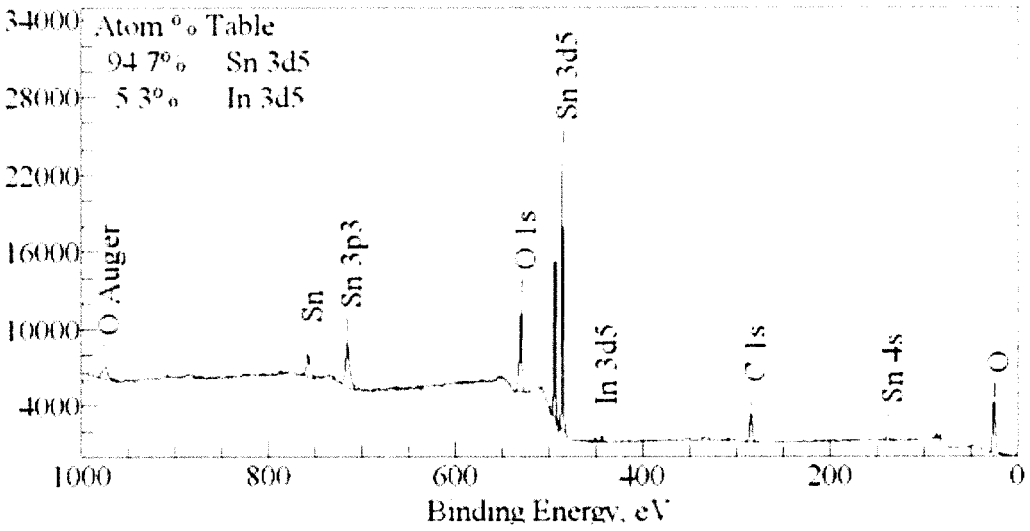

Figure 5.16. XPS spectrum of the In-SnO_2 NWs. The vertical axis is in arbitrary units.

5.5 Parametric Study

To examine the semiconductor behavior of the nanowires, the gate voltage and the bias voltage between the source and the drain are wept from -20 V to +20 V. Figure 5.17.a demonstrates the semiconductor behavior of the In-SnO_2 nanowire; the inset is the nanowire spanning two gold contact pads. However, the current is rather small, in pico-ampere range. Two plausible reasons are (1) poor contact between the nanowire and the gold pad and (2) the reduced electron mobility of the indium-doped tin oxide material.

The transistor displays"normally-on" characteristics, showing a current at zero gate voltage. As the gate voltage increases from -20 V to +20 V, the magnitude of the current between the source and the drain decreases, showing an *n*-type semiconductor behavior, consistent with the intrinsically *n*-type SnO_2. This behavior explains why there is minimal charging effect when samples, not coated with metal, are viewed under the

SEM. There appears to be saturation at gate voltages of -15 and -20 V. No I-V curve of tin oxide or indium-doped tin oxide nanowires could be found in the literature, thus far. Therefore, no comparison is possible.

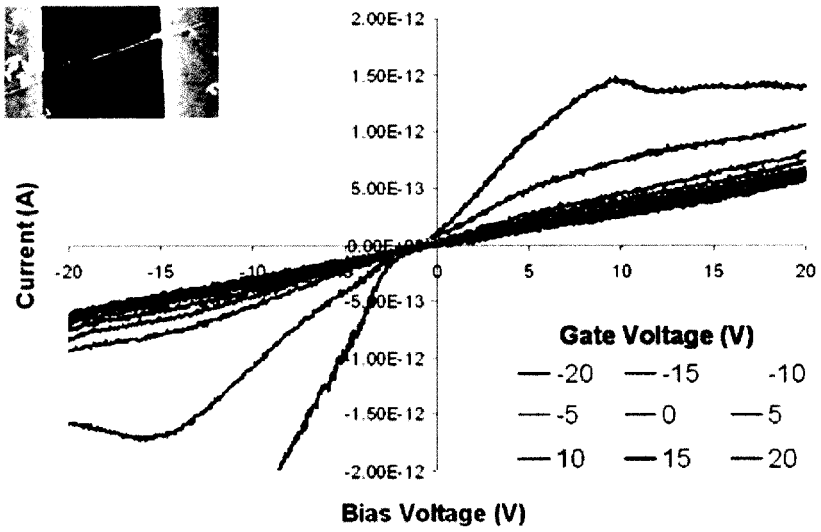

Figure 5.17. I-V curve of In-SnO_2 NW showing semiconducting property.

CHAPTER SIX – FURTHER ANALYSIS

A PRELIMINARY THERMODYNAMIC SURVEY ON THE SYNTHESIS OF INDIUM-TIN OXIDE NANOWIRE

6.1 Problem Statement

Surface composition data from energy-dispersive X-ray analysis and X-ray photoelectron spectroscopy indicate that the major metal constituent of the nanowire body is tin instead of indium. Selective area electron diffraction and high resolution transmission electron microscopy further suggest the crystal structure of the nanowire to be consistent with the tetragonal rutile structure of tin (IV) oxide instead of the cubic bixbyte structure of indium (III) oxide. Deductively, the nanowire composition is indium-doped tin oxide, rather than tin-doped indium oxide. These results contradict the plan of synthesizing tin-doped indium oxide from tin-doped indium oxide bulk source via the catalyst-assisted vapor-liquid-solid mechanism.

This is rather unexpected since the source contains ninety-weight-percent indium oxide and the partial pressure of indium vapor should be relatively higher than the partial vapor pressure of tin vapor in the system if carbothermal reduction produces metallic indium and tin in equal amount. Vapor pressure calculation is performed using the following Equation 3, with a percent error of $\leq \pm 5\%$, as stated by the CRC handbook, over the temperature range; the pressure curves are plotted in Figure 6.1. Evidently, within the feasible temperature range, $1070\ K < T < 1170\ K$, the vapor pressure of bulk indium is three orders of magnitude higher than that of bulk tin. On a side note, the vapor

pressure of gold is approximately 40 nTorr. Thus, evaporation of gold as the gold thin-film disintegrates to form the semi-liquid gold droplets is minimal, at reaction temperature.

$$\log\left(P_{vap}(atm)\right) = A + \frac{B}{T} + C\ \log T + \frac{D}{T^3}, \text{ where T is in Kelvin.} \qquad \text{Equation 4}$$

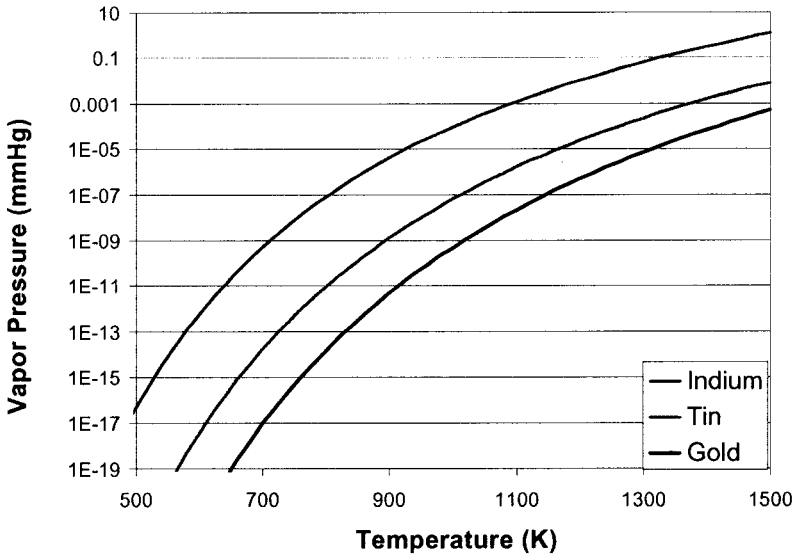

Figure 6.1. Vapor pressure of the metals as a function of temperature.

In addition, enthalpy of formation analysis, either via the Born-Haber cycle, enthalpy of formation calculation, or binding energy calculation, indicate indium (III) oxide is more stable than tin (IV) oxide. The values of lattice enthalpy of formation are tabulated in Tables 6.1 and 6.2. ΔH^{o} (TD Data) are standard enthalpies of formation, calculated using parameters from McBride *et al.* (2002) [63]. Clearly, preliminary analysis appears to indicate that indium (III) oxide should be the major constituent of the nanowire as indium is more volatile and indium (III) oxide is more stable. Details of theory and calculation in Chapter Six are provided in Appendix B.

Table 6.1. Standard enthalpy of formation for various metal oxides

Species	ΔH^{o}_{F} (Born-Haber Cycle) (kJ/mol)	ΔH^{o}_{F} (TD Data) (kJ/mol)
In_2O_3 (cr)	-783.82	-923.00
SnO_2 (cr)	-513.90	-577.63
SnO (cr)	-279.79	-280.71

Table 6.2. Theoretical lattice binding energy for the crystalline metal oxide species

Species	r_+/r_-	CN	$U_{POT\ MIN}$ (kJ/mol)	E_B (kJ/mol)
In_2O_3 (cr)	0.606	6	-14390	-43169
SnO_2 (cr)	0.561	6	-11781	-35343
SnO (cr)	0.689	6	-3688	-11063

However, the compositional analysis data contradicts the expectations. Thus, detailed thermodynamic and kinetic analyses of the process at the source, in the gas phase, and in the liquid alloy catalytic head are warranted to rationalize the results and facilitate in-depth understanding of the system. In the following sections, thermodynamic calculations are performed to deduce the mechanistic process and the reason why indium-doped tin oxide nanowires are synthesized.

6.2 Thermodynamic Analysis of Synthesis Phenomena

6.2.1 Preliminary

To deduce the mechanism of reaction, a combinatorial approach has been performed to determine which reactions are plausible under the reaction conditions. However, this method relies extensively on available thermodynamic data on measurable species and the assumption of the involved species. The existence of intermediate species is plausible but cannot be accounted for. Thus, the calculations in Appendix B provide only a superficial analysis and cannot provide a comprehensive and exclusive capture of the phenomena inside the reaction chamber.

A complete thermodynamic analysis is beyond the scope of this study, multiple simplifications are made to minimize mathematical complexity. Consequently, unity is assigned to the activities of the solids and ideal gas behaviors are attributed to the gaseous species. This assumption is reasonable as the products and reactions are of different phases and the reaction condition is at elevated temperature and atmospheric pressure. Thus, the partial pressures at the source can be obtained from the Gibbs free energy calculations.

6.2.2 Inputs to system

To accurately describe the process, the inputs must be well-defined. For the current experimental set-up, the inputs are the gold-coated sapphire substrate, source mixture of ITO and graphite powders, and argon carrier gas. Table 6.3 tabulates the composition data of the input carrier gas. Although the purity of argon is 99.999% and the concentrations of oxygen, water, and carbon dioxide are each less than one part per

million, these oxidative gases potentially contribute to the reactions inside the chamber. More importantly, the exit end of the reaction chamber was exposed to ambient air in the new set-up, providing another critical source of oxygen. A preliminary calculation, provided in Appendix C, shows that the net flux can be as high as 0.2 μmol/s.

Table 6.3. Impurity composition of argon carrier gas (www.scottgas.com).

ULTRA PURE 99.999% ARGON – IMPURITY ANALYSIS REPORT	
N_2	< 4 PPM
O_2	< 1 PPM
H_2	< 4 PPM
CO_2	< 1 PPM
THC	< 0.5 PPM
H_2O	< 1 PPM

The as-prepared composition of ITO granular is not available from Alfa Aesar, despite attempts to contact the manufacturer. Thus, the composition is rationally elucidated below. The MSDS composition of hot-pressed ITO granules is 90 wt% indium (III) oxide and 10 wt% tin (IV) oxide. Though the process details are unavailable, the preparation of ITO granular involves hot-pressing mixture of indium (III) oxide and tin (IV) oxide in 9:1 weight ratio. The MSDS from Alfa Aesar describes the ITO granules as white or yellow in color. However, the purchased ITO granules are actually in dark-gray color, similar to the color of tin (II) oxide powder. The colors of indium (III) oxide and tin (IV) oxide are yellow and light-white respectively. It appears that Alfa Aesar does not perform composition analysis of the ITO granules and it may have reported the composition of the reactants, not the products, instead.

Based on observations in Session 5.1.4, tin oxide appears not to exist as tin (IV) oxide in ITO, but rather predominantly as tin (II) oxide or an "activated" form. For emphasis, the data are re-introduced below. Some nanowire growth was observed using pulverized granular ITO mixed with alumina powder or tin (II) oxide powder at reaction temperature and flow rate; though the growth was not as profuse as with the one-to-one mixing of ITO powder or tin (II) oxide powder with graphite powder, as shown in Figure 6.2. Alumina powder was chosen to simulate the mixing effect of graphite powder. Another interesting observation was made by comparing Figure 6.2.b and 6.2.c where the alumina-ITO ratio was decreased from 1:1 to 1:2 – there appears to be less growth for the 1:2 ratio. A possible explanation is that an internal self-catalytic mechanism may occurs, which does not occur for pure SnO_2 powder. Further studies to characterize the ITO composition and the "activation effect" are recommended.

No growth was observed using either tin (IV) oxide powder or a mixture of tin (IV) oxide powder and graphite powder at standard reaction conditions, only at a significantly higher temperature. Consequently, it is reasonable to deduce that during preparation of hot-pressed ITO granules, tin (IV) oxide either decomposes to tin (II) oxide and oxygen via the following reaction, as this reaction can proceed above 300 °C according to Moreno *et al.* (1992) [64] and Nagano (1984) [65] or form some unknown volatile complexes. Although the following decomposition reaction can, reportedly, proceed at a lower temperature than stated feasible range, it was not observed in this study.

$$2\ SnO_{2\,(s)} \rightarrow 2\ SnO_{(s)} + O_{2\,(g)}$$

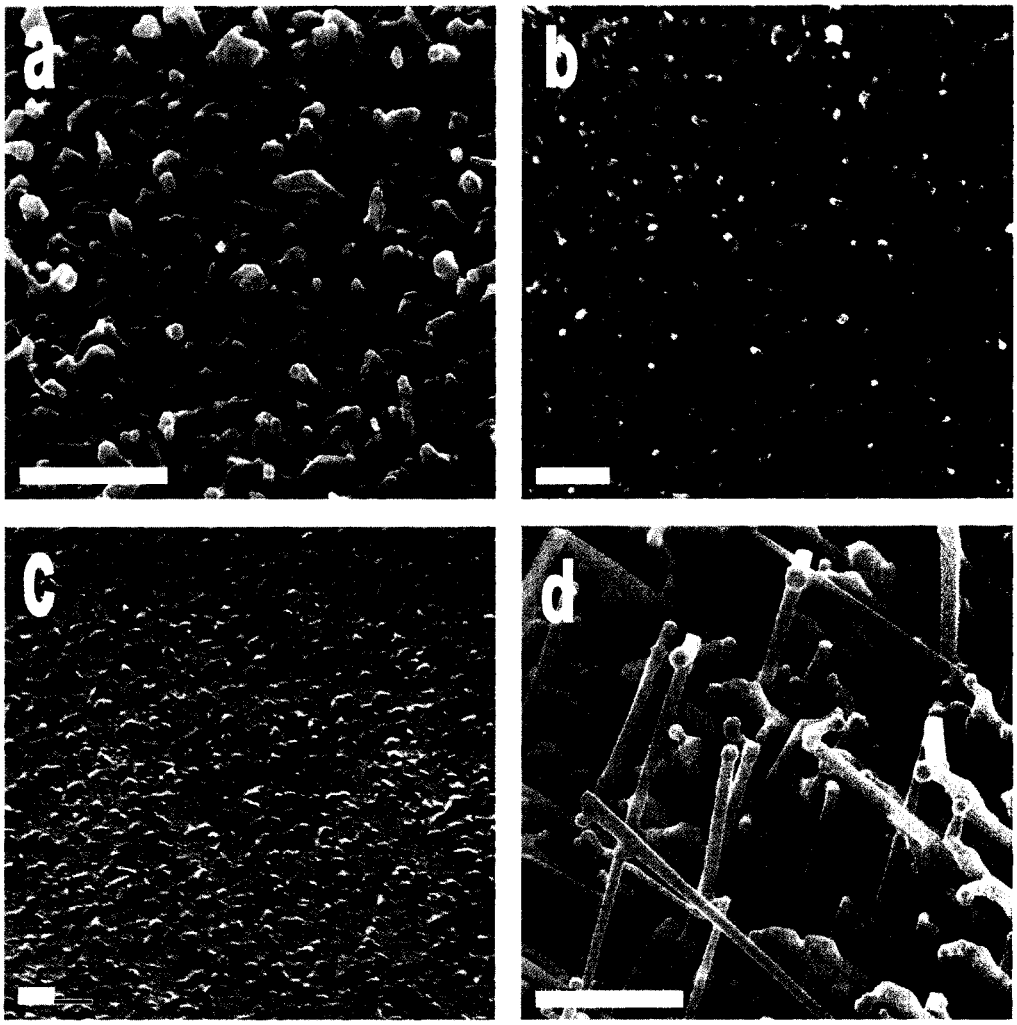

Figure 6.2. Other sources. (a) 1:1 weight ratio of SnO and In_2O_3 powders, (b) 1:1 weight ratio of ITO and 0.05μ γ-Al_2O_3 powders, (c) 2:1 weight ratio of ITO and 0.05μ γ-Al_2O_3 powders, (d) 1:1 weight ratio of SnO and graphite powders. All runs performed in new quartz tube and boat. Scale bars are 1 micron in length.

6.2.3 Nanowire composition

A combinatorial analysis was performed in Appendix B to determine which reactions are thermodynamically feasible at the reaction conditions. The species under investigation are listed in Table 6.4. If the following assumptions are quantitatively valid, then the ratio of the partial pressure of chemically generated tin-containing vapor species to the partial pressure of chemically generated indium-containing vapor species is estimated to be 148:1.

Table 6.4. List of species under thermodynamics study.

Phase	**Species**
Gas	CO, CO_2, O_2, InO, In_2O, In, SnO_2, SnO, Sn
Liquid	In, In_2O_3, SnO_2, SnO, Sn
Solid/Crystalline	In, In_2O_3, SnO_2, SnO, Sn

(1) All reactions are independent,

(2) System is in a quasi-equilibrium state,

(3) System exhibits ideal bulk solid or liquid behavior,

(4) Carbon monoxide is generated only by carbothermal reduction of tin (II) oxide and tin (IV) oxide,

(5) Local concentration of carbon monoxide is at equilibrium, and

(6) Liquid-gas phase transformation of tin and indium is constrained by the generation of the liquid metals.

Including the fact that SnO is the more thermally volatile oxide, this calculated ratio partially explains the reason why indium-doped tin oxide nanowire was synthesized from the 1:9 tin-to-indium source ratio, instead of tin-doped indium oxide nanowire. Despite

the presence of more indium oxide in ITO source, higher vapor pressure of indium, and the more negative lattice enthalpy, thermodynamics does not supply sufficient indium vapor from the simultaneous "carbothermal" reduction process of indium (III) oxide, tin (IV) oxide, and tin (II) oxide.

6.2.4 Phase diagrams and final composition of catalytic nanoparticle

Since ternary or higher-order phase diagrams are unavailable, the analysis presented below is based solely on binary phase diagrams of tin-gold and indium-gold and the assumption of the reaction sequence presented in Section 2.2.1. The feasibility zone is drawn on the two phase diagrams, Figures 6.3 and 6.4. Evidently, as the tin or indium composition increases above ten weight percent, the alloy droplet becomes liquid. The tin/indium composition range in the liquid alloy droplet is wide, theoretically. Nonetheless, it is noted that the composition of indium and tin in the alloy cannot be too high, as they will be evaporated off due to the low melting points of the metals and the increased surface area. It was experimentally demonstrated that 2 nm-thin tin film can be evaporated away at reaction temperature even though the boiling point of bulk tin is 2602 °C.

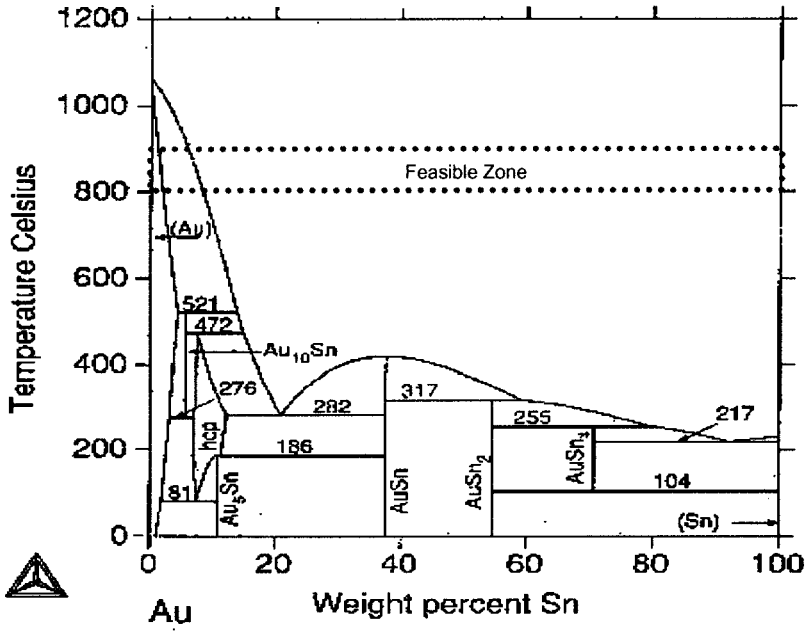

Figure 6.3. Binary phase diagram of the Au-Sn system.

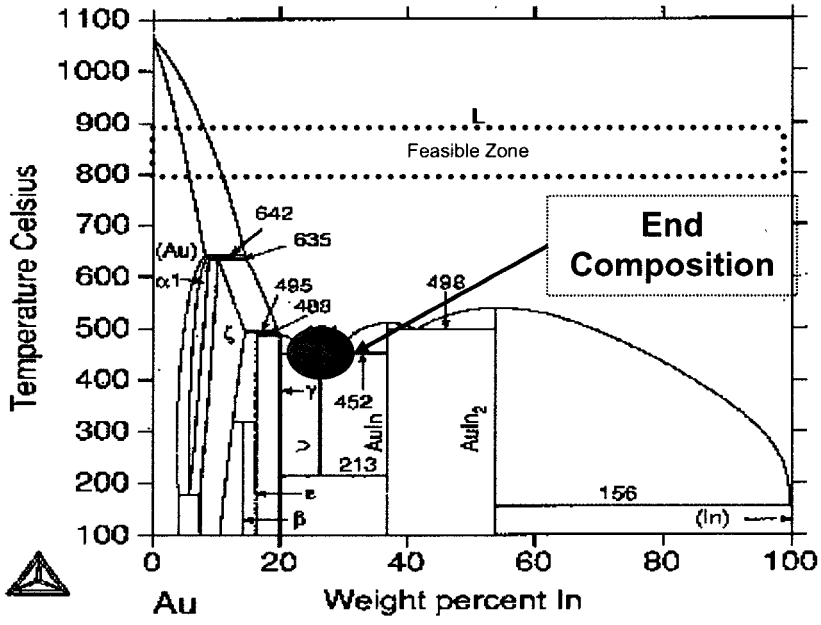

Figure 6.4. Binary phase diagram of the Au-In system.

The high concentration of indium and tin in the droplet allows their oxidation from either oxygen or carbon dioxide from the gas phase at the gas-liquid interface. As discussed previously, tin availability is much higher than indium, resulting in more tin oxide in the alloy droplet. Furthermore, tin (IV) oxide can be formed by the reverse of the aforementioned reactions, allowing more alternative pathways than the formation of indium (III) oxide. According to the vapor-liquid-solid mechanism, as the metal oxide molecules reach a critical concentration, they crystallize out of the liquid alloy at the oxide/liquid interface. Indium (III) oxide molecules are added to the tin (IV) oxide crystal lattice statistically. The lattice constraint generated by the different crystal packing of indium (III) oxide within the tin (IV) oxide structure is not expected to be detected by the high resolution TEM, as the concentration of indium is below six atomic percent. However, the lattice constraint may have resulted in the small difference in the lattice parameters of the nanowires and the lattice parameters of X-ray powder diffraction, from Table 4.2.

As the reactor is cooled down to room temperature, more tin is consumed as the alloy composition moves toward the left. The decreasing temperature facilitates crystallization of majority, if not all, of the metal oxide molecules existing in the liquid alloy. Neglecting, tin and the oxides, the first eutectic point of the system should be 450 ^{o}C, having composition of 25 - 30 weight percent indium and 70 - 75 weight percent gold, based on the indium-gold binary phase diagram. The eutectic point between tin and gold at 300 ^{o}C cannot be reached as the alloy solidifies at temperature below 450 ^{o}C.

The EDX data reveals the composition of the solid catalytic head to be approximately 71 atomic percent Au, 6 atomic percent Sn and 23 atomic percent In. Translating these values to weight percentages give 81 weight percent, 4 weight percent and 15 weight percent in Au, Sn and In, respectively. The ratio 81:19 Au:In/Sn agrees reasonably well with the calculated binary phase diagram.

6.3 Proposed reaction mechanism

As mentioned previously in Section 2.2.1, Huang *et al.* [9] suggest the following chemistry mechanism for the synthesis of ZnO nanowires:

1. Carbothermal reduction of zinc oxide by graphite to form zinc and carbon monoxide occurs at 925 °C. Zinc is evaporated into the vapor phase and is convected downstream by the inert argon gas to the catalyst particle.

2. Vapor zinc is absorbed into the gold, forming a liquid alloy droplet due to the melting point depression in the *alloying* step of the VLS mechanism.

3. Zinc at the surface of the liquid alloy droplet is oxidized by the carbon monoxide in the gas phase to form zinc oxide.

4. Disproportionation to form liquid gold-zinc oxide alloy droplet and crystalline zinc oxide *nucleate*. Crystalline nanowire results due to migration of zinc oxide molecules to the lower energy site at the zinc oxide-gold interface and *elongation* of the wire. Here, an internal circulation loop within the liquid alloy droplet delivers zinc oxide to the nucleating interface and replenishes depleted zinc at the surface.

Due to the observations that (1) crystallites formed on the inner surface of the reaction chamber directly on top of the source, (2) nanowires formed both on the surface of the boat and the inner surface of the chamber downstream of the source, where it was experimentally confirmed that a 2 nm tin thinfilm was completely evaporated under reaction conditions, (3) increase in flow rate leads to increase in growth rate, and (4) both indium oxide and tin oxide possess highly negative enthalpy and Gibbs free energy of formation, it is believed that, to some certain extent, there is metal oxide aerosol species both due to the evaporation of the metal oxide solid source and gas-phase oxidation of the metal vapor. The metal oxide vapors are incorporated directly into the alloy heads. These metal oxide vapors may also aggregate in the gas phase and condense later to initiate growth themselves by VS mechanism.

A suggested mechanism based on the thermodynamic analysis in Appendix B is outlined below.

- Source:
  - Physical evaporation of oxides.
  - Carbothermal reduction of SnO. As CO percolates up the powder matrix, it is further oxidized to CO_2 by indium oxide and tin oxide. The volatile indium (I/II) oxide, In, and Sn are quickly evaporated at high temperature.
- Gas-Phase:
  - The metal-containing species are convected downstream.
  - Some gas-phase oxidation reactions proceed simultaneously.

– The inner surface of the chamber may serve as a "catalytic surface" and inert argon may serve as the energy-dissipation entity for the gas-phase reaction.

- Catalytic head:

– Alloying of metal oxide and metal vapors into gold droplets.

– Oxidation of metal by O_2 and CO_2 at the gas-liquid interface.

– Heteroepitaxial nucleation, followed by 1-D elongation, proceeds to form nanowires.

CHAPTER SEVEN - CONCLUSIONS

7.1 Conclusions

Successful synthesis of indium-tin oxide nanowires was achieved for a wide range of growth conditions. Despite this wide range of operating condition, good uniformity and density were achieved at a narrower range of temperature and carrier gas flow rate. Particularly, high-quality single crystalline nanowires were predominantly obtained within a relatively narrow temperature range of 840 – 860 °C, a carrier gas flow rate of 250 – 350 sccm, a feedstock source/substrate distance of separation of 1 – 3 cm, and a gold thin film thickness range of 1 – 2 nanometers.

The average diameter of the nanowires is 94 nanometers with a standard deviation of 19 nanometers, whereas, the average diameter of the nanoparticles are 125 nanometers with a standard deviation of 32 nanometers. As demonstrated experimentally, the diameter of the nanowires can be controlled by the thickness of the gold thinfilm. Another possible method is hydrogen reduction at elevated temperature.

In this process window of 300 ± 200 sccm, higher argon flow rate leads to denser and faster growth. No growth was observed outside of the temperature window of 790 °C – 940 °C. At 790 °C, only uniformly dispersed nucleates on a "polycrystalline" thin film of indium-tin oxide were observed. In contrast, at 940 °C, surface coverage of the "polycrystalline" thin film of indium-tin oxide is not as complete as at 790 °C. The data

suggest the lack of vapor content, i.e. mass transfer, inhibit growth at 790 °C; whereas, excessive thermal energy, i.e. kinetic constraints, inhibit growth at 940 °C.

EDX software analysis reveals the composition of the catalytic head to be 71.2 atomic percent in gold, 6.2 atomic percent in indium, and 22.6 atomic percent in tin. In the body of the nanowire, the atomic percent ratio of indium and tin is 5.4 to 94.6. This value agrees well with the XPS analysis, where the ratio of tin to indium is approximately 20:1. Although the software analysis does not report the presence of gold in the body of the nanowire, there appears to be a miniscule gold K_β peak, which could be attributed to gold from the background or gold from the body of the nanowire.

A selected area electron diffraction (SAED) pattern of a nanowire taken perpendicular to the nanowire axis further confirms the high single crystallinity. Regular diffraction spots could be indexed for the $[1\bar{1}\bar{1}]$ zone axis of single-crystalline tetragonal rutile SnO_2, with estimated lattice constants of a = 4.685Å and c = 3.200Å.

The possible explanations why indium-doped tin oxide nanowire was synthesized instead of tin-doped indium oxide nanowire were traced back to the composition of the indium-tin-oxide source and thermodynamics. The composition of the source is postulated to be mainly indium (III) oxide and tin (II) oxide or "activated" ITO. Due to the higher volatility of tin (II) oxide, more tin-containing vapor species are generated at the reaction conditions instead of indium (III) oxide, resulting in the predominantly tin (IV) oxide composition, as the other tin oxides transform to tin (IV) oxide.

Parametric study demonstrates the semiconducting properties of the tin oxide nanowires. Due to the lack of a photoluminescence system, the photoluminescence property of the doped nanowire is not conducted here to determine the quantum confinement and doping effects on photoluminescence.

7.2 Recommendations for Further Studies

Based on the current study, the following studies are recommended:

1. In-depth study of the gas phase and liquid phase reactions to determine precisely how thermodynamics control the dopant concentration and crystallinity of the nanowires, either by *in-situ* mass spectroscopy/chromatography or by computer simulation.

2. Reduction of the as-grown nanowires to reduce and control diameters using hydrogen gas at elevated temperature.

3. Synthesis of nanowires at fixed temperature and varied mix ratio of tin (II) oxide and indium (III) oxide

4. Synthesis of nanowires at various temperatures, within the 790 – 950 ^{o}C window, using either SnO-In_2O_3 or SnO_2-In_2O_3 source combinations.

5. Synthesis of nanowires using SnO_2 and In_2O_3 powders mixed with graphite as source, instead of ITO powder mixed with graphite powder.

6. Study other catalyst materials.

7. Study band-gap energy and photoluminescence variations based on (3) and (4).

8. Better reactor design where flow dynamics is considered to minimized the mass-transport limitation.

9. Study electron transport phenomena inside the doped nanowires.

10. Investigation of potential applications in nano-electronics and nano-photonics.

REFERENCES

1. Drexler, K. E., "*Engines of Creation – The Coming Era of Nanotechnology*," Anchor Books, 1986. (ISBN 0-385-19973-2).

2. R. Feynman, "*There's Plenty of Room at the Bottom*," Caltech's Engineering and Science, Feb. 1960.

3. S. Iijima, "*Helical Microtubules of Graphitic Carbon*," Nature **354**, 56-58, (1991).

4. P. G. Collins and Ph. Avouris, "*Nanotubes for Electronics*," Scientific American, 62-69 (Dec 2000). J.A. Misewich, R. Martel, Ph. Avouris, J.C. Tsang, S. Heinze and J. Tersoff, "*Induced Optical Emission from a Carbon Nanotube FET*," Science, **15**, (2003). www.ibm.com/research.

5. P. L. McEuen, M. Fuhrer, and H. Park, "*Single-Walled Carbon Nanotube Electronics*", To be published in the inaugural issue of IEEE Transactions on Nanotechnology (2002).

6. www.siliconstrategies.com or respective company websites.

7. Y. Benenson, T. Paz-Elizur, R. Adar, E. Keinan, Z. Livneh and E. Shapiro, "*Programmable and autonomous computing machine made of biomolecules*," Nature, **414**, 430 - 434 (2001).

8. M. Meyyappan, T.R. Govindan and H. Partridge, "*Nanotechnology Research at NASA Ames*," NASA Ames Research Center Publications, (2001).

9. M.H. Huang, Y. Wu, H. Feick, N. Tran, E. Weber and P. Yang, "*Catalytic growth of zinc oxide nanowires through vapor transport*," Adv. Mater. **12**, 113 (2001).

10. P. Yang, "Miniaturised Ultraviolet Lasers," *Global Photonics Applications and Technology*, World Markets Series, Business Briefing, 42-47 (2002).

11. X. Duan, Y. Huang, Y. Cui, J. Wang and C.M. Lieber, "*Indium phosphide nanowires as building blocks for nanoscale electronic and optoelectronic devices,*" Nature, **409**, 66 (2001).

12. Y. Hoang, X. Duan, Y. Cui and C.M. Lieber, "*Gallium Nitride Nanowire Nanodevices,*" NanoLetters, **2**, 101 (2002).

13. Y. Cui and C.M. Lieber, "*Functional Nanoscale Electronic Devices Assembled Using Silicon Nanowire Building Blocks*," Science, **291**, 851 (2001).

14. R. Chau, J. Kavalieros, B. Doyle, A. Murthy, N. Paulsen, D. Lionberger, D. Barlage, R. Arghavani, B. Roberds and M. Dovzy, "*A 50nm Depleted-Substrate CMOS Transistor (DST)*," IEEE, (2001).

15. Y. Wu and P. Yang, "*Germanium nanowire growth via simple vapor transport*," Chem. Mater. **12**, 605 (2000).

16. G. Gu, M. Burghard, G.T. Kim, G.S. Dusberg, P.W. Chiu, V. Krstic and S. Roth, "*Growth and Electrical Transport of Germanium Nanowires*," J. of Applied Physics **90** (11), 5747 (2001).

17. Y. Cui, L.J. Lauhon, M.S. Gudiksen, J. Wang and C.M. Lieber, "*Diameter-controlled synthesis of single crystal silicon nanowires*," Appl. Phys. Lett. **78**, 2214 (2001).

18. Z.G. Bai, D.P. Yu, H.Z. Zhang, Y. Ding, Y.P. Wang, X.Z. Wang, X.Z. Gai, Q.L. Hang, G.C. Xiong and S.Q. Feng, "*Nano-scale GeO_2 Wires Synthesized by Physical Evaporation*," Chem. Phys. Lett. **303**, 311-314 (1999).

19. C.C. Chen and C.C. Yeh, "*Large-Scale Catalytic Synthesis of Crystalline Gallium Nitride Nanowires*," Adv. Mater. **12**, 738 (2000).

20. W.S Shi, Y.F. Zheng, N. Wang, C.S. Lee, and S.T. Lee, "*Microstructures of gallium nitride nanowires synthesized by oxide-assisted method*," Chem. Phys. Lett **345**, 377-380 (2001).

21. X.P. Peng, Y.W. Wang, J. Zhang, X.F. Wang, L.X. Zhao, G.W. Meng and L.D. Zhang, "*Large-scale synthesis of In_2O_3 nanowires*," Appl. Phys A **74**, 437-439 (2002).

22. Z.W. Pan, Z.R. Dai and Z.L. Wang, "*Nanobelts of Semiconducting Oxides*," Science **291**, 1947-1949 (2001).

23. Z.R. Dai, J.L. Gole, J.D. Stout and Z.L. Wang, "*Tin Oxide Nanowires, Nanoribbons, and Nanotubes*," J. Phys. Chem. B **106**, 1274-1279 (2002).

24. H.L. Hartnagel, A.L. Dawar, A.K. Jain, and C. Jagadish, Semiconducting Transparent Thin Films, Institute of Physics, Bristol, 1995.

25. N.D. Young, R.M. Bunn, R.W. Wilks, D.J. McCulloch, S.C. Deane, M.J. Edwards, G. Harkin and A.D. Pearson, J. Soc. Inf. Displ. **5** (3), 275 (1997).

26. H. Kim, A. Pique, J.S. Horwitz, H. Mattoussi, H. Murata, Z.H. Kafafi, and D.B. Chrisey, "*Indium Tin Oxide Thin Films for Organic Light-Emitting Devices*," Appl. Phys. Lett. **74**, 3444 (1999).

27. H. Kim, J.S. Horwitz, G.P. Kushto, Z.H. Kafafi, and D.B. Chrisey, "*Indium Tin Oxide Thin Films Grown on Flexible Plastic Substrates by Pulsed-Laser Deposition for Organic Light-Emitting Diodes*," Appl. Phys. Lett. **79**,284 (2001).

28. L. Gupta, A. Mansingh and P. K. Srivastava, "Band Gap Narrowing and the Band Structure of Tin Doped Indium Oxide Films", *Thin Solid Films* **176**, 33 (1989).

29. W.I. Park, G.C. Yi, M. Kim and S.J. Pennycook, "*Quantum Confinement Observed in ZnO/ZnMgO Nanorod Heterostructure*," Advanced Materials, **15(6)**, 526 (2003).

30. C. Delerue, G. Allan and M. Lannoo, Journal of Luminescence **80,** 65-73 (1998).

31. D. Li, "*Thermal Transport Measurements of Nanotubes, Nanowires, and Nanobelts.*" 2002.

32. T. Guo, P. Nikolaev, A. Thess, D. T. Colbert and R. E. Smalley, "*Catalytic Growth of Single-Walled Nanotubes by Laser Vaporization*," Chem. Phys. Lett. **243**, 49 (1995).

33. X. Duan and C.M. Lieber, "*Laser-Assisted Catalytic Growth of Single Crystal GaN Nanowires*," J. Am. Chem. Soc. **122**, 188 (2000).

34. A.M. Morales and C.M. Lieber, "*A Laser Ablation Method for the Synthesis of Crystalline Semiconductor Nanowires*," Science **279**, 208 (1998).

35. Y.F. Zhang, Y.H. Tang, X.F. Duan, Y. Zhang, C.D. Lee, N. Wang, I. Bello and S.T. Lee, "*Yttrium-Barium-Copper-Oxygen Nanorods Synthesized by Laser Ablation*," Chem. Phys. Lett. **323**, 180-184 (2000).

36. D.P, Yu, Z.G. Bai, Y. Ding, Q.L. Hang, H.Z. Zhang, Y.H. Zou, J.J. Zou, W. Qian, H.T. Zhou, G.C. Xiong and S.Q. Feng, "*Nanoscale Silicon Wires Synthesized Using Simple Physical Evaporation*," Appl. Phys. Lett. **73**, 3076 (1998).

37. T. Muller, K.H. Heinig and B. Schmidt, "*Formation of Ge Nanowires in Oxidized Silicon V-Grooves by Ion Beam Synthesis*," Nuclear Instruments and Methods in Physics Research B **175-177**, 468-473 (2001).

38. J.D. Holmes, K.P. Johnston, R.C. Doty and B.A. Korgel, "*Control of Thickness and Orientation of Solution-Grown Silicon Nanowires*," Science **287**, 1471-1473 (2000).

39. S. Jin, Q. Li and C.S. Lee, "*Direct Growth of Amorphous Silicon Oxide Nanowires and Crystalline Silicon Nanowires from Silicon Wafer*," Phys. Stat. Sol. (a) **188** (2), R1-R2 (2001).

40. X. Duan and C.M Lieber, "*General Synthesis of Compound Semiconductor Nanowires*," Adv. Mater. **12**, 298 (2000).

41. Y. Chen, D.A. Ohlberg and R.S. Williams, "*Epitaxial Growth of Erbium Silicide Nanowires on Silicon (001)*," Matl. Sci. & Engr. B **27**, 222-226 (2001).

42. Y. Chen, D.A. Ohlberg, G. Medeiros-Ribeiro, Y.A. Chang and R.S. Williams, "*Self-Assembled Growth of Epitaxial Erbium Disilicide nanowires on Silicon (001)*," Appl. Phys. Lett. **76** (26), 4004 (2000).

43. N. Wang, Y.H. Tang, Y.F. Zhang, C.S. Lee and S.T. Lee, "*Nucleation and growth of Si nanowires from silicon oxide*," Phys. Rev. B **58**(24), 24-26(1998).

44. N. Wang, Y.H. Tang, Y.F. Zhang, C.S. Lee, I. Bello and S.T. Lee, "*Si Nanowires Grown from Silicon Oxide*," Chem. Phys. Lett. **299**, 237-242 (1999).

45. S.T. Lee, N. Wang and C.S. Lee, "*Semiconductor Nanowires: Synthesis, Structure and Properties*," Mat. Sci. & Engr. **B86**, 16-23 (2000).

46. Y.F. Zhang, Y.H. Tang, C. Lam, N. Wang, C.S. Lee, I. Bello and S.T. Lee, "*Bulk-quantity Si nanowires synthesized by SiO sublimation*," J. Cryst. Growth **212**, 115-118 (2000).

47. W.S Shi, Y.F. Zheng, N. Wang, C.S. Lee, and S.T. Lee, "*Oxide-assisted growth and optical characterization of gallium-arsenide nanowires*," App. Phys. Lett **78**(21), 3304-3306 (2001).

48. W.S Shi, Y.F. Zheng, N. Wang, C.S. Lee, and S.T. Lee, "*Microstructures of gallium nitride nanowires synthesized by oxide-assisted method*," Chem. Phys. Lett **345**, 377-380 (2001).

49. R.S. Wagner and W.C. Ellis, Appl. Phys. Lett. **4**, 89 (1964).

50. R.S. Wagner, in: *Whisker Technology*, edited by A.P. Leitt, (Wiley-Interscience, New York, 1970), p. 47.

51. Y. Wu and P. Yang, "*Direct Observation of Vapor-Liquid-Solid Nanowire Growth*," J. Am. Chem. Soc. **123**, 3165 (2001).

52. Y. Wu and P. Yang, "*Germanium nanowire growth via simple vapor transport*", Chem. Mater. **12**, 605 (2000).

53. M.S. Gudiksen, J. Wang and C.M. Lieber, "*Synthetic Control of the Diameter and Length of Single Crystal Semiconductor Nanowires*," J. Phys. Chem. B **105**, 4062-4064 (2001).

54. C.C. Chen, C.C. Yeh, C.H. Chen, M.Y. Yu, H.L Liu, J.J. Wu, K.H. Chen, L.C. Chen, J.Y. Peng and Y.F. Chen, "*Catalytic Growth and Characterization of Gallium Nitride Nanowires*," J. Am. Chem. Soc. **123**, 2791-2798 (2001).

55. Y. Wu, H. Yang, M. Huang, B. Messer, J.H. Song and P. Yang, "*Inorganic Semiconductor Nanowires: Rational Growth, Assembly, and Novel Properties*," Chem. Eur. J. **8** (6), 1260-1269 (2002).

56. P. Nguyen, H.T. Ng, J. Kong, A.M. Cassell, R. Quinn, J. Li, J. Han, M. McNeil and M. Meyyappan, "*Epitaxial Directional Growth of Single Crystalline In-situ Indium-Doped Tin Oxide Nanowire Arrays*," Nano Letters, **3** (7), 925-928 (2003).

57. JCPDS File No. 06-0416.

58. R.W.G. Wyckoff, Crystal Structures, Interscience, New York, 1968. W.H. Baur, Acta Crystallography, **9**, 515-520 (1956).

59. W.J. Moore and L.J. Pauling, *J. Am. Chem. Soc.*, **63**, 1392-1394 (1941).

60. F. Lawson, *Nature*, **215**, 955-956 (1967).

61. Z.R. Dai, Z.W. Pan and Z.L. Wang, "*Growth and Structure Evolution of Novel Tin Oxide Diskettes*," J. Am. Chem.Soc., **124**, 8673-8680 (2002).

62. CRC Handbook of Chemistry and Physics, 82th Ed, D.R. Lite, Editor, CRC Press, 2001-2002.

63. B.J. McBride, M.J. Zehe and S. Gordon, *NASA Glen Coefficients for Calculating Thermodynamic Properties of Individual Species*, NASA Glen Research Center, Cleveland, Ohio, 2002.

64. M.S. Moreno, R.C. Mercader and A.G. Bibiloni, J. Phys. Condens. Matter., **4**, 351 (1992).

65. M. Nagano, J. Cryst. Growth **66**, 377 (1984).

66. Y. Chen, X. Cui, K. Zhang, D. Pan, S. Zhang, B. Wang and J.G. Hou, "*Bulk-quantity synthesis and self-catalytic VLS growth of SnO_2 nanowires by low-temperature evaporation*," Chem. Phys. Lett. **369**, 16-20 (2003).

67. Internal unpublished data.

APPENDIX A

OTHER VAPOR-TRANSPORT MECHANISMS

A.1 Vapor-Solid Model

Physical vapor deposition, or the Vapor-Solid (VS) mechanism, is simply the evaporation of the source and condensation of the vapor-phase source material on the surface of a substrate. The essential difference between the VS mechanism and the VLS mechanism is the use of a catalytic material in the VLS growth. Here, VS denotes the phase change from vapor to solid; whereas, VLS represents the transformation from vapor to liquid alloy to crystalline solid. Importantly, it can be inferred from liquid-phase nucleation of a supersaturated solution that growth of one-dimensional structure via the VS mechanism initiates at surface defect locations on the surface of the substrate. Thus, localization control is a challenge for this mechanism.

In 1999, Bai *et al.* [18] report the growth of germanium di-oxide nanowires via the physical vapor deposition process. In this experiment, the authors attempt to grow crystalline germanium nanowires via the VLS mechanism with iron as the catalyst material. However, germanium oxide nanowires are synthesized instead. Here, a hot-pressed plate of 92 wt% high purity germanium powder and 8 wt% iron powder is maintained at 820 ^{o}C under constant argon flow rate of 130 sccm. White fluffy product is found on the quartz substrate downstream of the hot plate. TEM images show slightly curved wires having diameter range of 10 – 80 nm and length range of several to tens of micrometers. Figure A.1 shows that there are no nanoparticles at the tips of the

nanowires and EDX analysis finds no trace of elemental iron in the product even though iron powder is present in the source. An alloy nanoparticle at the tip is commonly accepted as the evidence of VLS growth.

Bai *et al.* [18] conclude the growth process is the VS mechanism. They believe that the gas phase is saturated with germanium vapor molecules, allowing prolonged growth of the nanowires. The authors claim that the oxygen is "most probably from the remaining of the vacuum system."

Figure A.1. GeO_2 nanowires via the VS growth process. Solid black arrows point to tips having no alloy nanoparticles [18].

Importantly, Bai *et al.* [18] demonstrate that VS growth can proceed even when VLS growth is intended. And deductive reasoning points to a certain range of process conditions where both VS and VLS coexist and compete with each other. Perhaps, the reaction temperature is not high enough for thermal evaporation of iron, in this case.

A.2 Oxide-Assisted Model

A.2.1 Evidence from Physical Vapor Deposition

In 1998, another model is proposed by a group of researchers from the University of Hong Kong. While attempting to grow silicon nanowires by physical vapor deposition, Wang *et al.* [43-44] discover some interesting phenomena. In this growth method, a 3:7 weight ratio mixture of solid high-purity silicon powder and silicon dioxide (Goodfellow, 99.99%) is subjected to thermal evaporation at 1200 °C for twelve hours in a quartz tube. Downstream of the source where the temperature is 970 °C, a molybdenum grid is placed to collect the silicon nanowires. The grid is directly observed under a Philips CM200FEG transmission electron microscope.

The as-grown silicon nanowires have uniform diameters, smooth surfaces, and lengths greater than 10 microns. TEM inspection detects the presence of silicon nanoparticles within the body in the form of a chain. During the nucleation phase, no metal catalyst or impurity is detected in the tips of the nanowires as in the case of VLS growth. The nucleus comprises of only a "crystalline" silicon core, with high defect density, and an amorphous silicon oxide outer layer, as detected by EDS, as shown in Figure A.2.a. The silicon oxide shell thickness depends on the diameter of the wire. Some wires grow faster because of their preferred growth orientation is normal to the surface of the substrate. Also, the vapor-phase material consists of mainly SiO. Figure A.2.b shows HRTEM image of nanoparticle (1-3) chain in the body of the silicon wire; again, no metal catalyst particle is visible inside the tip of this wire.

Figure A.2.a. TEM image of silicon nanowires by Oxide-Assisted method [44].

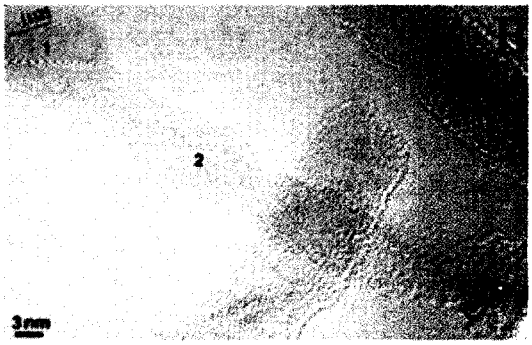

Figure A.2b. HRTEM showing nanoparticle (1-3) chain in the body of the wire [44].

Based on these observations, an oxide-assisted growth mechanism (OAM) is proposed as followed.

$Si_xO \rightarrow Si_{x-1} + SiO$ $(x > 1)$

and $2SiO \rightarrow Si + SiO_2$.

Here, the Si_xO shell on the nanowire tip acts as a catalyst. During growth, the SiO_2 shell retards the sideway growth and structural defects, such as stacking faults and micro-twins, enhance elongation of the wire. Among the surfaces in a silicon crystallographic unit structure, the (111) surface has the lowest surface energy and it promotes wire growth in the <112> direction. Other metrology tools indicate the presence of silicon oxide nanoclusters inside the nanowires as well. Raman study shows asymmetric peak at 521 cm^{-1}. Asymmetry is caused by the nano-scale size of the silicon nanoparticles, the structural defects, and the presence of the silicon mono-oxide shell.

A.2.2 More Evidences from Laser Ablation

In 2000, Lee *et al.* [45] present more evidence for the proposed Oxide-Assisted model. In this study, the solid target is a high-purity silicon powder mixed with various metals, such as Fe, Ni or Co. An excimer laser is utilized to ablate the target in a quartz tube furnace circulated with argon gas. The temperature around the target is maintained between 1200 - 1400 °C and that around the substrate is 900 - 1100 °C.

Figure A.3 shows that the wires, thus produced, are extremely long and highly curvaceous. Each wire consists of a crystalline silicon core and an outer silicon oxide sheath. Typical diameter is approximately 20 nm. High density of stacking faults and micro-twins is observed within the crystalline core.

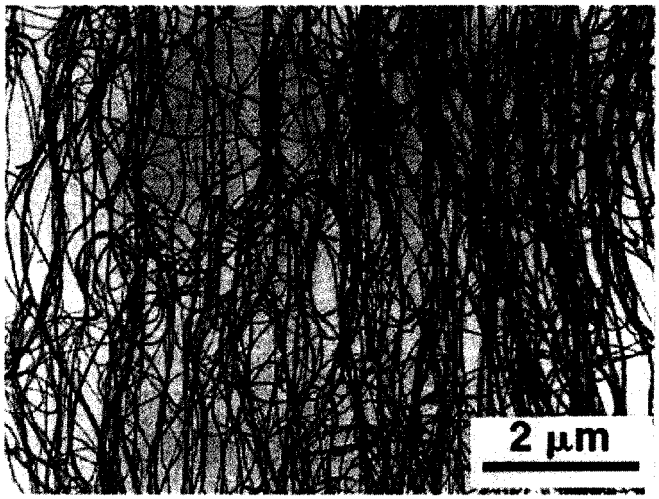

Figure A.3. TEM image of silicon nanowire grown by laser ablation via the OAM [45].

From this experiment, Lee *et al.* [45] draw the following observations to bolster their proposed OA mechanism. Si nanowires are also grown even with target made of pure silicon powder (99.995%), though the yield is low. Introduction of SiO_2 into the Si

powder target greatly enhances the growth of silicon nanowires. Peak yield occurs at one-to-one weight ratio of SiO_2 and Si, where the yield is thirty times higher compared to pure silicon source. If the SiO_2 containing source is switched with a pure Si source after formation of Si nanowire nuclei, no further growth is observed. Morphology and structure of Si nanowires grown using high-purity SiO powder are very similar to those grown from the Si/SiO_2 solid source. Morphology of germanium nanowires grown with a GeO_2-containing Ge target is similar to morphology of the Si nanowires. Each nanowire also consists of a crystalline Ge core and a thick amorphous oxide sheath.

Additionally, HRTEM investigation reveals no metal alloy tip in any of the wires grown with metal-containing targets. Electron energy dispersive spectroscopy data show only silicon and oxygen in the wires; no metal is detected, even in the tip. The tip of a nanowire is generally spherical and covered with a relatively thick silicon oxide sheath. The silicon crystalline core of the tip also contains high density of crystal defects.

Lee *et al.* [45] propose the growth mechanism, similar to Wang *et al.* [44]'s, as followed:

(a) $Si_xO_{(s)} \rightarrow Si_{x-1\,(s)} + SiO_{(s)} \qquad (x > 1)$

(b) $2\,SiO_{(s)} \rightarrow Si_{(s)} + SiO_{2\,(s)}$

At higher temperature zone ~1400 °C, a new morphology is observed. The wires are straight, approximately millimeters long and 100 nm in diameter. Iron is detected at the tip of the wire by EDX, indicative of the VLS mechanism. This is probably due to the high molten temperature of iron-silicide. Hence, there could be an intermediate

temperature between 900 - 1100 °C and ~ 1400 °C where both mechanisms compete with each other.

A.2.3 Dependence on Temperature and Pressure of the Oxide-Assisted Model

Also in 2000, Zhang *et al.* [46] conduct a study to examine the effects of temperature and pressure on the yield of silicon nanowires grown by the OAM to explore the feasibility of mass production. In this study, SiO powder is sublimated at approximately 950 °C inside a quartz tube. The SiO vapor is carried by high purity argon gas at 50 sccm down stream from the source and deposit on the regions of the reactor where temperature is less than 920 °C to form silicon oxide nanowires.

The average diameter of the nanowires after 5 hours of growth is 15 nm with the range from 6 to 28 nm. The lengths could be as long as a few millimeters. Growth rate in axial direction is up to 8 μm per minute. Some wires have kinks and bends along the bodies.

EDX analysis shows the composition of the wires is silicon and oxygen in one-to-one atom ratio. Under HRTEM, the nanowires consist of a crystalline cubic silicon core and an amorphous silicon dioxide sheath. No metal is detected in the tips of the wires, as shown in Figure A.4.

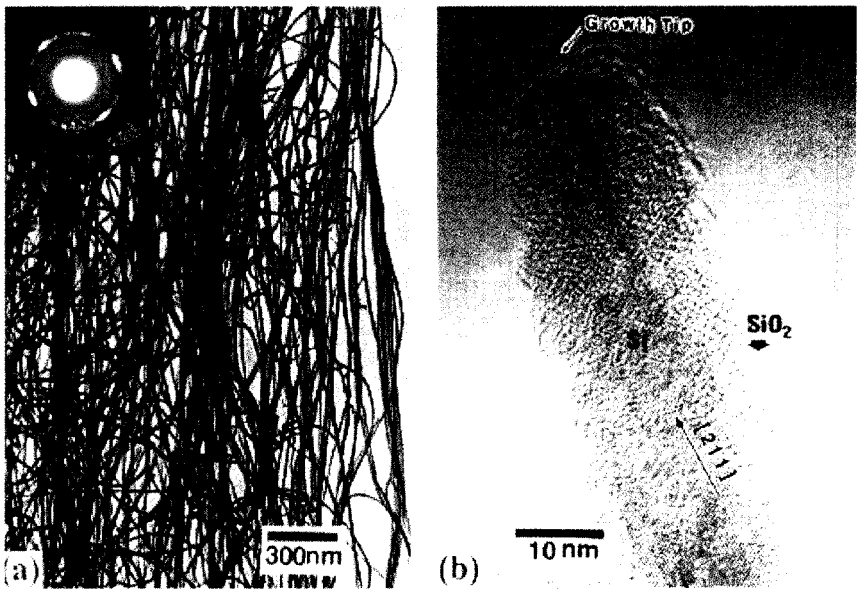

Figure A.4. (a) - (b) Morphology of Si NW by SiO sublimation. (b) There is no metal catalyst at the growth tip and the wire is made of an inner crystalline Si core and an outer amorphous SiO_2 sheath [46].

Based on the Oxide-Assisted model, Zhang *et al.* [46] propose the growth sequence of silicon nanowires as followed. During sublimation at 950 °C, SiO molecules in the vapor phase combine into nanoclusters to minimize the free energy. These nanoclusters deposit on substrate where the surface temperature is lower than 950 °C to form a viscous matrix of SiO. Subsequent disproportionation results in precipitation of silicon to form an inner crystalline structure and an outer oxide sheath.

When pressure is maintained at $4x10^4$ Pa, the yield of Si nanowires follows an Arrhenius dependency on temperature. The activation energy for vaporization of Si powder is calculated to be 2.0 eV. When the sublimation temperature is maintained at 1300 °C, the yield of Si nanowires increases with increasing pressure of the argon carrier gas. The dependence of yield on temperature and on pressure is shown in Figure A.5.

From Figure A.5.b, it can be deduced that further increase in pressure beyond the reported range will not lead to any further increase in yield. Minimization of mass-transport limitation accounts for this pressure-dependence yield increase behavior.

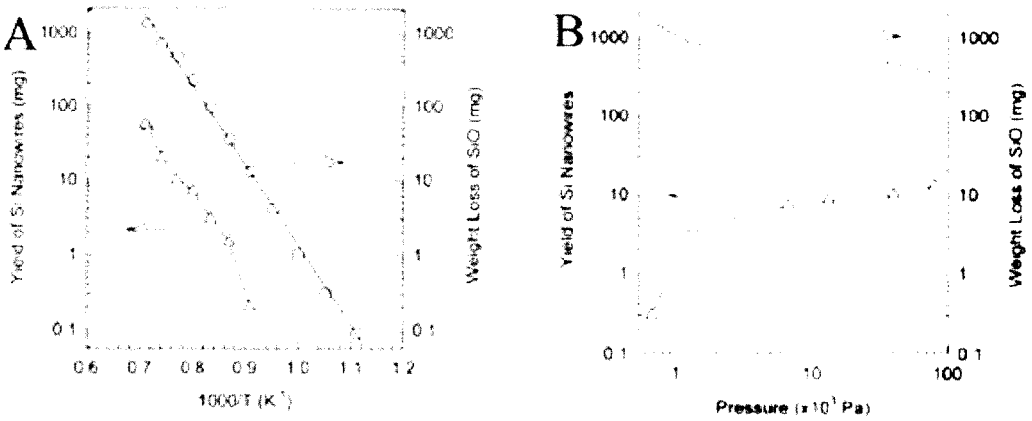

Figure A.5. (a) Si NW yield and SiO source weight loss as function of temperature and (b) Si NW yield and SiO source weight loss as function of pressure [46].

It is unstated in this paper how high the defect density is. Based on the mechanism itself, crystal defects are intrinsic to this growth method. Evidently, growth by the Oxide-Assisted model is a function of the thermal evaporation temperature, the total pressure, and the source : oxide mixing ratio. Although massive production of silicon nanowires is attainable, the drawbacks of growth by this method are plenty. The high defect density causes low wire-to-wire uniformity and eliminates any potential optoelectronic application. Nanowire morphology and growth orientation are difficult to control. Furthermore, localization control is also complicated. Regardless, there may be cases where nanowires grown by this mechanism are desirable.

Subsequently, the oxide-assisted model is found to also apply to the growth of GaAs [47] and GaN [48] nanowires as well, not only silicon and germanium nanowires. Thus, if an oxide is present in the reactor apparatus, then wires can potentially undergo growth via the OAM. During synthesis of metal oxide nanowires, growth via the OAM may occur when growth by the VLS mechanism is intended. As noted in Lee *et al.* [45], temperature may be a critical parameter. Again, it is shown in Lee *et al.* [45] that a different mechanism (OAM), instead of the one intended (VSM), takes precedence under a given set of growth conditions.

APPENDIX B

THERMODYNAMIC CALCULATIONS

B.1 Enthalpy of formation

B.1.1 Born-Haber cycle

The Born-Haber cycle for tin (IV) oxide is drawn in Figure B.1; the enthalpy of formation calculation based on thermodynamic data is shown later in this chapter. The values of lattice enthalpy of formation are tabulated in Table B.1. Clearly, preliminary analysis appears to indicate that indium (III) oxide should be the major constituent of the nanowire as indium is more volatile and indium (III) oxide is more stable.

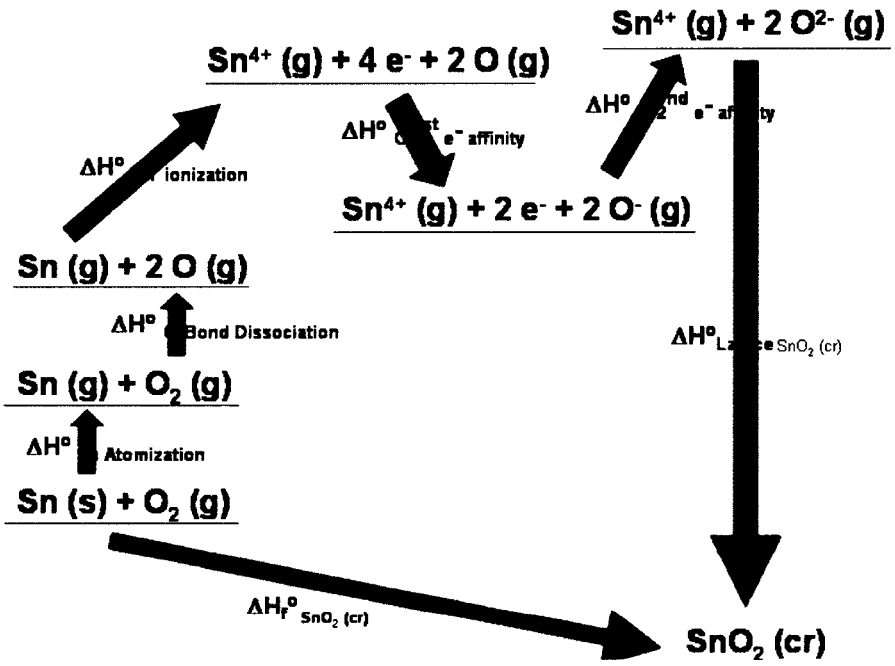

Figure B.1. A Born-Haber cycle for calculation of enthalpy of formation of SnO_2.

Table B.1. Standard enthalpy of formation for various metal oxides.

Species	ΔH^{o}_{F} (Born-Haber Cycle) (kJ/mol)	ΔH^{o}_{F} (TD Data) (kJ/mol)
In_2O_3 (cr)	-783.82	-923.00
SnO_2 (cr)	-513.90	-577.63
SnO (cr)	-279.79	-280.71

B.1.2 Binding Energy

The binding energy is approximated by the change in enthalpy of sublimation, which is the sum of the change in enthalpy of fusion and change in enthalpy of evaporation.

$$E_b \cong \Delta H_{sublimation} = \Delta H_{melt} + \Delta H_{evap}$$

It can also be computed theoretically by the equation given below.

$$E_b = \frac{1}{2} CN\ N_{AV} U_{POT\ min} \qquad \text{Equation B.1}$$

CN is the coordination energy, N_{AV} is the Avogadro's number, and $U_{POT\ min}$ is the minimum lattice potential energy at the equilibrium separation distance.

$U_{POT\ min}$ can be calculated via either the Born-Mayer equation or the Kapustinskii equation. The Born-Mayer equation requires the Madelung geometric factor α, which is not available for many crystalline species. The Kapustinskii equation is more flexible as the factor is easier to compute. The binding energy for the three metal oxides species are tabulated in Table B.2. Calculation of the minimum lattice potential energy is based on the Kapustinskii equation.

Born-Mayer Equations:

$$U_{POT} = \left(\frac{e^2 N_{AV}\alpha}{4\pi\varepsilon_o}\right)(Z_+Z_-)\left(\frac{1}{d}-\frac{d^*}{d^2}\right) \text{ or } U_{POT} = 1390^{kJ\ \mathring{A}/mol}(\alpha\ Z_+Z_-)\left(\frac{1}{d}-\frac{d^*}{d^2}\right)$$

$$U_{POT\ \min}(kJ/mol) = \frac{139\ \alpha\ Z_+Z_-}{r_+ + r_-}\left(1-\frac{0.0345}{r_+ + r_-}\right)$$

Kapustinskii Equations:

$$U_{POT} = 1210^{kJ\ \mathring{A}/mol}(n\ Z_+Z_-)\left(\frac{1}{d}-\frac{d^*}{d^2}\right)$$

$$U_{POT\ \min}\ (kJ/mol) = \frac{121.4\ n\ Z_+Z_-}{r_+ + r_-}\left(1-\frac{0.0345}{r_+ + r_-}\right)$$

The variables are defined as followed:

e = charge of electron

ε_o = permittivity of vacuum

Z = nuclear charge

r = ionic radius

d = inter-atomic distance

d* = scaling factor for repulsive term

n = number of ions in the formula unit

α = Madelung factor

+/- = denote the cation and anion, respectively.

Table B.2. Theoretical lattice binding energy for the crystalline metal oxide species.

Species	r_+/r_-	CN	$U_{POT\ MIN}$ (kJ/mol)	E_B (kJ/mol)
In_2O_3 (cr)	0.606	6	-14390	-43169
SnO_2 (cr)	0.561	6	-11781	-35343
SnO (cr)	0.689	6	-3688	-11063

B.2 Thermodynamic Analysis of Synthesis Phenomena

B.2.1 Theory

The following thermodynamic analysis is performed to determine which reaction is more favorable. The change in Gibbs free energy of a reaction is given by Equation B.2,

$$\Delta G_{rxn} = \Delta H_{rxn} - T\Delta S_{rxn} \qquad \text{Equation B.2}$$

where enthalpy of reaction and entropy of reaction is given by Equations B.3 and B.4.

$$dH = Cp\ dT + V(1-\beta T)\ dP \qquad \text{Equation B.3}$$

$$dS = Cp\,{}^{dT}\!/_{T} - \beta V\ dP \qquad \text{Equation B.4}$$

Assuming isobaric condition, Equations B.3 and B.4 are reduced to

$$dH = Cp\ dT \qquad \text{Equation B.5}$$

$$dS = Cp\,{}^{dT}\!/_{T} \qquad \text{Equation B.6}$$

To simplify calculations, an acceptable assumption renders the heat capacity of each species constant. Here, to improve the accuracy of the calculation, the heat capacity of each species as a function of temperature is given as an experimental best-fit function of the form

$$\frac{C_P^o(T)}{R} = \frac{a_1}{T^2} + \frac{a_2}{T} + a_3 + a_4 T + a_5 T^2 + a_6 T^3 + a_7 T^4,$$

and the entropy and enthalpy of formation as function of temperature are calculated based on the equations given below.

$$\frac{S^o(T)}{R} = -\frac{a_1}{2T^2} - \frac{a_2}{T} + a_3 \ln(T) + a_4 T + \frac{a_5 T^2}{2} + \frac{a_6 T^3}{3} + \frac{a_7 T^4}{4} + b_2 \qquad \text{Equation B.7}$$

$$\frac{H\ (T)}{RT} = -\frac{a_1}{T^2} + \frac{a_2}{T} \ln(T) + a_3 + \frac{a_4 T}{2} + \frac{a_5 T^2}{3} + \frac{a_6 T^3}{4} + \frac{a_7 T^4}{5} + \frac{b_1}{T} \qquad \text{Equation B.8}$$

The constants are provided in handbooks such as McBride *et al.* 2002.

The last two equations can be applied to calculate the enthalpy, entropy and Gibbs free energy of formation or of reaction as functions of temperature. And representative values of enthalpy and entropy of formation of various species at various temperatures are tabulated in Tables B.3.a and B.3.b.

Table B.3.a. Enthalpies of formation of various species for 1000 K < T < 1400 K

	Enthalpy of Formation as Function of Temperature (kJ/mol)								
T (K) -->	1000	1050	1100	1150	1200	1250	1300	1350	1400
In (cr/l)	22.9	24.3	25.6	27.0	28.3	29.7	31.1	32.4	33.8
In (g)	257.3	258.7	260.0	261.4	262.7	264.1	265.4	266.8	268.1
InO (g)	174.6	176.7	178.9	181.0	183.2	185.3	187.4	189.5	191.6
In_2O (g)	4.1	7.0	9.8	12.7	15.6	18.5	21.3	24.2	27.1
In_2O_3 (cr)	-838.5	-832.0	-825.5	-818.9	-812.3	-805.7	-799.1	-792.4	-785.7
In_2O_3 (l)	-761.3	-753.3	-745.3	-737.3	-729.3	-721.3	-713.3	-705.3	-697.3
Sn (cr)	27.2	28.6	30.0	31.4	32.8	34.2	35.6	37.0	38.4
Sn (g)	321.0	322.7	324.3	326.0	327.6	329.3	330.9	332.5	334.1
Sn_2 (g)	451.0	453.2	455.4	457.5	459.7	461.9	464.1	466.2	468.4
SnO (g)	46.6	48.5	50.3	52.2	54.0	55.9	57.7	59.6	61.5
SnO (cr)	-243.8	-241.0	-238.0	-235.1	-232.1	-229.1	-226.0	-222.9	-219.8
SnO (l)	-217.1	-214.0	-210.8	-207.7	-204.5	-201.4	-198.2	-195.1	-191.9
SnO_2 (g)	279.4	281.4	283.4	285.2	287.1	288.9	290.6	292.3	294.0
SnO_2 (cr)	-526.1	-522.1	-518.0	-513.8	-509.7	-505.5	-501.3	-497.1	-492.8
SnO_2 (l)	-508.5	-503.9	-499.3	-494.7	-490.1	-485.5	-480.9	-476.3	-471.7
O (g)	264.0	265.1	266.1	267.2	268.2	269.3	270.3	271.3	272.4
O_2 (g)	22.7	24.5	26.2	28.0	29.8	31.6	33.4	35.2	37.0
C (s)	11.8	12.9	14.0	15.1	16.2	17.4	18.5	19.7	20.9
C (g)	731.2	732.3	733.3	734.4	735.4	736.4	737.5	738.5	739.6
CO (g)	-88.8	-87.2	-85.5	-83.8	-82.1	-80.4	-78.7	-76.9	-75.2
CO_2 (g)	-360.1	-357.4	-354.6	-351.8	-349.0	-346.2	-343.4	-340.5	-337.6

Table B.3.a. Enthalpies of formation of various species for 1000 K < T < 1400 K

	Entropy of Formation as Function of Temperature (kJ/mol K)								
T (K) -->	1000	1050	1100	1150	1200	1250	1300	1350	1400
In (cr/l)	0.099	0.101	0.102	0.103	0.104	0.105	0.106	0.107	0.108
In (g)	0.202	0.203	0.204	0.205	0.207	0.208	0.209	0.210	0.211
InO (g)	0.287	0.289	0.291	0.293	0.295	0.296	0.298	0.300	0.301
In_2O (g)	0.368	0.371	0.374	0.376	0.379	0.381	0.383	0.385	0.388
In_2O_3 (cr)	0.244	0.251	0.257	0.263	0.268	0.274	0.279	0.284	0.289
In_2O_3 (l)	0.273	0.281	0.289	0.296	0.302	0.309	0.315	0.321	0.327
Sn (cr)	0.100	0.101	0.103	0.104	0.105	0.106	0.107	0.108	0.109
Sn (g)	0.201	0.203	0.204	0.206	0.207	0.208	0.210	0.211	0.212
Sn_2 (g)	0.318	0.320	0.322	0.324	0.326	0.328	0.330	0.331	0.333
SnO (g)	0.274	0.276	0.278	0.279	0.281	0.282	0.284	0.285	0.287
SnO (cr)	0.120	0.122	0.125	0.128	0.130	0.133	0.135	0.137	0.140
SnO (l)	0.141	0.144	0.147	0.150	0.152	0.155	0.157	0.160	0.162
SnO_2 (g)	0.320	0.323	0.325	0.328	0.331	0.333	0.336	0.338	0.340
SnO_2 (cr)	0.135	0.139	0.143	0.146	0.150	0.153	0.157	0.160	0.163
SnO_2 (l)	0.143	0.147	0.151	0.156	0.159	0.163	0.167	0.170	0.174
O (g)	0.187	0.188	0.189	0.190	0.191	0.191	0.192	0.193	0.194
O_2 (g)	0.244	0.245	0.247	0.249	0.250	0.251	0.253	0.254	0.256
C (s)	0.024	0.026	0.027	0.028	0.029	0.029	0.030	0.031	0.032
C (g)	0.183	0.184	0.185	0.186	0.187	0.188	0.189	0.190	0.190
CO (g)	0.235	0.236	0.238	0.239	0.241	0.242	0.243	0.245	0.246
CO_2 (g)	0.269	0.272	0.275	0.277	0.279	0.282	0.284	0.286	0.288

Using Equations B.9 and B.10, the concentrations of the respective metal species are calculated as followed, assuming near-ideal behaviors at elevated temperature.

$$\Delta G^{o} = -RT \ln K \qquad \text{Equation B.9}$$

$$\Delta G = \Delta G^{o} + RT \ln Q \qquad \text{Equation B.10}$$

A negative value of the Gibbs free energy of reaction denotes a spontaneous reaction, as written; a positive Gibbs free energy of reaction signifies non-spontaneity. Furthermore, as soon as the Gibbs free energy of reaction is obtained, the vapor concentration of the gas-phase species can be calculated. For the generic two-phase reaction

$$a\,A_{(s)} + b\,B_{(s)} \rightarrow c\,C_{(g)} + d\,D_{(g)}.$$

The equilibrium constant for the reaction is given in Equation B.10, where a_i is the activity of species "i".

$$K \equiv \frac{-\Delta G^{o}_{RXN}}{RT} = \frac{\alpha_C^{c} * \alpha_D^{d}}{\alpha_A^{a} * \alpha_B^{b}} \qquad \text{Equation B.11}$$

A complete thermodynamic analysis is beyond the scope of this study, multiple simplifications are made to minimize mathematical complexity. Consequently, unity is assigned to the activities of the solids and ideal gas behaviors are attributed to the gaseous species. This assumption is reasonable as the products and reactions are of different phases and the reaction condition is at elevated temperature and atmospheric pressure. Using stochiometry, the expression for the equilibrium constant simplifies to equations.

$$K = P_C^c \; P_D^d = P_C^c \left({}^{d}\!/_{c} \; P_C \right)^d, \text{ and}$$

$$Q \equiv \frac{-\Delta G_{RXN}}{RT} = P_C^c \left({}^{d}\!/_{c} \; P_C \right)^d$$

Thus, the partial pressures at the source can be obtained from the Gibbs free energy calculation. The sign of ΔG or the ratio of Q/K reveals the spontaneity of the reaction.

B.2.2 Calculations

B.2.2.1 Thermodynamics at source

Before proceeding further, it must be explicitly stated that the following thermodynamic analysis is based on bulk properties only. This analysis provides a crude picture of what potentially occurs in the system but, by no means, provides a complete and absolute representation of the actual system.

Figures B.2.a-b plots the change in Gibbs free energy of reaction as function of temperature for generation of indium-containing species. Figure B.2.b is simply a zoom-in reproduction of Figure B.2.a. According to the calculations, only the generation of liquid indium and carbon dioxide via reduction of liquid indium (III) oxide by carbon monoxide is spontaneous at the temperature range. The reduction of crystalline indium (III) oxide by carbon monoxide to liquid indium and carbon dioxide has ΔG_{rxn} (T) less than 10 kJ per mole. Thus, this reaction is also expected to contribute significantly to the generation of indium vapor. As detailed subsequently, carbon monoxide is generated by carbothermal reduction of tin oxide. As it percolates up the source matrix, it is chemisorbed and/or physisorbed into the solid powder to reduce the metal oxides.

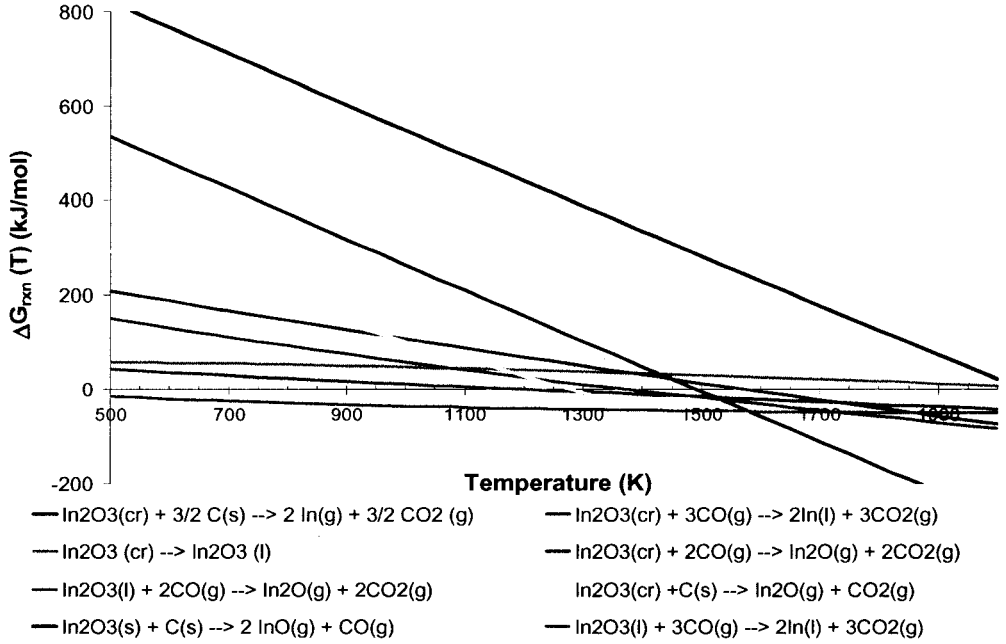

Figure B.2.a. Change in Gibbs free energy of reaction as function of temperature for generation of indium-containing vapors at the source.

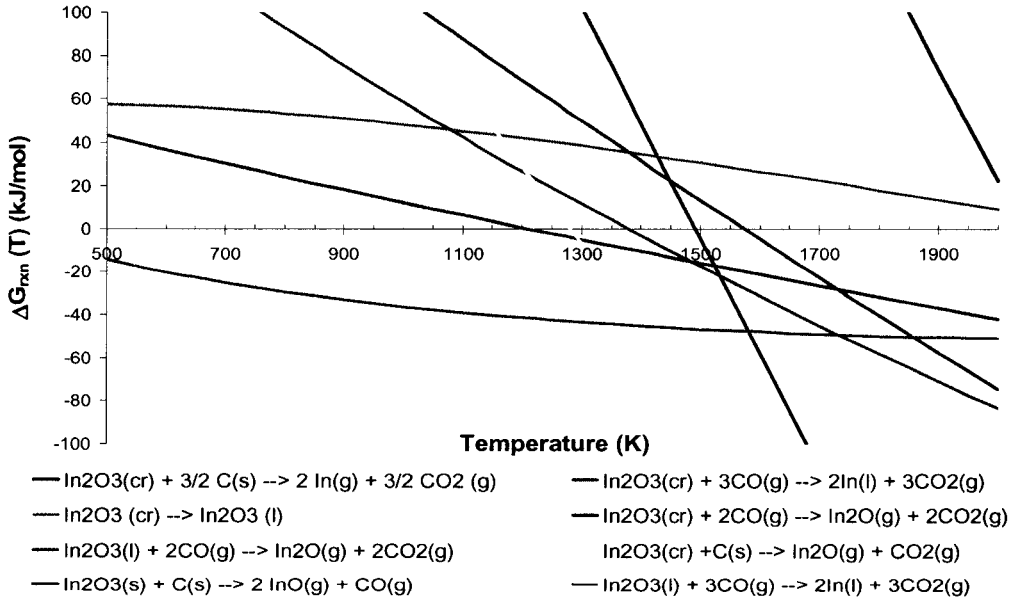

Figure B.2.b. Change in Gibbs free energy of reaction as function of temperature for generation of indium-containing vapors at the source.

Although the other as-written reactions are not spontaneous at the conditions, they are all expected to proceed to the right to certain extent because the products are quickly liberated from the source mixture and convected downstream by the argon carrier gas. Interestingly, carbothermal reduction of crystalline indium (III) oxide to gaseous indium (I) oxide and indium (II) oxide, along with the reduction of crystalline indium (III) oxide to liquid indium, rapidly become spontaneous at temperature above 1200K. Therefore, increase in vapor pressure of indium-containing vapors is expected at higher range of temperature. This observation has been confirmed in subsequent experiments.

Figures B.3.a-b plots the change in Gibbs free energy of reaction as function of temperature for generation of tin-containing species. Figure B.3.b is simply a zoom-in reproduction of Figure B.3.b. As concluded previously, tin oxide exists both as tin (II) oxide and tin (IV) oxide in the source mixture. Both stannous and stannic tin can potentially exist in a semi-liquid state in the reaction due to elevated temperature and reduced particle size, especially tin (II) oxide as its melting point is 1250 K and the reaction temperature is 1123 K. At elevated temperature, tin (IV) oxide is reduced via carbothermal reduction to tin (II) oxide and carbon monoxide. As the carbon monoxide percolates upward through the source matrix, it is either chemisorbed or physisorbed onto the surface of the tin oxide micro-particles. There, a secondary reduction reaction proceeds to produce metallic tin and carbon dioxide from carbon monoxide and tin (II) oxide. Upon completion of the reaction, tin and carbon dioxide are rapidly vaporized out of the source container into the mainstream flow. Due to the low melting temperature of tin (II) oxide, some evaporation of tin (II) oxide is expected.

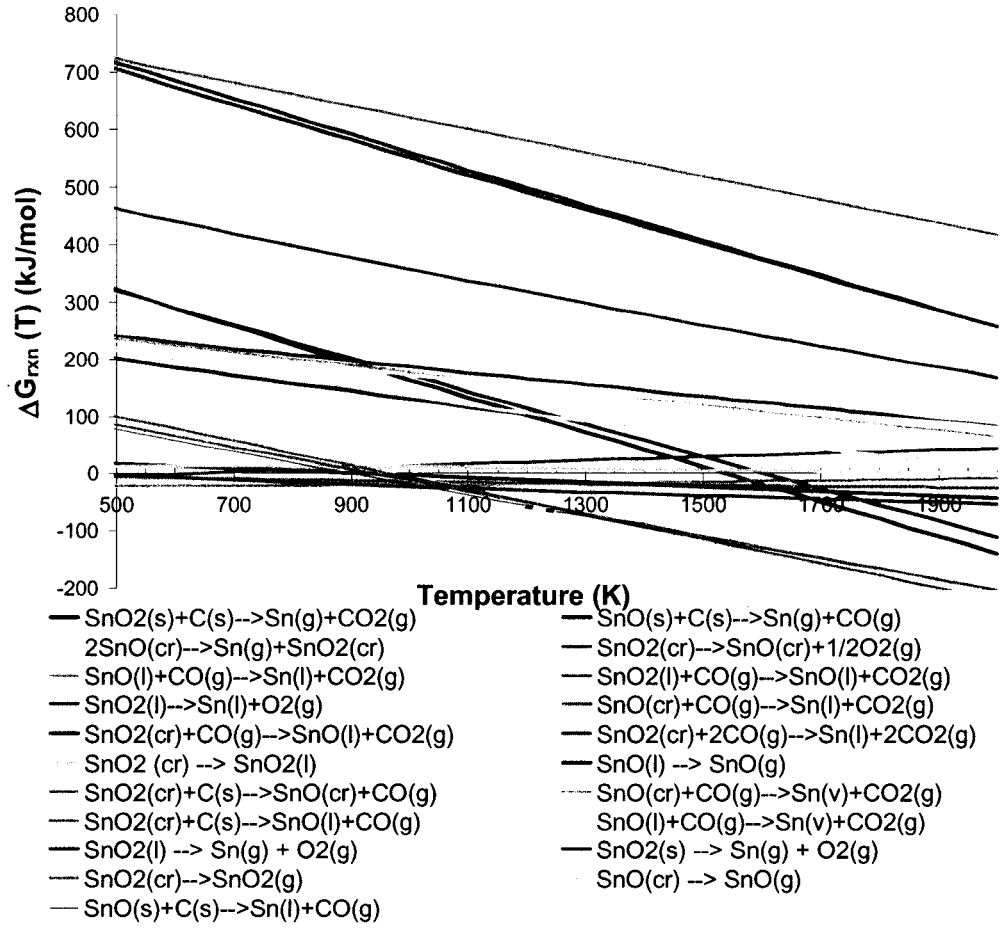

Figure B.3.a. Change in Gibbs free energy of reaction as function of temperature for generation of tin-containing vapors at the source.

It is noted that solid tin (IV) oxide can be also reduced by tin vapor to solid tin (II) oxide. However, this reaction is not favorable. Figure B.3.b shows that carbothermal reduction of tin (II) oxide to liquid tin and gaseous carbon monoxide is the most spontaneous tin-generation reaction at the reaction conditions. Consequently, carbon monoxide is in ample supply for other reactions at the source.

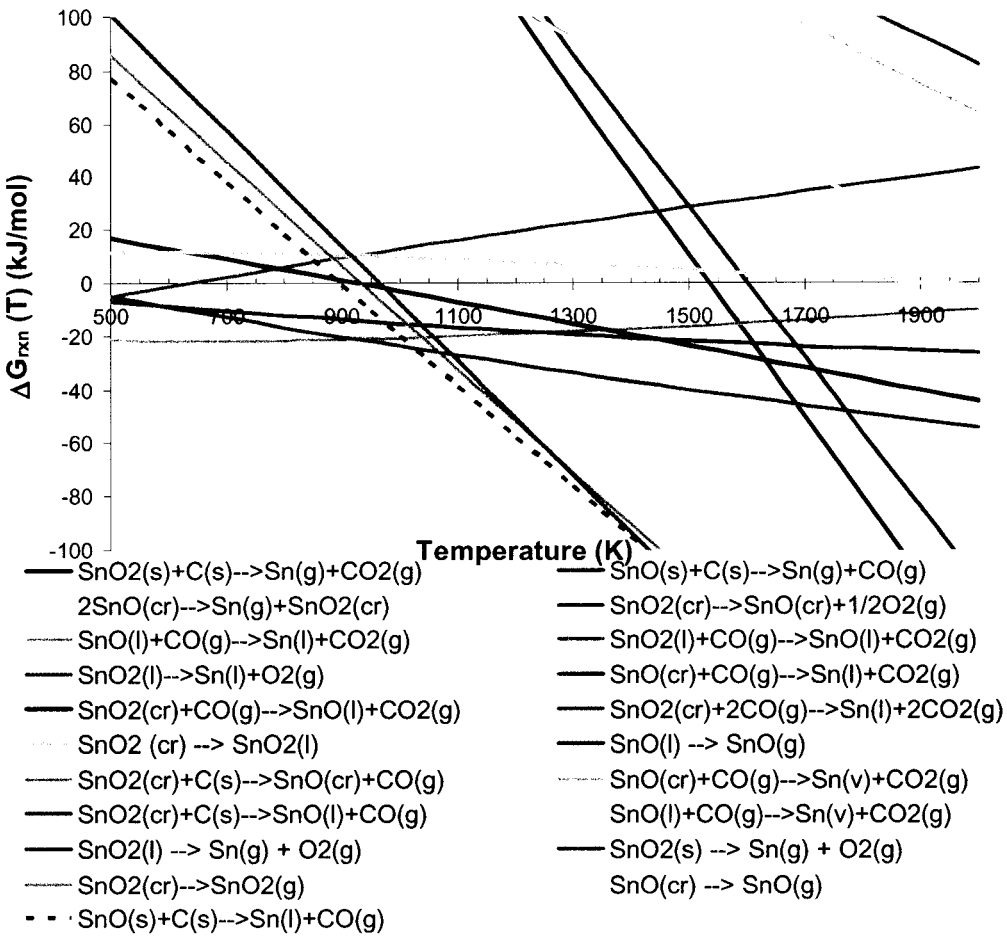

Figure B.3.b. Change in Gibbs free energy of reaction as function of temperature for generation of tin-containing vapors at the source.

According to the previous analysis, tin-containing vapors should be present in significantly higher concentration compared to indium-containing vapors. It is desirable to be able to determine the relative ratio of the two species in the gas-phase. Unfortunately, due to the numerous reactions involved and the complexity of the interactions among them, an accurate calculation requires an enormous computational prowess. Thus, it is recommended to be performed in another study.

A qualitative analysis is presented in Tables B.4.a-b. In the tables the equilibrium constant and the reaction quotient, as well as the Q/K ratio, are presented for the temperature at 1150 Kelvin. The Q/K ratio denotes the spontaneity of the as-written reaction equations. The smaller the ratio, the more it will proceed to the right of the as-written reaction; the larger the ratio, the more it will proceed to the left of the as-written reaction.

Table B.4.a. Equilibrium constant and reaction quotient of the indium-generation reactions at 1150 Kelvin.

Potential Reactions	K (1150 K)	Q (1150 K)	Q/K
In_2O_3(cr) + 3/2 C(s) --> 2 In(g) + 3/2 CO_2 (g)	4.5729E-30	8.5605E-22	1.8720E+08
In_2O_3(l) + 3 CO(g) --> 2 In(l) + 3 CO_2 (g)	6.6471E+01	1.5962E-02	2.4014E-04
In_2O_3(cr) + 3 CO(g) --> 2 In(l) + 3 CO_2 (g)	6.9804E-01	4.3118E-03	6.1770E-03
In_2O_3 (cr) --> In_2O_3 (l)	2.8366E-03	2.7012E-01	9.5226E+01
In_2O_3(cr) + 2 CO(g) --> In_2O(g) + 2 CO_2 (g)	2.8780E-04	1.1703E-08	4.0665E-05
In_2O_3(l) + 2 CO(g) --> In_2O(g) + 2 CO_2 (g)	2.7406E-02	4.3327E-08	1.5809E-06
In_2O_3(cr) + C(s) --> In_2O(g) + CO_2 (g)	1.2310E-17	1.6880E-15	1.3713E+02
In_2O_3(cr) + C(s) --> 2 InO(g) + CO (g)	3.7320E-43	5.9205E-22	1.5864E+21
In(l) --> In(v)	1.0161E-16	3.0078E+03	2.9601E+19

Table B.4.b. Equilibrium constant and reaction quotient of the tin-generation reactions at 1150 Kelvin.

Potential Reactions	K (1150 K)	Q (1150 K)	Q/K
$SnO_2(s) + C(s) \rightarrow Sn(g) + CO_2(g)$	2.6220E-18	5.8317E-13	2.2242E+05
$SnO(s) + C(s) \rightarrow Sn(g) + CO(g)$	5.2609E-18	3.8714E-12	7.3588E+05
$2\ SnO(cr) \rightarrow Sn(g) + SnO_2(cr)$	2.8883E-12	1.7819E-04	6.1692E+07
$SnO_2(cr) \rightarrow SnO(cr) + 1/2\ O_2(g)$	1.0520E-12	6.2375E-05	5.9294E+07
$SnO(l) + CO(g) \rightarrow Sn(l) + CO_2(g)$	7.9094E+00	1.3222E+00	1.6716E-01
$SnO_2(l) + CO(g) \rightarrow SnO(l) + CO_2(g)$	1.5744E-01	2.7340E+01	1.7365E+02
$SnO_2(l) \rightarrow Sn(l) + O_2(g)$	1.3054E-15	8.2917E-09	6.3520E+06
$SnO(cr) + CO(g) \rightarrow Sn(l) + CO_2(g)$	6.2660E+00	2.7798E-01	4.4363E-02
$SnO_2(cr) + CO(g) \rightarrow SnO(l) + CO_2(g)$	2.6211E+00	3.1671E-02	1.2083E-02
$SnO_2(cr) + 2CO(g) \rightarrow Sn(l) + 2CO_2(g)$	2.0731E+01	4.1874E-02	2.0198E-03
$SnO_2(cr) \rightarrow SnO_2(l)$	3.5732E-01	8.6589E-01	2.4233E+00
$SnO(l) \rightarrow SnO(g)$	9.3009E-06	2.8047E-06	3.0155E-01
$SnO_2(cr) + C(s) \rightarrow SnO(cr) + CO(g)$	1.8215E-06	2.1727E-08	1.1928E-02
$SnO(cr) + CO(g) \rightarrow Sn(v) + CO_2(g)$	1.4395E-12	2.6841E-05	1.8646E+07
$SnO_2(cr) + C(s) \rightarrow SnO(l) + CO(g)$	3.0338E-07	4.5679E-09	1.5057E-02
$SnO(l) + CO(g) \rightarrow Sn(v) + CO_2(g)$	8.6425E-12	1.2767E-04	1.4772E+07
$SnO_2(l) \rightarrow Sn(g) + O_2(g)$	1.1172E-23	8.0064E-13	7.1662E+10
$SnO_2(s) \rightarrow Sn(g) + O_2(g)$	4.6105E-24	6.9326E-13	1.5037E+11
$SnO_2(cr) \rightarrow SnO_2(g)$	1.2538E-35	7.8920E-09	6.2944E+26
$SnO(cr) \rightarrow SnO(g)$	4.3449E-12	5.8967E-07	1.3572E+05
$SnO(s) + C(s) \rightarrow Sn(l) + CO(g)$	1.5877E+02	4.0093E-08	2.5252E-10
$Sn(l) \rightarrow Sn(v)$	2.0198E-19	2.6039E+03	1.2892E+22

A comparison of Tables B.4.a-b shows that Q/K ratio for the reduction of tin (II) oxide to tin and carbon monoxide is four orders of magnitude smaller than the reduction of quasi-liquid indium (III) oxide to indium (I) oxide and carbon monoxide. Also, all indium-generation reactions having the Q/K ratio less than unity require carbon monoxide, which must be generated by the reduction of tin oxide. Thus, despite the fact that bulk indium metal has much higher vapor pressure than bulk tin metal, as discussed previously and shown here with the Q/K ratios, tin-containing vapor species are present in much high concentration due to the many alternative pathways and the low energy barrier for the tin-oxide system. If the following assumptions can be made, then the ratio

of the partial pressure of tin-containing vapor species to the partial pressure of indium-containing vapor species is 148:1 using the reaction quotient.

1. All reactions are independent,
2. System is in a quasi-equilibrium state,
3. System exhibits ideal bulk solid or liquid behavior,
4. Carbon monoxide is generated only by carbothermal reduction of tin (II) oxide and tin (IV) oxide,
5. Local concentration of carbon monoxide is constant, and
6. Liquid-gas phase transformation of tin and indium is constrained by the generation of the liquid metals.

B.2.2.2 Thermodynamics in the gas phase

Although it has been widely assumed that majority of the reactions proceed within the semi-liquid alloy catalytic droplet, in this study, polycrystalline thin film and metal oxide whiskers are located both in the high temperature zone above the source and near the exit of the chamber where temperature rapidly descend from reaction temperature to near room temperature. Thus, it is deduced gaseous interplay proceed at reaction condition and precipitation of metal oxide required not the gold catalyst. However, it is recognized that gold catalyst is necessary for directing the growth orientation and nanowire localization. In this section, the gas phase reactions are investigated for their corresponding spontaneity.

The Gibbs free energy of reaction is plotted in Figures B.4.a-b. Many reactions have negative ΔG_{rxn} (T) within the temperature process window. Magnitude of the negative ΔG_{rxn} (T) diminishes with increasing temperature. The reason is because most of these are gas-phase condensation reaction and the entropy term in Equation B.2 dominates at elevated temperature. Even with a relatively large negative ΔG_{rxn} (T), it is difficult to speculate on the instantaneity of the reaction.

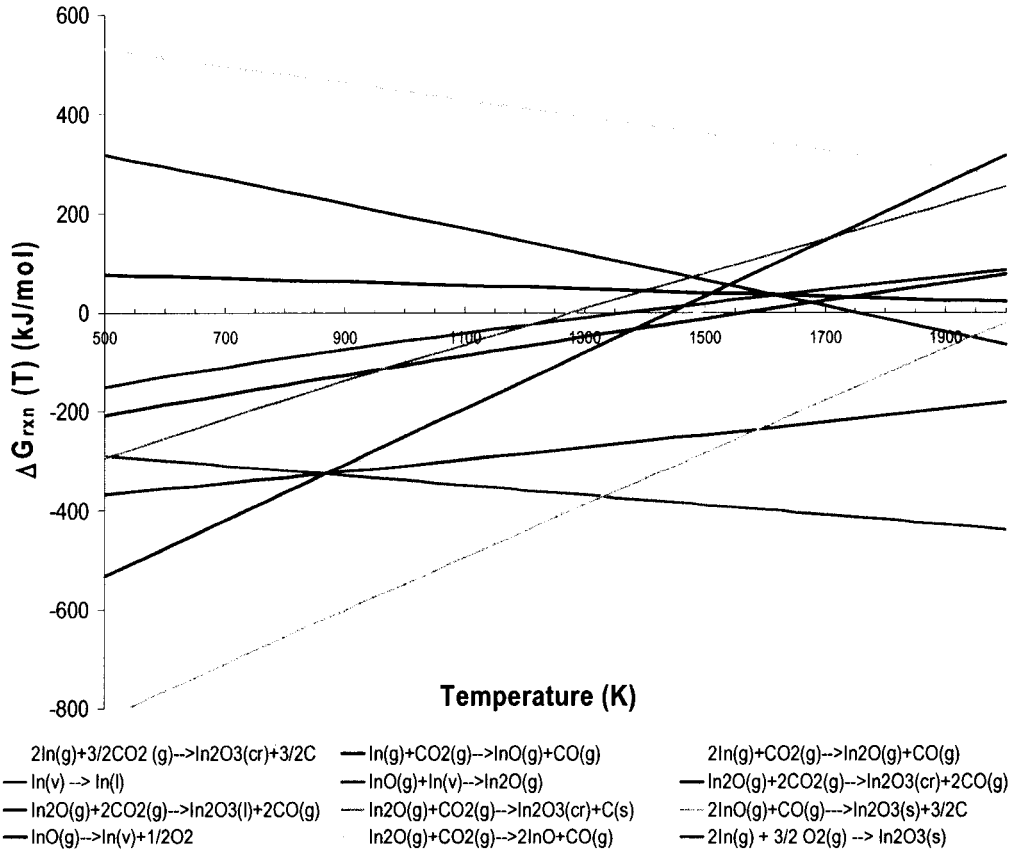

Figure B.4.a. Change in Gibbs free energy of reaction as function of temperature for consumption of indium-containing vapors in the gas phase, downstream of the source.

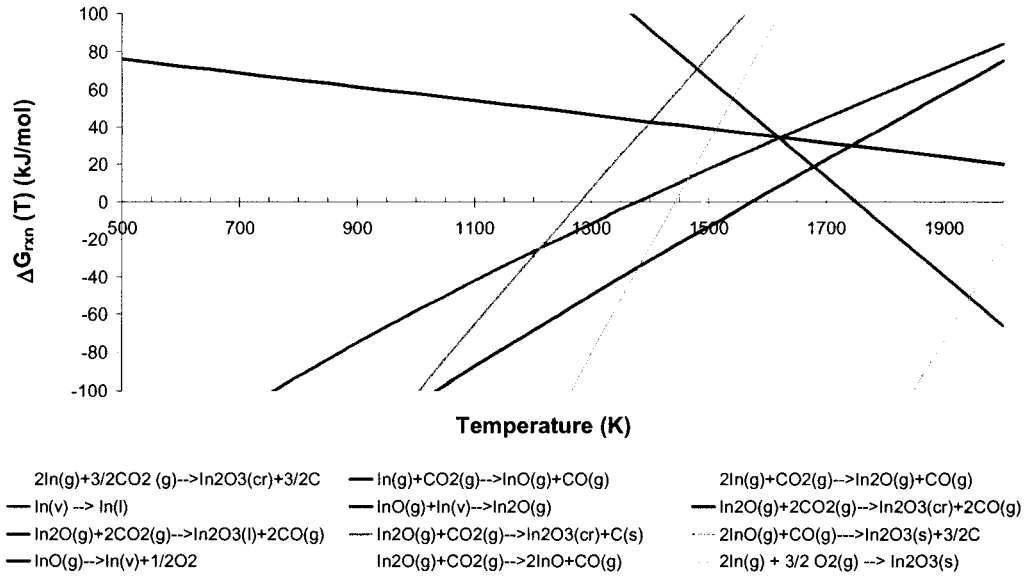

Figure B.4.b. Change in Gibbs free energy of reaction as function of temperature for consumption of indium-containing vapors in the gas phase, downstream of the source.

B.2.2.3 Gas-phase

For the indium oxide sub-system, decomposition of indium (II) oxide to indium vapor and molecular oxygen is not spontaneous at reaction conditions. However, the equilibrium constant K is only 1 E-4 at 1100 Kelvin; thus, some decomposition may occur to generate molecular oxygen in the system. The generation of indium (II) oxide and carbon monoxide from indium (I) oxide vapor and carbon dioxide gas is highly unfavorable as the equilibrium constant is 2 E-26 at 1100 Kelvin.

All reactions which produce crystalline indium (III) oxide are highly favorable. Indium vapor can react readily with carbon dioxide to form indium (I) oxide and carbon monoxide. Any indium (II) oxide that exists in the system will form indium (I) oxide by reacting with indium vapor or form indium vapor and carbon dioxide by oxidizing carbon

monoxide. Subsequently, indium (I) oxide rapidly produces either solid or liquid indium (III) oxide by reacting with carbon dioxide.

For tin oxide sub-system, the Gibbs data are plotted in Figures B.5a-b. Similar to the indium oxide sub-system, many of these reactions have large negative ΔG_{rxn} (T). Any tin (IV) oxide molecule in the gas phase will either decompose into tin vapor and molecular oxygen or react with carbon monoxide to form tin (II) oxide vapor and carbon dioxide. Subsequently, the tin vapor can react with carbon dioxide or molecular oxygen to liquid or solid tin (II) oxide and tin (IV) oxide, with carbon monoxide as the by-product. It is observed that tin vapor may also be oxidized by carbon monoxide to from tin (II) oxide and graphite.

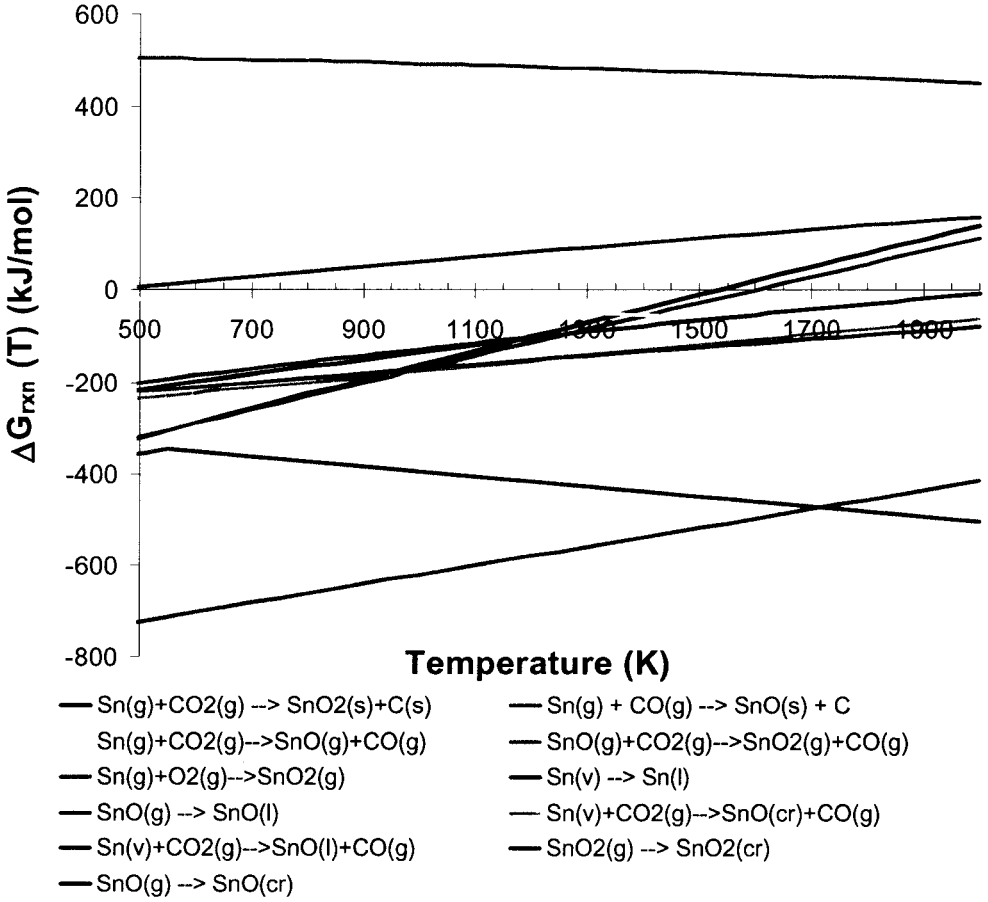

Figure B.5.a. Change in Gibbs free energy of reaction as function of temperature for consumption of tin-containing vapors in the gas phase, downstream of the source.

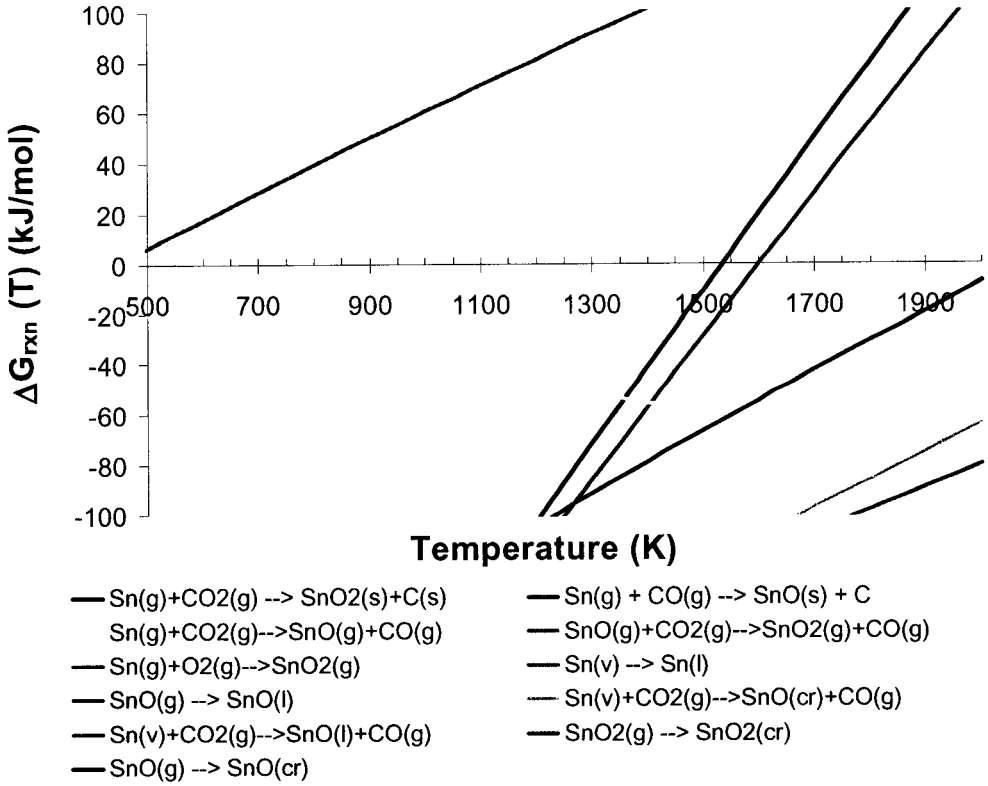

Figure B.5.b. Change in Gibbs free energy of reaction as function of temperature for consumption of tin-containing vapors in the gas phase, downstream of the source.

The large negative change in Gibbs free energy of reaction within the temperature process window suggests that some gas phase reactions may occur. The metal oxide aerosol nanoparticles may gravitate onto the wall of the quartz chamber, the boat, or onto the surface of the substrate itself. Once the nanoparticles are secured, they can serve as a thermodynamically favorable condensation points for other aerosol nanoparticles or semi-gas-phase reactions. It is noted that growth mode by this mechanism lacks directionality as compared to the catalytic-assisted VLS method. Thus, polycrystalline film is the likely product of this mechanism. Tables B.5.a-b list the equilibrium constants and reaction quotients at 1150 K for various gas-phase reactions.

Table B.5.a. Equilibrium constant and reaction quotient of the gas-phase indium-consumption reactions at 1150 Kelvin.

Potential Gas-Phase Reactions	K (1150 K)	Q (1150 K)	Q/K
$2In(g) + 3/2\ CO_2\ (g) \rightarrow In_2O_3(cr) + 3/2\ C(s)$	1.8720E+08	1.1682E+21	6.2400E+12
$In(g) + CO_2(g) \rightarrow InO(g) + CO(g)$	3.5553E-17	4.1578E-10	1.1695E+07
$2In(g) + CO_2(g) \rightarrow In_2O(g)+CO(g)$	5.6306E+09	3.4463E+02	6.1206E-08
$In(v) \rightarrow In(l)$	3.2721E+12	3.3247E-04	1.0161E-16
$InO(g) + In(v) \rightarrow In_2O(g)$	4.3096E+17	3.1346E+04	7.2737E-14
$In_2O(g) + 2\ CO_2(g) \rightarrow In_2O_3(cr) + 2CO(g)$	2.9689E+11	8.5445E+07	2.8780E-04
$In_2O(g) + 2\ CO_2(g) \rightarrow In_2O_3(l) + 2CO(g)$	8.4216E+08	2.3080E+07	2.7406E-02
$In_2O(g) + CO_2(g) \rightarrow In_2O_3(cr) + C(s)$	1.3713E+02	5.9241E+14	4.3202E+12
$2InO(g) + CO(g) \rightarrow In_2O_3(s) + 3/2\ C(s)$	1.5864E+21	1.6891E+21	1.0647E+00
$InO(g) \rightarrow In(v) + 1/2\ O_2$	1.6155E-04	3.7663E-02	2.3313E+02
$In_2O(g) + CO_2(g) \rightarrow 2InO + CO(g)$	3.0317E-26	3.5074E-07	1.1569E+19

Table B.5.b. Equilibrium constant and reaction quotient of the gas-phase tin-consumption reactions at 1150 Kelvin.

Potential Gas-Phase Reactions	K (1150 K)	Q (1150 K)	Q/K
$Sn(g) + CO_2(g) \rightarrow SnO_2(s) + C(s)$	2.2242E+05	1.7148E+12	7.7097E+06
$Sn(g) + CO(g) \rightarrow SnO(s) + C(s)$	7.3588E+05	2.5831E+11	3.5102E+05
$Sn(g) + CO_2(g) \rightarrow SnO\ (g) + CO(g)$	3.0184E+00	2.1969E-02	7.2784E-03
$SnO(g) + CO_2(g) \rightarrow SnO_2(g) + CO(g)$	5.7900E-24	8.8847E-02	1.5345E+22
$Sn(g) + O_2(g) \rightarrow SnO_2(g)$	3.9227E+00	1.1384E+04	2.9020E+03
$Sn(v) \rightarrow Sn(l)$	1.9014E+15	3.8404E-04	2.0198E-19
$SnO(g) \rightarrow SnO(l)$	3.8335E+10	3.5654E+05	9.3009E-06
$Sn(v) + CO_2(g) \rightarrow SnO(cr) + CO(g)$	1.8646E+07	3.7256E+04	1.9980E-03
$Sn(v) + CO_2(g) \rightarrow SnO(l) + CO(g)$	1.4772E+07	7.8329E+03	5.3025E-04
$SnO_2(g) \rightarrow SnO_2(cr)$	6.2944E+26	1.2671E+08	2.0131E-19
$SnO(g) \rightarrow SnO(cr)$	1.3572E+05	1.6959E+06	1.2496E+01

B.2.2.4 Catalytic head

As the vapor content progresses over the surface of the substrate, condensation of all metal vapor species, as well as metal oxide vapors, proceeds at the most thermodynamically favorable locations, i.e. the catalytic heads and nucleation sites from surface imperfections. In the case of the tin oxide sub-system, dissolved tin or tin (II) oxide can be oxidized by carbon dioxide and any oxygen in the gas-phase to form liquid tin (IV) oxide. At critical concentration, dissolved tin (IV) oxide crystallizes out of the

liquid alloy head at the interface between the head and the surface of the substrate or the body of the nanowire, depending on the growth stage. Similarly, indium vapor also dissolves into the liquid alloy head. Here, indium (I) and (II) oxides only exist in the vapor phase. At the liquid-gas interface, the indium atoms are oxidized by either carbon dioxide or molecular oxygen to form liquid and, subsequently, crystalline indium (III) oxide.

A comparison of the indium and tin plots shows that crystallization of liquid indium (III) oxide releases much more heat than the crystallization of tin (IV) oxide - ΔG_{cryst} (1150K) is -43.6 kJ/mol compared to -8.5 kJ/mol. However, there are more pathways for generation of tin (IV) oxide than indium (III) oxide. Again, the multiple reaction pathways available for the tin-oxide sub-system allow greater flexibility and higher conversion rate.

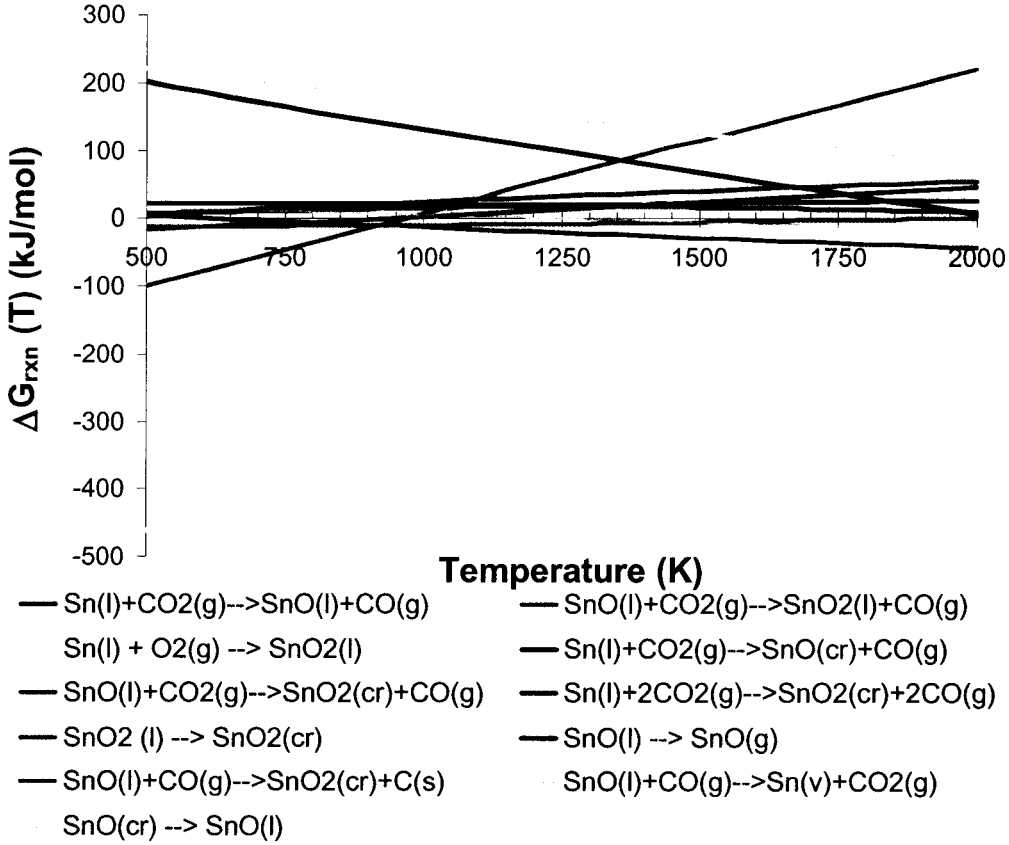

Figure B.6.a. Change in Gibbs free energy of reaction as function of temperature for consumption of tin-containing vapors at the catalytic liquid alloy nanoparticle.

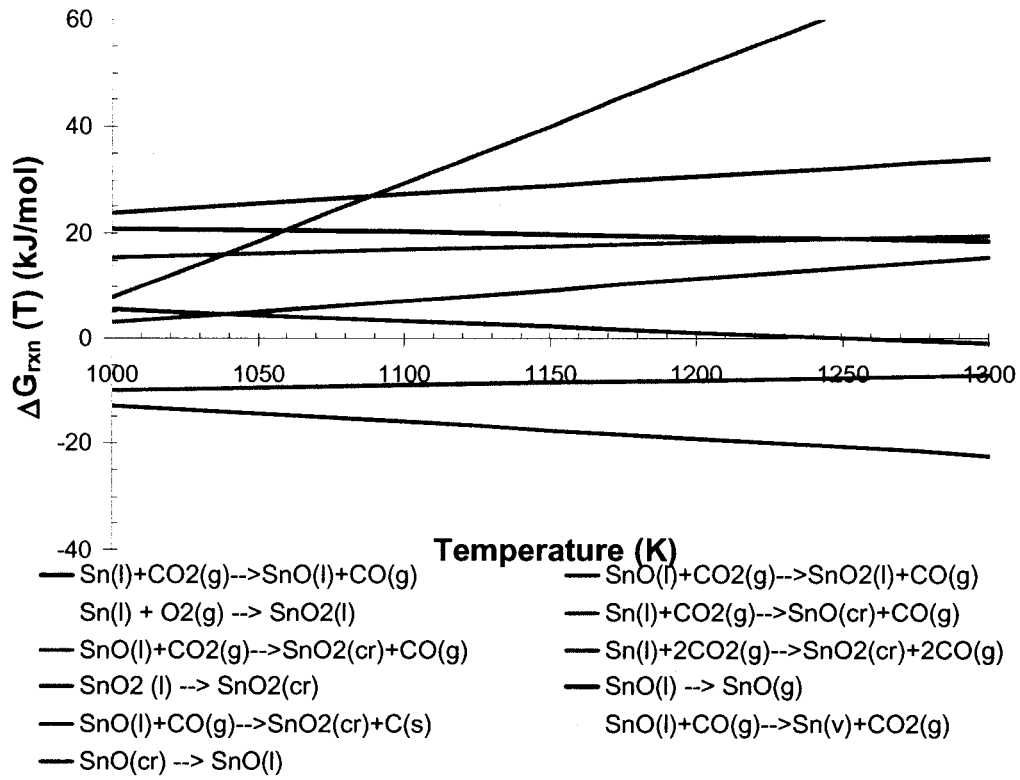

Figure B.6.b. Change in Gibbs free energy of reaction as function of temperature for consumption of tin-containing vapors at the catalytic liquid alloy nanoparticle.

Upon close examination of Figure B.6.b, the crystallization of tin (II) oxide becomes spontaneous at 1250 K. Although, as mentioned previously, the melting temperature of bulk tin (II) oxide is 1250 K, crystalline tin (II) oxide inside the liquid alloy droplet is expected to have a lower melting point due to the reduced dimensions and the solvation power of gold. Couple with the large negative ΔG_{rxn} (T) of the oxidation of liquid tin (II) oxide to liquid tin (IV) oxide by carbon dioxide, the composition of the nanowire is expected to be mainly tin (IV) oxide.

Another interesting reaction is the complete reduction of carbon monoxide to graphite by liquid tin (II) oxide. This reaction is highly thermodynamically unfavorable. Although carbothermal reduction is the mechanism of generating the tin-containing vapor at the source, the reverse reaction at the growth front of the nanowire to regenerate graphite is almost impossible. Thus, the nanowire is not expected to be doped with graphite.

Figure B.7 plots the thermodynamic behavior of the indium-oxide system. Since crystallization of indium (III) oxide is much more favorable than tin (IV) oxide, as discussed earlier, it is expected that indium (III) oxide will be the predominant constituent of the nanowire if both exists in same concentration. The fact that tin (IV) oxide is the predominant component of the nanowire, although indium and tin should have similar dissolution properties, based on the binary phase diagrams with gold, further suggests that the vapor content of the various indium species is much lower than the vapor content of the various tin species. This inference is further supported by the solvation readiness of tin (II) oxide, compared to indium (I) and (II) oxides, which only exist in the gas phase. Thus, tin-containing species exist in higher concentration both in the gas phase and in the liquid-alloy phase.

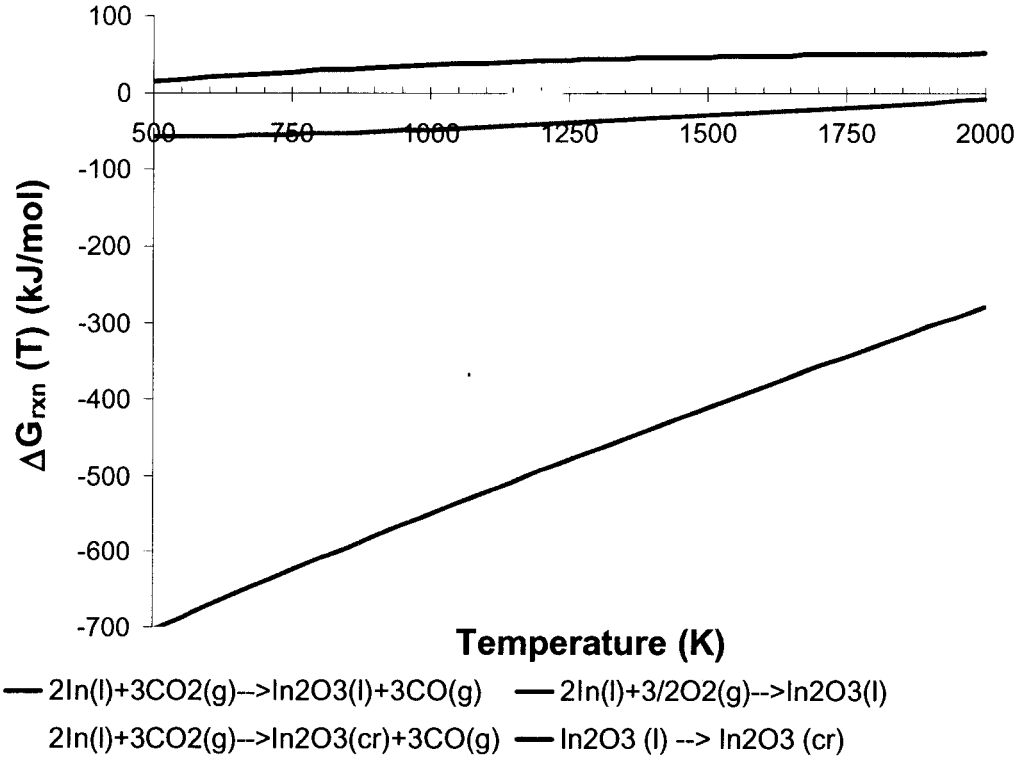

Figure B.7. Change in Gibbs free energy of reaction as function of temperature for consumption of indium-containing vapors at the catalytic liquid alloy nanoparticle.

Table B.6.a. Equilibrium constant and reaction quotient of the liquid-phase indium-consumption reactions at 1150 Kelvin.

Potential Reactions In The Catalyst Head	K(1150K)	Q(1150)	Q/K
2 In(l) + 3 CO_2(g) --> In_2O_3(l) + 3 CO(g)	9.4247E-01	6.2647E+01	6.6471E+01
2 In(l) + 3/2 O_2(g)--> In_2O_3(l)	1.0022E+35	8.8238E+11	8.8042E-24
2In(l) + 3 CO_2(g) --> In_2O_3(cr) + 3 CO(g)	3.3225E+02	2.3192E+02	6.9804E-01
In_2O_3(l) --> In_2O_3(cr)	9.5226E+01	3.7021E+00	3.8877E-02

Table B.6.b. Equilibrium constant and reaction quotient of the liquid-phase tin-consumption reactions at 1150 Kelvin.

Potential Reactions In The Catalyst Head	K(1150K)	Q(1150)	Q/K
$Sn(l) + CO_2(g) \rightarrow SnO(l) + CO(g)$	9.5625E-02	7.5634E-01	7.9094E+00
$SnO(l) + CO_2(g) \rightarrow SnO_2(l) + CO(g)$	2.3232E-01	3.6576E-02	1.5744E-01
$Sn(l) + O_2(g) \rightarrow SnO_2(l)$	9.2390E+22	1.2060E+08	1.3054E-15
$Sn(l) + CO_2(g) \rightarrow SnO(cr) + CO(g)$	5.7411E-01	3.5974E+00	6.2660E+00
$SnO(l) + CO_2(g) \rightarrow SnO_2(cr) + CO(g)$	1.2046E+01	3.1575E+01	2.6211E+00
$Sn(l) + 2\ CO_2(g) \rightarrow SnO_2(cr) + 2CO(g)$	1.1519E+00	2.3881E+01	2.0731E+01
$SnO_2(l) \rightarrow SnO_2(cr)$	2.4233E+00	1.1549E+00	4.7659E-01
$SnO(l) \rightarrow SnO(g)$	9.3009E-06	2.8047E-06	3.0155E-01
$SnO(l) + CO(g) \rightarrow SnO_2(cr) + C(s)$	1.5057E-02	2.1892E+08	1.4540E+10
$SnO(l) + CO(g) \rightarrow Sn(v) + CO_2(g)$	8.6425E-12	1.2767E-04	1.4772E+07
$SnO(cr) \rightarrow SnO(l)$	7.9222E-01	2.1025E-01	2.6539E-01

The enthalpy released by crystallization of the metal oxides may maintain a higher temperature at the catalytic head, preventing crystallization of tin (II) oxide and maintaining, perhaps, an internal convection loop to replenish the metal to the surface and transport the metal oxide to the surface. A detailed calculation requires an enormous computation power and is recommended for another study, as multiple processes, e.g. the heat of condensation, heat of reaction, reaction rate, convection in the gas phase and the liquid phase, etc, are involved.

A crude estimate is presented in Tables B.7.a-b, which tabulate the heat generation by the growing front of the nanowire and the rate of temperature increase if there is no other mean of heat dissipation/generation. Dimensions of a typical "tetragonal" nanowire are employed for calculation of the heat generation. For the catalytic head, two sets of calculation have been performed for pure gold and pure tin-oxide, as these sets the upper

and lower limits. Based on this calculation, the true temperature of the catalytic head can deviate as much as +170°C from the chamber temperature.

Table B.7.a. Heat released by crystallization of nanowire of assumed geometry.

Parameters	Value
Edge (m)	9.00E-08
Length (m)	5.00E-06
Volume (m^3)	4.05E-20
Time (s)	3600
Density (g/m^3)	6900000
MW (g/mol)	1.51E+02
Crystallization rate(mol/s)	5.15E-19
Heat released (J/s)	9.34E-15

Table B.6.7. Pseudo temperature "ramp-rate"

Parameters	Au Catalytic Head	SnO_2 Catalytic Head
Diameter (m)	1.10E-07	1.10E-07
Volume (m^3)	2.22E-22	2.22E-22
Mole	2.17E-18	1.02E-17
Cp (J/mol K)	25.42	82.303
Heat Rate (J/s)	169	11

B.2.3 Coulombic force as nucleation force

The bond which holds the crystal lattice of metal oxides exhibits ionic bonding characteristics. It is worthwhile to investigate the roles of ionic bonding during nucleation for the epitaxial growth. Here, the ionic bonding character of the metal oxide bonds is assumed to be 100%. It is noted that the true ionic character is less than that since the ionic character of zinc (II) oxide is 62% and that of sodium chloride is 94%.

Lattice potential energy is given by the Born-Mayer equation and the Kapustinskii equation, based on the Coulombic attraction force and the Born repulsion, i.e. the

repulsion due to overlapping of the electron clouds. Nomenclature is defined in the Nomenclature section. Typical lattice energy versus inter-atomic distance plot is shown in Figure B.8. "r_o" is the equilibrium position.

$$F_{Coulombic} = -\left(\frac{e^2 N_{AV}}{4\pi\varepsilon_o}\right)(Z_+ Z_-)\left(\frac{1}{d^2}\right) \qquad \text{Equation B.11}$$

$$F_{\text{Re}\,pulsive} = \lambda\ \exp\left(-a/\rho\right) \qquad \text{Equation B.12}$$

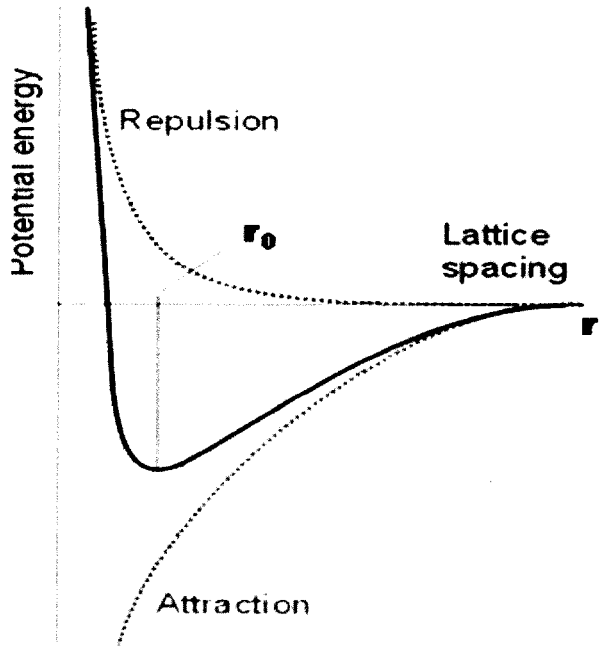

Figure B.8. Lattice energy as a function of lattice spacing

B.2.4 Kinetics of phase transformation

The transition of the solutes from the quasi-liquid state to the crystalline solid state also displays an Arrhenius behavior. Here, however, the activation energy barrier is minimal. The probability of an atom reaching the activated state is given by $\exp\frac{-\Delta G^A}{k\,T}$.

The rate of transformation is proportional to $\exp\frac{-\Delta G^{A}}{R\,T}$, which is the Arrhenius rate equation. In a multiple-component system, the activation energy barriers of the corresponding species may eventually dictate the composition of the crystalline state.

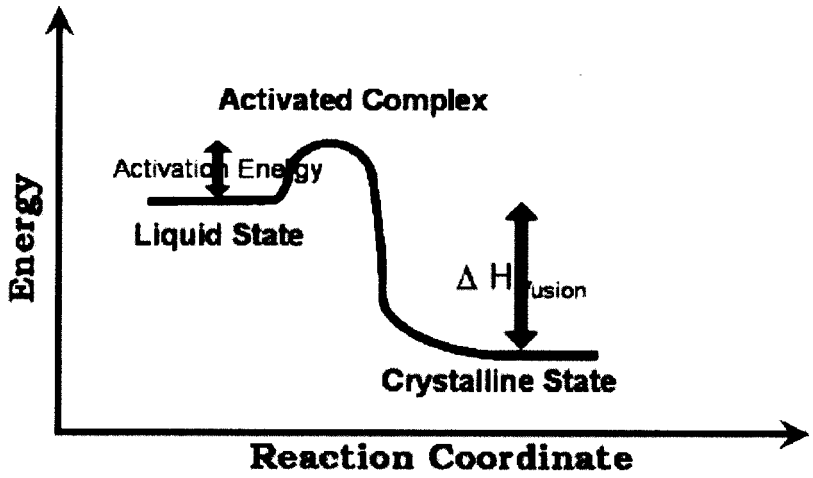

Figure B.9. Reaction coordinate diagram of phase transformation.

According to Figure B.9, at high temperature, the metal oxide molecules at the liquid-solid interface may accumulate sufficient kinetic energy to overcome the binding energy of the crystal lattice structure, i.e. the reverse enthalpy of phase transformation, and change to liquid phase. This behavior is similar to ice melting inside a liquid at temperature above 273.15 Kelvin. Thus, the existence of the upper limit of the feasible synthesis temperature window can be partially rationalized by such Arrhenius plot.

B.2.5 Solubilities of Metallic Gold, Tin and Indium in Crystal Lattice of Nanowire

In available literature, it is usually claimed that the nanowires synthesized by the VLS mechanism are composed purely of the nanowire materials, e.g. metal oxide, GaAs, or InP, despite the fact that another metal, gold in this case, serves as the catalyst material. Here, an elementary investigation into the thermodynamics of mixing is conducted to determine if the metal catalyst can exist within the nanowire crystal lattice.

Similar to Equation B.2, the change in Gibbs free energy of mixing is given below,

$$\Delta G_{mix} = \Delta H_{mix} - T\,\Delta S_{mix}$$

For an ideal solution, the enthalpy of mixing, ΔH_{mix}, is zero and the entropy of mixing is, $\Delta S_{mix} = -R \sum_{i=1}^{i=N} (X_i \ln X_i) = -R\,(X_A \ln X_A + X_B \ln X_B)$ for a binary solution.

For a regular binary solution, $\Delta H_{mix} = N_{AB}\varepsilon = N_{AB}\left(\varepsilon_{AB} - \frac{1}{2}(\varepsilon_{AA} - \varepsilon_{BB})\right)$ where N_{AB} = # of bond and ε_{ij} is the binary bond energy.

If ε is approximately zero, $\Delta H_{mix} = N_{AB} N_{AV} Z\ \varepsilon\ X_A X_B = \Omega\ X_A X_B$, where N_{AV} is the Avogadro's number and Z is the number of bond per atom.

For an infinitely dilute solution, $\lim_{X_{A\ or\ B} \to 0} -T\,\Delta S_{mix}$ asymptotically approaches an infinitely negative value, whereas, $\lim_{X_{A\ or\ B} \to 0} \Delta H_{mix}$ approaches a finite value of O.

Consequently, $\Delta G_{mix} = \Delta H_{mix} - T\,\Delta S_{mix}$ will always decrease on small incorporation of a solute into a solution, as shown in Figure B.10. Consequently, statistical incorporation of

the elemental metals into the crystal lattice of the nanowires, either substitutionally or interstitially, is inevitable as the synthesis proceeds. Interested readers ought to refer to a good solid-solution thermodynamics book for a detailed discussion.

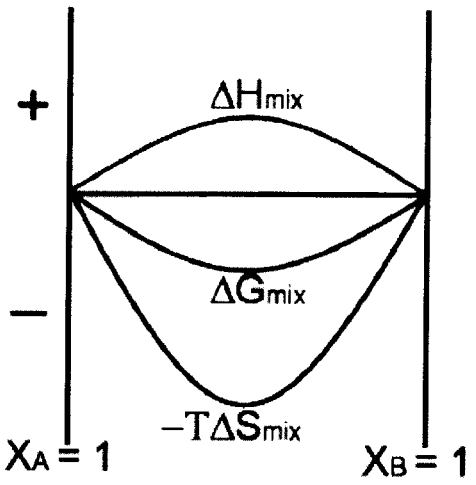

Figure B.10. Thermodynamics of mixing for a binary solution.

The equilibrium concentration of the solute in the solution is an Arrhenius function of temperature.

$$X_{B\ in\ A}^{equilibrium} = A\ \exp\left(\frac{-Q}{RT}\right)$$

where A is a function of entropy, $A = \exp\left(\frac{\Delta S_B}{R}\right)$,

and $Q = \Delta H_B + \Omega$ is the enthalpy change upon addition of one mole of solute B in solution A,.

APPENDIX C

GAS FLOW DYNAMICS CONSIDERATION

C.1 Mass Transport Limitation

To determine the flow regime of the reaction conditions, the Reynolds number, as defined below, was calculated to be 2.40. The density was calculated, assuming argon is the main constituent, using the ideal gas equation for the reaction temperature of 1123K. The viscosity was chosen to be 5.00E-5 kg/m s. Such low value of the dimensionless Reynolds number highly suggests laminar flow behavior.

$$\mathrm{Re} = \rho v D / \mu$$

Table C.1. Parameters for Re calculation

Parameters	Units	Value
T	K	1123.15
P	atm	1.0
Q	m^3/s	0.000005
D	m	0.023
v	m/s	0
μ	kg/m s	5.00E-05
ρ	kg/m^3	0.434001

To compare the relative flux ratio of the vapor going into the surface of the horizontal substrate and the 45° slanted substrate, as shown in Figure C.1, the following assumptions were made to simplify calculation.

1. Stagnant film diffusion

2. Deposition materials in trace amount
3. Instantaneous and complete reaction at the surface of the substrate
4. Reaction rate is independent of time and substrate topography.
5. Diffusivity and reactivity of all species are identical

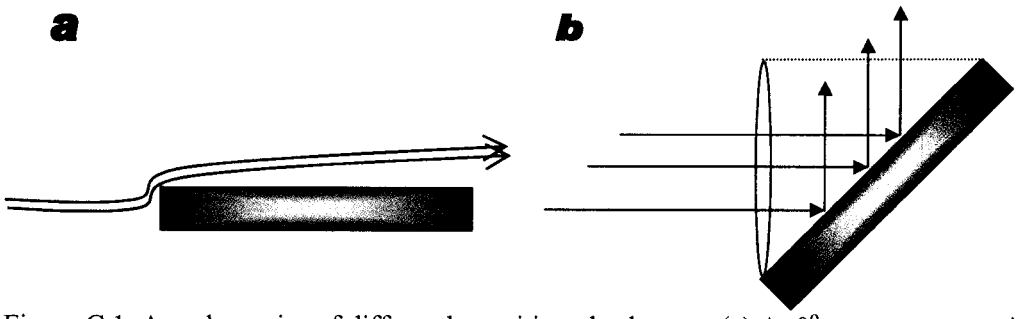

Figure C.1. Aerodynamics of differently positioned substrate. (a) At 0^{o}, mass transport is by means of stagnant layer diffusion. (b) At 45^{o}, convection dominates mass transport.

Since the flow is in laminar flow regime, it becomes apparent that diffusion through a stagnant film is the main means of transporting materials to the surface of the horizontal substrate; whereas, convection is the dominant transport mechanism for the slanted substrate. Figure C.1 quickly demonstrates how improvement to uniformity can be made in case of relatively fast reaction rate. Solution of the as-described mass-transport problem can be readily attained by any astute chemical engineering student; hence, an example is redundant here.

C.2 Diffusion of Oxygen into the Process Chamber

To approximate the diffusion of molecular oxygen from the environment into the process chamber, the following simplified analysis can be performed. The experimental set up is shown in Figure C.2 and the assumptions are given below.

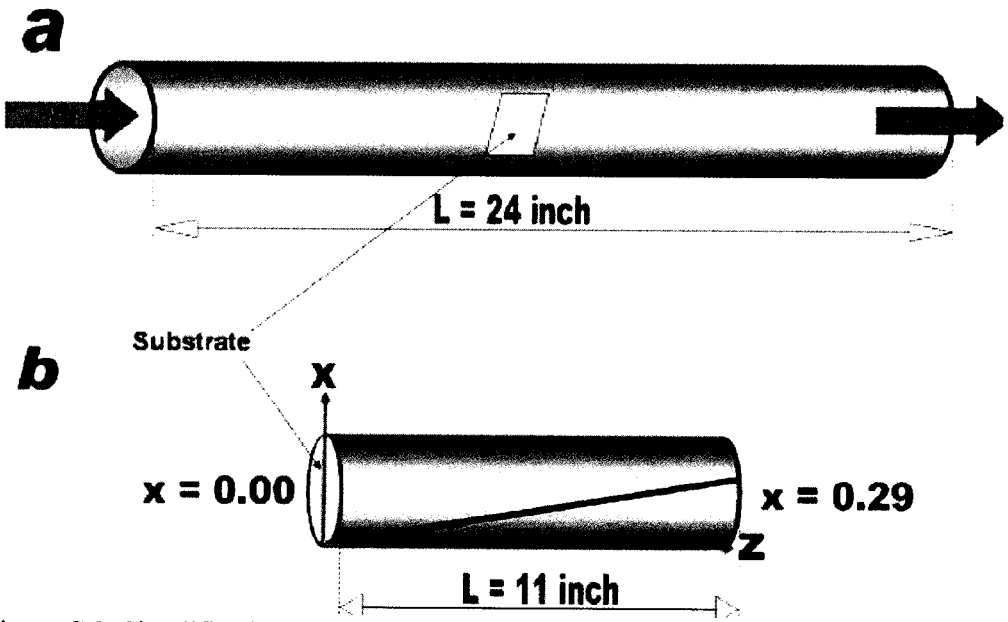

Figure C.2. Simplification of O_2 transport problem. (a) Experimental set-up. (b) Simplification of experimental set-up, where assumptions (2) – (4) are applied; the superimposed plot is the simplified concentration profile of O_2.

Assumptions:

(1) Quasi-steady state,

(2) The bulk of the oxidation reactions only occur at the surface of substrate or no homogeneous reaction,

(3) Reactions are instantaneous and oxygen consumption is complete at the substrate,

(4) Convection of oxygen is much less than diffusion of oxygen,

(5) 1-D simplification,

(6) Linear temperature profile from substrate to egress of chamber, and

(7) Mass transfer problem is uncoupled from momentum and energy transfer problems.

Thus, the mass conservation axiom for molecular oxygen, henceforth labeled "A", is reduced from

$$\frac{\partial c_A}{\partial t} + \nabla \cdot N_A = R_A$$

to

$$\frac{d^2 X}{d^2 z} = 0$$

where X is the partial pressure of oxygen, with the following boundary conditions:

B.C.1 $X = X_0$ or 0, $z = 0$

B.C.2 $X = X_8$ or 0.29, $z = L$ or 11 inches.

And the solution becomes

$$X = {}^{x_\infty}\!/_{L} * z .$$

Thus, the net flux is calculated as followed

$$Net\ Flux = Area * J_{Az} = Area * D_{A-Ar} \frac{dC_A}{dz}$$

or

$$Net\ Flux = Area * D_{A-Ar} \frac{P_{atm}}{R\,T_{rm}} * \frac{x_\infty}{L} .$$

The theoretical binary diffusivity value, $D_{A\text{-}Ar}$, can be determined via either the Chapman-Enskog equation or the temperature-dependence correlation equation provided by Carl Yaws. Both of these equations are listed below

$$D = \frac{1.8583 * 10^{-3} * T^{3/2} \sqrt{\frac{1}{M_1} + \frac{1}{M_2}}}{p\sigma_{12}^2 \Omega_{12}}$$

$$D_A = A + BT + CT^2$$

where T, M_i, p, σ_{12}, and Ω_{12} are the temperature, molecular mass of species i, total pressure, collision diameter, and collision integral, respectively; A, B, and C are experimentally determined parameters specific for each gaseous species.

Using a nominal value of 0.1 cm^2/s for the binary diffusivity, the flux of oxygen into the reaction chamber is calculated to be 0.2 μmol/s. Although this value is an overestimate and a more detailed analysis can provide more insights, this calculation demonstrates that diffusion can be a significant source of oxygen inside the chamber.

APPENDIX D

MISCELLANEOUS

D.1 Coalescence of Gold Thinfilm at High Temperature

At high temperature, the solid gold thin film becomes a quasi-liquid film, disintegrates, and forms gold droplets due to the low wetting coefficient and low miscibility between gold and the polished sapphire surface, much similar to water droplet formation on the surface of a glass plate. The Young's equation gives the contact angle between the free surface of the substrate and the liquid droplet, as shown in Figure D.1. This phenomenon has been observed experimentally using atomic force microscopy [67] and scanning electron microscope, as shown in Figure D.2.

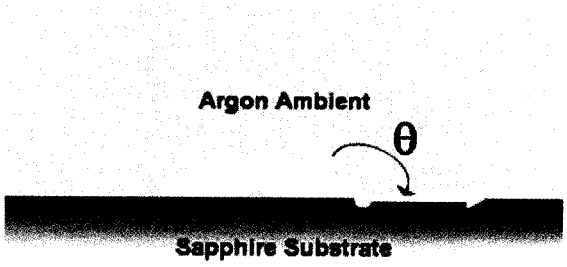

Figure D.1. Contact angle and surface tension.

$\gamma_{SL} + \gamma_{LG} \cos\theta - \gamma_{SG} = 0$ (Young's Equation)

or $\cos\theta = \frac{\gamma_{SG} - \gamma_{SL}}{\gamma_{LG}}$

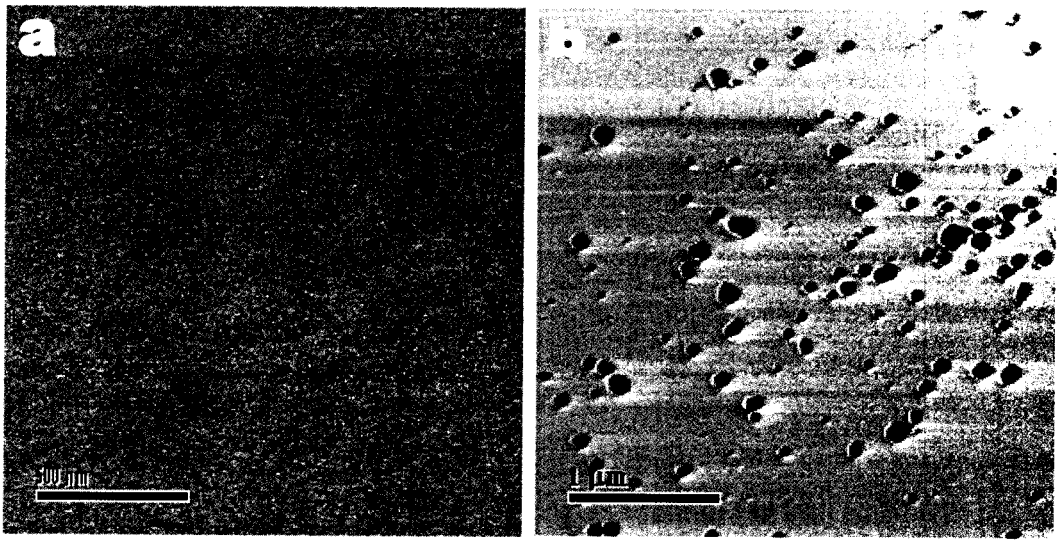

Figure D.2. Coalescence of gold thin film at elevated temperature. (a) top view of 2-nm gold film as-deposited by ion-beam sputtering on *a*-plane sapphire. (b) same sample annealed at 1000 °C for 30 minutes, in 30 sccm argon environment, image is taken at 30° angle to minimize the charging effect due to accumulation of electrons on the non-conducting sapphire surface.

D.2 Luminescence Effects

Figure D.3 demonstrates photoluminescence. Here, a photon source of energy higher than the bandgap energy of the material is directed at the surface. Upon absorption of the photonic energy, the electron become excited and promoted to the conduction band. A process called thermalization occurs if the electron possesses excessive energy, where it disperses its energy in form of heat as it "rolls" down to a lower energy level within the conduction band. Luminescence results as the electron recombines with the hole in the valence band as it transitions down, as shown in Figure D.3. The luminescence intensity is proportional to the product of the density of state, the occupancy factor of the electron, and the occupancy factor of the hole. Boltzman's statistics can be applied to calculate the occupancy factors. Photoluminescence study finds frequent applications in determination of the band gap energy level. A good textbook is highly recommended for the enthusiast.

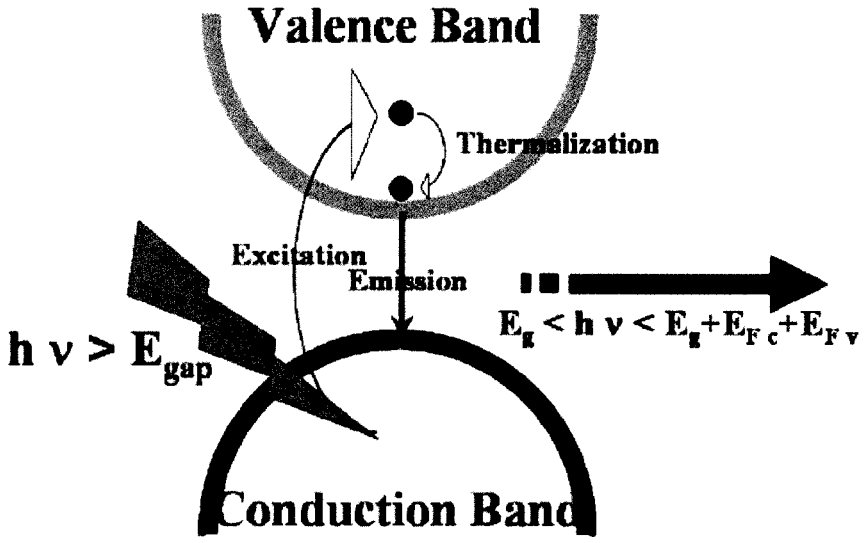

Figure D.3. Photoluminescence

In electroluminescence, electrons and holes are pumped into the diode junction. As they combine across the band gap, a photon of approximately the same energy as the bandgap energy is emitted, as shown in Figure D.4. For commercial applications, electroluminescence is highly desirable over photoluminescence. Again, a text book will provide a more comprehensive mechanistic view.

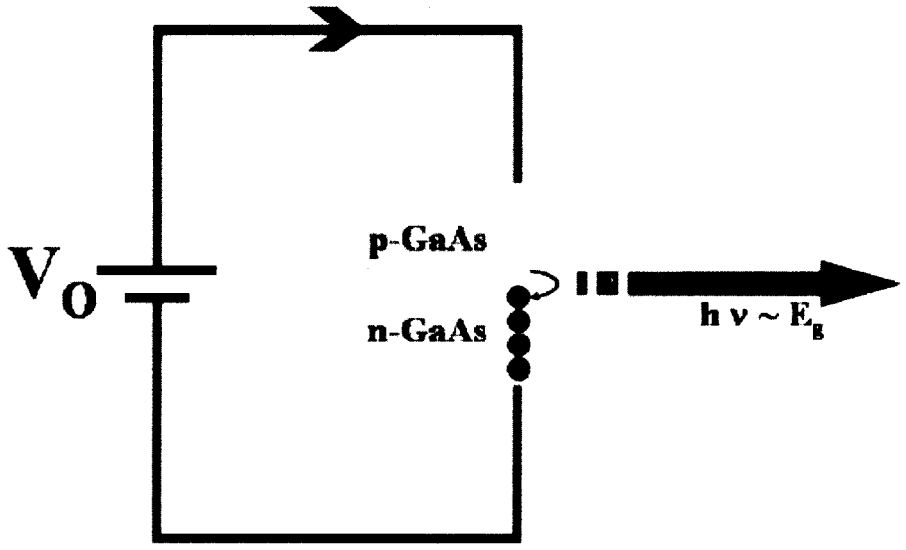

Figure D.4. Electroluminescence (a GaAs laser diode)